Acta Numerica (2021), pp. 765–851 Printed in the United Kingdom
doi:10.1017/S0962492921000088

Modelling and computation of liquid crystals

Wei Wang
Department of Mathematics, Zhejiang University, Hangzhou 310027, China
E-mail: wangw07@zju.edu.cn

Lei Zhang
Beijing International Center for Mathematical Research,
Center for Quantitative Biology, Peking University, Beijing 100871, China
E-mail: zhangl@math.pku.edu.cn

Pingwen Zhang
School of Mathematical Sciences, Peking University, Beijing 100871, China
E-mail: pzhang@pku.edu.cn

Liquid crystals are a type of soft matter that is intermediate between crystalline solids and isotropic fluids. The study of liquid crystals has made tremendous progress over the past four decades, which is of great importance for fundamental scientific research and has widespread applications in industry. In this paper we review the mathematical models and their connections to liquid crystals, and survey the developments of numerical methods for finding rich configurations of liquid crystals.

CONTENTS

1 Introduction 766
2 Mathematical models of liquid crystals 770
3 Mathematical analysis for different liquid crystal models 789
4 Numerical methods for computing stable defects of liquid crystals 801
5 Numerical methods for computing liquid crystal hydrodynamics 815
6 Numerical methods for computing transition pathways and the solution landscape of liquid crystals 822
7 Conclusion and future directions 833
Appendix 838
References 840

1. Introduction

Liquid crystals (LCs) are a classical example of partially ordered materials that translate freely as liquids and exhibit some long-range order above a critical concentration or below a critical temperature. The anisotropic properties lead to anisotropic mechanical, optical and rheological properties (de Gennes and Prost 1993, Stewart 2004), and make LCs suitable for a wide range of commercial applications, among which the best-known is the LC display industry (Stephen and Adrian 2002, Majumdar, Newton, Robbins and Zyskin 2007). LCs also have substantial applications in nanoscience, biophysics and materials design, for example. Furthermore, an LC is a typical system of complex fluids, so the theoretical approaches or technical tools of LC systems can be applied beyond the specific field of LCs, such as surface/interfacial phenomena, active matter, polymers, elastomers and colloid science (Takashi and Yasumasa 2010, Muller *et al.* 2012, Cai, Zhang and Shi 2017*b*).

LCs are mesophases between anisotropic crystalline (Figure 1.1(a)) and isotropic liquid (Figure 1.1(e)). There are three major classes of LCs: nematic, cholesteric and smectic (Friedel 1922). The simplest phase is the nematic phase (Figure 1.1(d)), where there is long-range orientational order, *i.e.* the molecules almost align parallel to each other, but no long-range correlation to the molecular centre of mass positions. On a local scale the cholesteric (Figure 1.1(c)) and nematic orders are similar, while on a larger scale the director of cholesteric molecules follows a helix with a spatial period. A nematic liquid crystal is a special cholesteric liquid crystal with no helix. Smectics (Figure 1.1(b)) have one degree of translational ordering, resulting in a layered structure. As a consequence of this partial translational ordering, the smectic phases are much more viscous and closer to crystalline than either the nematic or cholesteric phases.

The most widely studied system of LCs is a rod-like nematic liquid crystal (NLC), whose molecules are rod-shaped and rigid. In such an NLC, the molecules may move freely like a liquid, but the molecules in a local area may tend to align along a certain direction, causing the liquid to be anisotropic. In order to describe

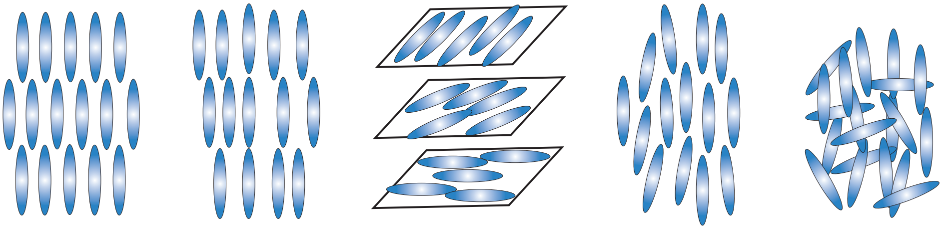

(a) crystalline (b) smectic (c) cholesteric (d) nematic (e) isotropic

Figure 1.1. Schematic representation of (a) crystalline, (b) smectic, (c) cholesteric, (d) nematic and (e) isotropic phases with rod-like molecules.

the anisotropic behaviour of NLCs, one has to choose appropriate functions, called *order parameters* in the physics community. There are various ways to choose order parameters, leading to mathematical theories at different levels, ranging from microscopic molecular theories to macroscopic continuum theories.

The first type of model is the vector model, including the Oseen–Frank theory (Oseen 1933, Frank 1958) and Ericksen's theory (Ericksen 1990). In these models it is assumed that there exists a locally preferred direction $\mathbf{n}(\mathbf{x}) \in \mathbb{S}^2$ (the unit sphere in three-dimensional space) for the alignment of LC molecules at each material point $\mathbf{x}$. This setting is rough but works very well in many situations, so the vector theory has been widely used in the LC community for its simplicity. However, vector theories have the drawback that they do not respect the head-to-tail symmetry of rod-like molecules, in which $-\mathbf{n}$ should be equivalent to $\mathbf{n}$ (Ball and Zarnescu 2008). This drawback may lead to an incorrect description of some systems, especially when defects are present.

The second is the molecular model, which was proposed by Onsager (1949) to characterize the nematic–isotropic phase transition, and then developed by Doi (1981) to study LC flow. In this theory, the alignment behaviour is described by an orientational distribution function $f(\mathbf{x}, \mathbf{m})$ which represents the number density of molecules with orientation $\mathbf{m} \in \mathbb{S}^2$ at a material point $\mathbf{x}$. Since the distribution function f contains much more information on molecular alignment, molecular models can provide a more accurate description. However, the computational cost is usually very high, as it often involves solving high-dimensional problems.

The third type of model is the $\mathbf{Q}$-tensor model, including the Landau–de Gennes (LdG) theory (de Gennes and Prost 1993), which uses a traceless symmetric 3×3 matrix $\mathbf{Q}(\mathbf{x})$ to describe the alignment of LC molecules at the position $\mathbf{x}$. From a physical viewpoint, the order parameter $\mathbf{Q}$-tensor is related to the second moment of the orientational distribution function $f(\mathbf{x}, \mathbf{m})$. It does not assume that the molecular alignment has a preferred direction and it can thus describe biaxiality.

The vector theory and tensor theory are called macroscopic theories, and are based on continuum mechanics, while the molecular theory is a microscopic one that is derived from the viewpoint of statistical mechanics. Although they were proposed from different physical viewpoints, all of them play important roles and have been widely used in studies of LCs. Understanding these models and their relationships has become an important issue for LC studies. Moreover, the coefficients in macroscopic theories are phenomenologically determined, and their interpretations in terms of basic physical measurements remain unclear. By exploring their relationships, one can determine these coefficients in terms of the molecular parameters, which provide a clear physical interpretation rather than a phenomenological determination. From the perspective of mathematical modelling, much effort has been devoted to their relationship, especially microscopic foundations of macroscopic theories. However, little work was done from the analytical side until some progress in the past decade. New experimental works and theoretical paradigms call for major modelling and analysis efforts.

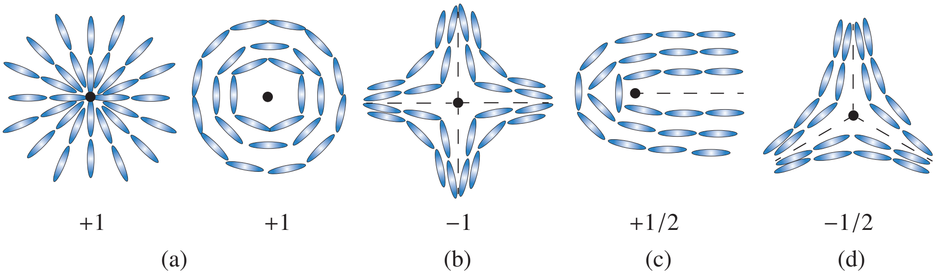

Figure 1.2. (a–d) Schematic diagrams of ±1 and ±1/2 2D point defects.

A particularly intriguing feature of LCs is that of topologically induced defects (Kléman 1989, Ball 2017). Defects are discontinuities in the alignment of LCs. They are classified as point defects, disclination lines and surface defects, and are further classified by the topological degree of defects, including two-dimensional (2D) ±1 and ±1/2 point defects (Figure 1.2). Defects are energetically unfavourable because the existence of defects will increase the elastic energy of nearby LCs. However, defects are unavoidable due to the environment, such as external fields (electric fields and magnetic fields: Oh-e and Kondo 1995), geometric constraints (boundary conditions and the domain: de Luca and Rey 2007) and non-smooth boundaries (polygon corners: Han, Majumdar and Zhang 2020*a*). NLCs are a typical system for studying defects, rich static structures and dynamic processes relevant to defects. Defects have the property of being isotropic and are surrounded by NLC molecules, and hence are able to induce phase transitions between NLC phases and isotropic phases (Mottram and Sluckin 2000, Mottram and Hogan 1997). The multiplicity of defect patterns also guides the design of new multi-stable LC display devices (Willman, Fernández, James and Day 2008).

A topologically confined NLC system can admit multiple stable equilibria, which usually correspond to different defect patterns (Kralj, Virga and Žumer 1999, Wang, Zhang and Chen 2017, Robinson *et al.* 2017). The energy landscape of an NLC system, in which the equilibrium states are located, is determined by the properties of the LC material as well as the environment, such as temperature, size and shape of the confining space, and the external field. Tremendous experimental and theoretical studies have been undertaken to investigate defect patterns in NLCs (Muševič *et al.* 2006, Lubensky, Pettey, Currier and Stark 1998, Onsager 1949, Bajc, Hecht and Žumer 2016).

From a numerical perspective, there are two approaches to computing stable defect patterns. One is the energy-minimization-based approach (Cohen *et al.* 1987, Alouges 1997, Adler, Atherton, Emerson and MacLachlan 2015, Nochetto, Walker and Zhang 2017, Majumdar and Wang 2018, Gartland Jr, Palffy-Muhoray and Varga 1991), which is often numerically solved by Newton-type or quasi-Newton methods. The other approach is to follow the gradient flow dynamics driven by the free energy corresponding to specific models of LCs (Fukuda, Stark, Yoneya and Yokoyama 2004, Ravnik and Žumer 2009, Canevari, Majumdar and Spicer 2017, Wang, Canevari and Majumdar 2019, MacDonald, Mackenzie and Ramage 2020). Various efficient numerical methods have been developed to solve the gradient flow equations, including energy-stable numerical schemes such as convex splitting methods (Elliott and Stuart 1993), invariant energy quadratization methods (Yang 2016) and scalar auxiliary variable methods (Shen, Xu and Yang 2018). Furthermore, machine learning has recently become an emerging approach in the field of soft matter including LCs (Walters, Wei and Chen 2019).

There are also extensive numerical developments for LC hydrodynamics to simulate LC flows, LC droplets and colloidal LC composites, for example (Badia, Guillén-Gónzalez and Gutiérrez-Santacreu 2011*b*, Foffano, Lintuvuori, Tiribocchi and Marenduzzo 2014). Various numerical studies of NLC dynamics have been performed by applying the Ericksen–Leslie equations (Liu and Walkington 2000, Becker, Feng and Prohl 2008), the hydrodynamic **Q**-tensor models (Beris and Edwards 1994, Zhao and Wang 2016) and the molecular models based on the extended Doi kinetic theory (Doi and Edwards 1988, Ji, Yu and Zhang 2008).

With the existence of multiple stable or metastable states in LC systems, transition can occur from one stable equilibrium to another under thermal fluctuation or external perturbations, causing the position and the topology of defects to change drastically (Kusumaatmaja and Majumdar 2015, Gupta, Sivakumar, Caruso and Abbott 2009). Thus it is important, both experimentally and theoretically, to determine when and how such a phase transition occurs. In the zero-temperature limit, the phase transition connecting two stable defects follows the so-called minimal energy path (MEP), which has the lowest energy barrier among all possible paths. The transition state corresponds to the state with the highest energy along the MEP, *i.e.* the index-1 saddle point (Zhang, Du and Zheng 2016*a*). Finding accurate critical nuclei and transition pathways is a challenging problem due to the anisotropic nature of the problems and the existence of a number of length scales. There are two typical approaches to computing transition states and transition pathways. One is the class of surface-walking methods, such as gentlest ascent dynamics (E and Zhou 2011) and the dimer-type method (Henkelman and Jónsson 1999). The other is path-finding methods, such as the string method (E, Ren and Vanden-Eijnden 2002) and the nudged elastic band method (Jónsson, Mills and Jacobsen 1998).

Besides local minimizers and transition states, there has been substantial recent interest in high-index saddle points with multiple unstable directions on the LC energy landscape, which are stationary solutions of the Euler–Lagrange equation corresponding to the LC free energy, and the Morse index is the number of negative eigenvalues of the corresponding Hessian of the free energy (Milnor, Spivak and Wells 1969). In recent years, a number of numerical algorithms have been developed to find multiple solutions of nonlinear equations, including the minimax method (Li and Zhou 2001), the deflation technique (Farrell, Birkisson and Funke 2015), the eigenvector-following method (Doye and Wales 2002) and the homotopy method (Mehta 2011). Despite substantial progress in this direction, the relationships between different solutions are unclear. In a recent work (Yin, Zhang and Zhang 2019), high-index saddle dynamics was proposed to efficiently compute any-index saddle points. By applying the high-index optimization-based shrinking dimer method, a solution landscape, which is a pathway map of all connected solutions, can be constructed for NLCs confined on a square domain (Yin *et al.* 2020*a*).

The rest of the paper is organized as follows. The mathematical models of LCs, including molecular models, vector models and tensor models, will be introduced in Section 2. Mathematical analysis and connections between different LC models will be discussed in Section 3. For the numerical computation of LCs, we will review numerical methods for computing stable defects of LCs in Section 4 and LC hydrodynamics in Section 5. In Section 6 we will introduce numerical algorithms to compute transition pathways between different LCs and the solution landscapes of LC systems. Section 7 will conclude with an outlook for trends and future developments of LCs.

2. Mathematical models of liquid crystals

In this section we review the three typical theories of LCs: molecular models, vector models and tensor models.

2.1. Molecular models

2.1.1. The static Onsager theory

Onsager (1949) proposed a classical model which can predict the isotropic–nematic phase transition for rod-like LCs. The theory is based on an orientational distribution function $f(\mathbf{m})$ which represents the number density of molecules with orientation $\mathbf{m}$. The free energy can be written as

$$A[f] = \int_{\mathbb{S}^2} \left\{ f(\mathbf{m}) \ln f(\mathbf{m}) + \frac{1}{2} f(\mathbf{m}) U(\mathbf{m}) \right\} \mathrm{d}\mathbf{m}. \tag{2.1}$$

The first term comes from the Brownian motion of the rod-like molecules, and the second term is the interaction term where $U(\mathbf{m})$ is the mean-field interaction potential

$$U(\mathbf{m}) = (U[f])(\mathbf{m}) := \int_{\mathbb{S}^2} B(\mathbf{m}, \mathbf{m}') f(\mathbf{m}') \,\mathrm{d}\mathbf{m}', \tag{2.2}$$

where $B(\mathbf{m}, \mathbf{m}')$ is the interaction potential between two molecules with orientation $\mathbf{m}$ and $\mathbf{m}'$. Onsager introduced the potential $B(\mathbf{m}, \mathbf{m}')$ with the form

$$B(\mathbf{m}, \mathbf{m}') = \alpha\, |\mathbf{m} \times \mathbf{m}'|, \tag{2.3}$$

which is calculated based on the excluded volume potential. Maier and Saupe (1958) proposed a similar interaction potential, now known as the Maier–Saupe potential:

$$B(\mathbf{m},\mathbf{m}') = \alpha\,|\mathbf{m}\times\mathbf{m}'|^2. \tag{2.4}$$

The parameter α represents the density (for lyotropic LCs) or the inverse of absolute temperature (for thermotropic LCs).

The energy functionals (2.1)–(2.2) with (2.3) or (2.4) are called the Onsager energy or the Maier–Saupe energy respectively. Both of them characterize the competition between the entropy and interaction energy and can effectively describe the nematic–isotropic phase transition. If the temperature is high or the density is dilute, the entropy term dominates the energy and the minimizer is the constant distribution $f(\mathbf{m}) = 1/(4\pi)$, which describes the isotropic phase. In contrast, if the temperature is low or the density is large, the energy is dominated by the interaction term and will be minimized by an axially symmetric distribution $f(\mathbf{m}) = f_0(\mathbf{m}\cdot\mathbf{n})$. This case corresponds to the nematic phase in which molecules prefer a uniform alignment. A rigorous proof for the Maier–Saupe energy was given independently by Liu, Zhang and Zhang (2005) and Fatkullin and Slastikov (2005). Another proof was given by Zhou, Wang, Forest and Wang (2005). More precisely, in these papers the following theorem was proved.

Theorem 2.1. All the critical points of the Maier–Saupe energy ((2.1)–(2.2) with (2.4)) are given by

$$h_{\eta,\mathbf{n}}(\mathbf{m}) = \frac{\mathrm{e}^{\eta(\mathbf{m}\cdot\mathbf{n})^2}}{\int_{\mathbb{S}^2}\mathrm{e}^{\eta(\mathbf{m}'\cdot\mathbf{n})^2}\,\mathrm{d}\mathbf{m}'},$$

where $\mathbf{n}$ is an arbitrary unit vector, and η is equal to 0 or satisfies

$$\frac{\int_0^1 \mathrm{e}^{\eta z^2}\,\mathrm{d}z}{\int_0^1 z^2(1-z^2)\,\mathrm{e}^{\eta z^2}\,\mathrm{d}z} = \alpha. \tag{2.5}$$

Furthermore, there exists

$$\alpha^* = \min_{\eta\in\mathbb{R}}\frac{\int_0^1 \mathrm{e}^{\eta z^2}\,\mathrm{d}z}{\int_0^1 z^2(1-z^2)\,\mathrm{e}^{\eta z^2}\,\mathrm{d}z} \approx 6.731393$$

such that the following hold.

(1) For $\alpha < \alpha^*$, (2.5) has no solution. For $\alpha = \alpha^*$, it has a unique solution $\eta = \eta^*$.

(2) For $\alpha > \alpha^*$, (2.5) has exactly two solutions $\eta = \eta_1(\alpha), \eta_2(\alpha)$ satisfying

- $\eta_1(\alpha) > \eta^* > \eta_2(\alpha)$, $\lim_{\alpha\to\alpha^*}\eta_1(\alpha) = \lim_{\alpha\to\alpha^*}\eta_2(\alpha) = \eta^*$,
- $\eta_1(\alpha)$ is an increasing function of α, while $\eta_2(\alpha)$ is a decreasing function,
- $\eta_2(7.5) = 0$.

The above theorem gives a complete classification of all critical points of the Maier–Saupe energy functional. The three kinds of solutions for $\eta = \eta_1, \eta_2, 0$

are referred to as prolate, oblate and isotropic solutions. Their stabilities are summarized in the following proposition. The proof can be found in Zhang and Zhang (2007) and Wang, Zhang and Zhang (2015*b*).

Proposition 2.2. $h = 1/(4\pi)$ $(\eta = 0)$ is a stable critical point of $A[f]$ if and only if $\alpha < 7.5$. If $\alpha > \alpha^*$, for any $\mathbf{n} \in \mathbb{S}^2$, $h_{\eta_1,\mathbf{n}}$ is stable, while $h_{\eta_2,\mathbf{n}}$ is unstable. Therefore, for $\alpha > 7.5$, $h_{\eta_1,\mathbf{n}}$ are the only minimizers.

Theorem 2.1 and Proposition 2.2 inform us that:

- the oblate solution is always unstable,
- if $\alpha > 7.5$, the prolate solution is the only stable solution, which corresponds to the nematic phase,
- if $\alpha < \alpha^*$, the isotropic solution is the only solution,
- for $\alpha \in (\alpha^*, 7.5)$, the prolate and isotropic solutions are both stable, which indicates that the isotropic phase and nematic phase can coexist in this parameter region.

Classification of minimizers of the Onsager energy functional is much more difficult, since the interaction potential is irregular and all even-order moments of the orientation distribution function are involved in the interaction part of the energy. The axial symmetry of all solutions to the 2D problem is proved by Chen, Li and Wang (2010). We refer to Vollmer (2017) and Ball (2020) for recent progress on the 3D problem.

2.1.2. *Dynamic Doi theory and its inhomogeneous extension*

The molecular theory was developed by Doi (1981) to study homogeneous LC flow. Under a given velocity gradient $\nabla\mathbf{v}$, the evolution of the distribution function is given by the following equation:

$$\frac{\partial f(t,\mathbf{m})}{\partial t} = \frac{1}{De}\mathcal{R}\cdot(\mathcal{R}f + f\mathcal{R}U) - \mathcal{R}\cdot(\mathbf{m}\times\kappa\cdot\mathbf{m}f). \tag{2.6}$$

Here De is the Deborah number, which characterizes the average time tending to local equilibrium state, $\mathcal{R} = \mathbf{m}\times\nabla_{\mathbb{S}^2}$ is the rotational gradient operator on the unit sphere, and $\kappa = (\nabla\mathbf{v})^\top$ is the transpose of the velocity gradient. The molecular alignment field in turn induces an extra stress tensor to the bulk fluids, which is given by

$$\sigma^{De} = \frac{1}{2}\mathbf{D}:\langle\mathbf{mmmm}\rangle_f - \frac{1}{De}\langle\mathbf{mm}\times\mathcal{R}\mu\rangle_f, \tag{2.7}$$

where $\mathbf{D} = (\nabla\mathbf{v} + (\nabla\mathbf{v})^\top)/2$ is the strain rate tensor, $\langle(\cdot)\rangle_f = \int_{\mathbb{S}^2}(\cdot)f\,\mathrm{d}\mathbf{m}$ denotes the average under the distribution f, and μ is the chemical potential:

$$\mu = \frac{\delta A[f]}{\delta f} = \ln f + U(\mathbf{m}).$$

Equation (2.6) has been very successful in describing the properties of LC polymers in a solvent. This model takes into account the effects of hydrodynamic flow, Brownian motion and intermolecular forces on the molecular orientation distribution. However, it does not include effects such as distortional elasticity and is thus valid only in the limit of spatially homogeneous flows.

Marrucci and Greco (1991) extended Doi's theory to the inhomogeneous case by incorporating long-range interaction into the theory. By using a truncated Taylor series expansion to approximate the non-local potential, the elastic energy is then described by gradients of the second moments of the distribution function. This method was subsequently developed by many people (Feng, Sgalari and Leal 2000, Wang 2002) to study inhomogeneous LC flow. However, instead of using the distribution as the sole order parameter, these works used a combination of the tensorial order parameter and the distribution function, and spatial variations were described by the spatial gradients of the tensorial order parameter, departing from the original motivation of the kinetic formulation.

Wang, E, Liu and Zhang (2002) used a more direct way to treat the intermolecular interaction by using the distribution function. They introduced an interaction potential to include the non-local interaction effects and extended the free energy (2.1) as follows:

$$\begin{aligned} A_\varepsilon[f] &= \int_\Omega \int_{\mathbb{S}^2} f(\mathbf{x},\mathbf{m},t)(\ln f(\mathbf{x},\mathbf{m},t)-1) + \frac{1}{2} U_\varepsilon(\mathbf{x},\mathbf{m},t) f(\mathbf{x},\mathbf{m},t)\,\mathrm{d}\mathbf{m}\,\mathrm{d}\mathbf{x}, \\ U_\varepsilon(\mathbf{x},\mathbf{m},t) &= \mathcal{U}_\varepsilon f := \int_\Omega \int_{\mathbb{S}^2} \mathcal{B}_\varepsilon(\mathbf{x},\mathbf{m};\mathbf{x}',\mathbf{m}') f(\mathbf{x}',\mathbf{m}',t)\,\mathrm{d}\mathbf{m}'\,\mathrm{d}\mathbf{x}', \end{aligned} \tag{2.8}$$

where $\mathcal{B}_\varepsilon(\mathbf{x},\mathbf{m};\mathbf{x}',\mathbf{m}')$ is the interaction potential between two molecules in the configurations $(\mathbf{x},\mathbf{m})$ and $(\mathbf{x}',\mathbf{m}')$, which depends on the non-dimensional small parameter $\varepsilon = L^2/L_0^2$ (here L is the length of the rods and L_0 is the typical size of the flow region). There are two typical choices.

(1) Hard-core excluded volume potential:

$$\mathcal{B}_\varepsilon(\mathbf{x},\mathbf{m};\mathbf{x}',\mathbf{m}') = \begin{cases} 1 & \text{molecule } (\mathbf{x},\mathbf{m}) \text{ is joint with molecule } (\mathbf{x}',\mathbf{m}'), \\ 0 & \text{disjoint with each other.} \end{cases} \tag{2.9}$$

(2) Long-range Maier–Saupe interaction potential:

$$\mathcal{B}_\varepsilon(\mathbf{x},\mathbf{m};\mathbf{x}',\mathbf{m}') = \frac{1}{\varepsilon^{3/2}} g\left(\frac{\mathbf{x}-\mathbf{x}'}{\sqrt{\varepsilon}}\right) \alpha|\mathbf{m}\times\mathbf{m}'|^2, \tag{2.10}$$

where $g(\mathbf{x})$ is a smooth function on $\mathbb{R}^3$ with $\int_{\mathbb{R}^3} g(\mathbf{x})\,\mathrm{d}\mathbf{x} = 1$, and the small parameter $\sqrt{\varepsilon}$ represents the typical interaction distance.

Both potentials are able to capture the non-local interaction between molecules and can thus describe distortion effects of the molecular alignment. The hard-core potential indeed coincides with Onsager's choice adopted in Onsager (1949). Note that different geometric shapes of molecules will lead to different energy forms. For NLCs, the molecules are commonly assumed to be prolate ellipsoids or spherocylinders. The long-range Maier–Saupe interaction potential (2.10), proposed in Yu and Zhang (2007), can be viewed as a smooth approximation for the hard-core potential, which is easier to analyse and simulate.

Based on the non-local energy, Wang *et al.* (2002) presented an inhomogeneous model for the LC flow. Define the chemical potential as

$$\mu_\varepsilon = \ln f(\mathbf{x}, \mathbf{m}, t) + U_\varepsilon(\mathbf{x}, \mathbf{m}, t).$$

Then the inhomogeneous (non-dimensional) system reads as

$$\begin{aligned}\frac{\partial f}{\partial t} + \mathbf{v}\cdot\nabla f &= \frac{\varepsilon}{De}\nabla\cdot\{(\gamma_{\|}\mathbf{mm} + \gamma_{\perp}(\mathbf{I}-\mathbf{mm}))\cdot f\nabla\mu_\varepsilon\}\\ &\quad + \frac{1}{De}\mathcal{R}\cdot(f\mathcal{R}\mu_\varepsilon) - \mathcal{R}\cdot(\mathbf{m}\times\kappa\cdot\mathbf{m}f),\\ \frac{\partial\mathbf{v}}{\partial t} + \mathbf{v}\cdot\nabla\mathbf{v} &= -\nabla p + \frac{1}{Re}\{\nabla\cdot(\tau^s + \tau^e) + \mathbf{F}^e_\varepsilon\}.\end{aligned} \tag{2.11}$$

Here $\mathbf{v}$ is the fluid velocity, p is the pressure and $\gamma_{\|}, \gamma_{\perp}$ are, respectively, the translational diffusion coefficients parallel to and normal to the orientation of the liquid crystal polymer (LCP) molecule. Re is the Reynolds number. The viscous stress τ^s, the elastic stress τ^e and the body force $\mathbf{F}^e$ are given by

$$\begin{aligned}\tau^s &= 2\gamma\mathbf{D} + \frac{1-\gamma}{2}\mathbf{D}:\langle\mathbf{mmmm}\rangle_f,\\ \tau^e &= -\frac{1-\gamma}{De}\langle\mathbf{mm}\times\mathcal{R}\mu_\varepsilon\rangle_f, \quad \mathbf{F}^e = -\frac{1-\gamma}{De}\langle\nabla\mu_\varepsilon\rangle_f.\end{aligned}$$

System (2.11) has the following energy-dissipation relation:

$$\begin{aligned}&\frac{\mathrm{d}}{\mathrm{d}t}\left(\int_\Omega \frac{Re}{2(1-\gamma)}|\mathbf{v}|^2\,\mathrm{d}\mathbf{x} + \frac{1}{De}A_\varepsilon[f]\right)\\ &\quad = -\int_\Omega\left(\frac{\gamma}{1-\gamma}|\mathbf{D}|^2 + \frac{1}{2}\langle(\mathbf{mm}:\mathbf{D})^2\rangle_f + \frac{1}{De^2}\langle|\mathcal{R}\mu_\varepsilon|^2\rangle_f\right.\\ &\qquad\left. + \frac{\varepsilon}{De^2(1-\gamma)}\langle\nabla\mu_\varepsilon\cdot(\gamma_{\|}\mathbf{mm} + \gamma_{\perp}(\mathbf{I}-\mathbf{mm}))\cdot\nabla\mu_\varepsilon\rangle_f\right)\mathrm{d}\mathbf{x},\end{aligned} \tag{2.12}$$

We refer to Yu and Zhang (2007) for the numerical study and Zhang and Zhang (2008) for the well-posedness of the system (2.11).

2.2. *Vector theories*

2.2.1. *Static vector models: the Oseen–Frank theory*

The molecular theories provide a detailed description of LCs, but they are not convenient to use. The simplest model for studying the equilibrium configuration for NLCs is the Oseen–Frank model, proposed by Oseen (1933) and Frank (1958).

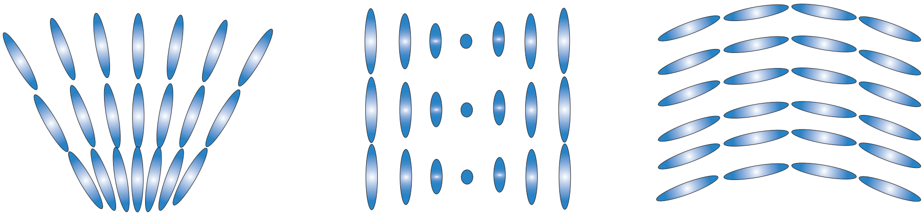

(a) splay (b) twist (c) bend

Figure 2.1. Three kinds of distortion: (a) splay, (b) twist and (c) bend.

It neglects the molecular details and uses a unit vector $\mathbf{n}(\mathbf{x})$ to describe the average orientation of LC molecules at position $\mathbf{x}$. Then the distortion energy, which is called the Oseen–Frank energy, takes the form

$$E_{OF}(\mathbf{n},\nabla\mathbf{n}) = \frac{k_1}{2}(\nabla\cdot\mathbf{n})^2 + \frac{k_2}{2}|\mathbf{n}\cdot(\nabla\times\mathbf{n})|^2 + \frac{k_3}{2}|\mathbf{n}\times(\nabla\times\mathbf{n})|^2 + \frac{(k_2+k_4)}{2}(\mathrm{tr}(\nabla\mathbf{n})^2 - (\nabla\cdot\mathbf{n})^2). \tag{2.13}$$

The constants k_1, k_2, k_3 represent moduli for three different kinds of pure deformation respectively, *splay*, *twist* and *bend*, which are illustrated in Figure 2.1. For prolate nematics, one often has

$$k_3 > k_1 > k_2 > 0.$$

The last term is actually a null Lagrangian which can be reduced to boundary terms. The simplest reduction for the Oseen–Frank energy is the case $k_1 = k_2 = k_3 = k$ and $k_4 = 0$, referred to as one-constant approximation, which leads to the Dirichlet energy

$$E(\nabla\mathbf{n}) = \frac{k}{2}|\nabla\mathbf{n}|^2.$$

For given boundary data on a bounded domain, the observed configuration usually corresponds to a minimizer of the Oseen–Frank energy. Applying the calculus of variations, a minimizer should satisfy, at least formally, the following Euler–Lagrange equations:

$$\mathbf{n}\times\mathrm{div}\left(\frac{\partial}{\partial\nabla\mathbf{n}}E_{OF}(\mathbf{n},\nabla\mathbf{n}) - \frac{\partial}{\partial\mathbf{n}}E_{OF}(\mathbf{n},\nabla\mathbf{n})\right) = 0,$$

or equivalently

$$\mathrm{div}\left(\frac{\partial}{\partial\nabla\mathbf{n}}E_{OF}(\mathbf{n},\nabla\mathbf{n}) - \frac{\partial}{\partial\mathbf{n}}E_{OF}(\mathbf{n},\nabla\mathbf{n})\right) = \lambda\mathbf{n}. \tag{2.14}$$

Note that $\mathbf{n}$ needs to satisfy the unit-norm condition $|\mathbf{n}| = 1$, which gives a nonlinear constraint and induces a Lagrange multiplier $\lambda \in \mathbb{R}$, in the above equation. In the one-constant approximation case, the equation reduces to the harmonic map equation

$$\Delta \mathbf{n} = -|\nabla \mathbf{n}|^2 \mathbf{n}.$$

Defects in vector theories are described by singularities in $\nabla \mathbf{n}$. For instance, the configuration $\mathbf{n}(\mathbf{x}) = \mathbf{x}/|\mathbf{x}|$ ($\mathbf{x} \in \mathbb{R}^3$) is a solution to (2.14), which is called the hedgehog solution. It is a typical and important example of point defects. In a 2D region, $\mathbf{n}(\mathbf{x}) = \mathbf{x}/|\mathbf{x}|$ is formally a solution to (2.14). However, the energy blows up near the singular point $\mathbf{x} = 0$. That is, the energy of a 2D point defect in vectorial description is infinite. Moreover, the following theorem has been proved by Hardt, Kinderlehrer and Lin (1986).

Theorem 2.3. If $\mathbf{n} \in H^1(\Omega, \mathbb{S}^2)$ is a minimizer of the Oseen–Frank energy E_{OF}, then $\mathbf{n}$ is analytic on $\Omega \setminus Z$, where Z is a relatively closed subset of Ω which has one-dimensional Hausdorff measure zero.

This fundamental result excludes the possibility of line defects, which have dimension one, under the framework of the Oseen–Frank theory. To resolve this problem, Ericksen (1990) proposed a vector model with an extra scalar order parameter $s \in (-1/2, 1)$, which represents the degree of orientation. Under the one-constant approximation, the Ericksen free energy takes the form

$$E(s, \mathbf{n}) = \int_\Omega \psi(s) + k|\nabla s|^2 + s^2|\nabla \mathbf{n}|^2 \, \mathrm{d}\mathbf{x}, \tag{2.15}$$

where $k > 0$ is a parameter and $\psi(s)$ is the potential function satisfying

- $\lim_{s\to 1} \psi(s) = \lim_{s\to -1/2} \psi(s) = +\infty$,
- there exists $s^* \in (0, 1)$ such $\psi(0) > \psi(s^*) = \min_{s\in(-1/2,1)} \psi(s)$,
- $\psi'(0) = 0$.

In Ericksen's theory, the defects are defined as zero sets of s, which permits the line defect or a 2D point defect (Lin 1991, Ambrosio 1990). We refer to Ericksen (1990) for details.

2.2.2. Dynamical vector models: the Ericksen–Leslie theory

The dynamic continuum theory for LC flows was established by Leslie (1968) and Ericksen (1961). The full system, which is called the Ericksen–Leslie system, takes the form

$$\begin{cases} \mathbf{v}_t + \mathbf{v} \cdot \nabla \mathbf{v} = -\nabla p + \nabla \cdot \sigma, \\ \nabla \cdot \mathbf{v} = 0, \\ \mathbf{n} \times (\mathbf{h} - \gamma_1 \mathbf{N} - \gamma_2 \mathbf{D} \cdot \mathbf{n}) = 0. \end{cases} \tag{2.16}$$

Here $\mathbf{v}$ is the fluid velocity, p is the pressure, and the stress σ is given by the phenomenological constitutive relation

$$\sigma = \sigma^L + \sigma^E,$$

where σ^L is the viscous (Leslie) stress,

$$\sigma^L = \alpha_1(\mathbf{nn}\colon \mathbf{D})\mathbf{nn} + \alpha_2\mathbf{nN} + \alpha_3\mathbf{Nn} + \alpha_4\mathbf{D} + \alpha_5\mathbf{nn}\cdot\mathbf{D} + \alpha_6\mathbf{D}\cdot\mathbf{nn}, \tag{2.17}$$

with

$$\mathbf{D} = \frac{1}{2}(\kappa^\top + \kappa), \kappa = (\nabla\mathbf{v})^\top \quad \text{and} \quad \mathbf{N} = \mathbf{n}_t + \mathbf{v}\cdot\nabla\mathbf{n} + \mathbf{\Omega}\cdot\mathbf{n}, \quad \mathbf{\Omega} = \frac{1}{2}(\kappa^\top - \kappa).$$

The constants $\alpha_1, \dots, \alpha_6$ in (2.17) are called the Leslie coefficients, while σ^E is the elastic (Ericksen) stress given by

$$\sigma^E = -\frac{\partial E_{OF}}{\partial(\nabla\mathbf{n})}\cdot(\nabla\mathbf{n})^\top, \tag{2.18}$$

and the molecular field $\mathbf{h}$ is given by

$$\mathbf{h} = -\frac{\delta E_{OF}}{\delta\mathbf{n}} = \nabla\cdot\frac{\partial E_{OF}}{\partial(\nabla\mathbf{n})} - \frac{\partial E_{OF}}{\partial\mathbf{n}}.$$

The Leslie coefficients and γ_1, γ_2 satisfy the following relations:

$$\alpha_2 + \alpha_3 = \alpha_6 - \alpha_5, \tag{2.19}$$

$$\gamma_1 = \alpha_3 - \alpha_2, \quad \gamma_2 = \alpha_6 - \alpha_5, \tag{2.20}$$

where (2.19) is called Parodi's relation, derived from the Onsager reciprocal relation (Parodi 1970). These two relations ensure a basic energy dissipation law of the system:

$$\begin{aligned}\frac{\mathrm{d}}{\mathrm{d}t}\left(\int_{\mathbb{R}^3}\frac{1}{2}|\mathbf{v}|^2\,\mathrm{d}\mathbf{x} + E_{OF}\right) = -\int_{\mathbb{R}^3}\Bigg(&\left(\alpha_1 + \frac{\gamma_2^2}{\gamma_1}\right)(\mathbf{D}\colon\mathbf{nn})^2 + \alpha_4|\mathbf{D}|^2 \\ &+ \left(\alpha_5 + \alpha_6 - \frac{\gamma_2^2}{\gamma_1}\right)|\mathbf{D}\cdot\mathbf{n}|^2 + \frac{1}{\gamma_1}|\mathbf{n}\times\mathbf{h}|^2\Bigg)\,\mathrm{d}\mathbf{x}.\end{aligned} \tag{2.21}$$

Besides the inability to describe line defects, vector models have some other drawbacks. For example, from the physical viewpoint, $\mathbf{n}(\mathbf{x})$ is not distinguishable from $-\mathbf{n}(\mathbf{x})$. This is referred to as the head-to-tail symmetry of LCs, which cannot be inherently revealed by the vectorial description. Indeed, there are some configurations that cannot be described by a vector field. For example, consider the point defect in 2D with degree 1/2 (see Figure 1.2(c)) and a circle near the defect point. The alignment on the circle is a smooth line field. However, one cannot define a continuous vector field $\mathbf{n} \in \mathbb{S}^1$ on this circle. This problem is carefully discussed in Ball and Zarnescu (2011) for more general domains.

In addition, in vector theories it is assumed that the orientation of the LC molecules has a preferred alignment at a material point. In most cases this assumption is reasonable. However, there are some situations in which a preferred alignment cannot be defined, for example near the core of a defect. So vector models fail to give accurate descriptions for molecular alignments near the core of defects.

2.3. *Tensor theories*

Despite its success in predicting the phase transition and rheological parameters for LCs, the molecular theory is not convenient in practice since it always leads to a high-dimensional problem with high costs. Therefore it is natural to explore alternative models to simulate LC flow or complex patterns. A common method to reduce the molecular theory is to consider the second-order moment of the probability distribution function $f(\mathbf{x},\mathbf{m})$:

$$\mathbf{Q}(\mathbf{x}) = \int_{\mathbb{S}^2}\left(\mathbf{mm}-\frac{1}{3}\mathbf{I}\right)f(\mathbf{x},\mathbf{m})\,\mathrm{d}\mathbf{m} \in \mathbb{Q} = \{\mathbf{Q}\in\mathbb{M}^{3\times3}, \mathbf{Q}=\mathbf{Q}^{\top}, \operatorname{tr}\mathbf{Q}=0\}, \tag{2.22}$$

which is called the $\mathbf{Q}$-tensor. Thus $\mathbf{Q}$ has five independent components. Let $\lambda_1,\lambda_2,\lambda_3$ be the three eigenvalues of $\mathbf{Q}$; then we can write

$$\mathbf{Q} = \lambda_1\mathbf{n}_1\mathbf{n}_1 + \lambda_2\mathbf{n}_2\mathbf{n}_2 + \lambda_3\mathbf{n}_3\mathbf{n}_3,$$

where $\mathbf{n}_1,\mathbf{n}_2,\mathbf{n}_3$ are unit norm vectors with $\mathbf{n}_i\cdot\mathbf{n}_j = 0$ $(1\le i<j\le 3)$. The definition (2.22) gives a constraint for the eigenvalues of $\mathbf{Q}$:

$$\mathbf{Q}\in\mathbb{Q}_{phy} = \left\{\mathbf{Q}\in\mathbb{Q}\colon \lambda_1,\lambda_2,\lambda_3\in\left(-\frac{1}{3},\frac{2}{3}\right)\right\}.$$

One can classify $\mathbf{Q}$ into three classes.

- If $\mathbf{Q}$ has three equal eigenvalues, *i.e.* $\mathbf{Q}=0$, we say $\mathbf{Q}$ is *isotropic*.
- If the eigenvalues have two distinct values, then there exist $s\in\mathbb{R}$, $\mathbf{n}\in\mathbb{S}^2$, such that
$$\mathbf{Q} = s\left(\mathbf{nn}-\frac{1}{3}\mathbf{I}\right).$$
In this case we say $\mathbf{Q}$ is *uniaxial*.
- If the three eigenvalues are distinct, we say $\mathbf{Q}$ is *biaxial*. In this case we can find $s,\lambda\in\mathbb{R}$, $\mathbf{n},\mathbf{m}\in\mathbb{S}^2$, such that $s\ne\lambda$, $\mathbf{m}\perp\mathbf{n}$ and
$$\mathbf{Q} = s\left(\mathbf{nn}-\frac{1}{3}\mathbf{I}\right) + \lambda\left(\mathbf{mm}-\frac{1}{3}\mathbf{I}\right).$$

If the LC material remains in the liquid state, *i.e.* the alignments are disordered, then the distribution function $f(\mathbf{x},\mathbf{m})$ is the uniform distribution on $\mathbb{S}^2$, which implies $\mathbf{Q}=0$, or equivalently $\mathbf{Q}$ is isotropic. If the material remains in the LC state, that is, $f(\mathbf{x},\mathbf{m})$ is an axially symmetric function on $\mathbb{S}^2$, *i.e.* $f(\mathbf{x},\mathbf{m}) = f(\mathbf{n}(\mathbf{x})\cdot\mathbf{m})$, then

$$\mathbf{Q} = s\left(\mathbf{nn}-\frac{1}{3}\mathbf{I}\right) \quad \text{with } s = \int_{\mathbb{S}^2}\frac{3(\mathbf{n}\cdot\mathbf{m})^2-1}{2}f(\mathbf{n}\cdot\mathbf{m})\,\mathrm{d}\mathbf{m},$$

which means that $\mathbf{Q}$ is uniaxial.

2.3.1. Static $\mathbf{Q}$-tensor models

For LC materials, the total energy $F^{LG}(\mathbf{Q},\nabla\mathbf{Q})$ consists of two parts: the *bulk energy* $F_b(\mathbf{Q})$, which dictates the preferred state of the material, and the *elastic energy* $F_e(\mathbf{Q},\nabla\mathbf{Q})$, which comes from the distortion of LCs, that is,

$$F^{LG}(\mathbf{Q},\nabla\mathbf{Q}) = F_b(\mathbf{Q}) + F_e(\mathbf{Q},\nabla\mathbf{Q}).$$

The energy should be frame-indifferent, that is, for any $\mathbf{P} \in O(3)$,

$$F(\tilde{Q},\tilde{\Psi}) = F(Q,\Psi),$$

where $\mathbf{\Psi} = \nabla\mathbf{Q}$ with $\Psi_{ijk} = Q_{ij,k}$ and $\tilde{\mathbf{Q}} = \mathbf{P}\mathbf{Q}\mathbf{P}^\top$, $\tilde{\mathbf{\Psi}}_{ijk} = P_{ii'}P_{jj'}P_{kk'}\Psi_{ijk}$.

The bulk energy is a function of the tensor $\mathbf{Q}$ which should predict the isotropic–nematic phase transition for LCs. Therefore, at high temperatures the bulk energy should arrive at its minimum at the isotropic state, while at low temperatures its minimizers should be uniaxial, which represents the nematic phase. In addition, due to the frame indifference, the bulk energy should depend only on the eigenvalues of $\mathbf{Q}$.

The simplest form that meets these requirements takes the following polynomial form:

$$F_b(\mathbf{Q}) = \frac{a}{2}|\mathbf{Q}|^2 - \frac{b}{3}\operatorname{tr}\mathbf{Q}^3 + \frac{c}{4}|\mathbf{Q}|^4, \tag{2.23}$$

where

$$|\mathbf{Q}|^2 = \sum_{i,j=1}^{3} Q_{ij}^2, \quad \operatorname{tr}\mathbf{Q}^3 = \sum_{i,j,k} Q_{ij}Q_{jk}Q_{ki}, \quad |\mathbf{Q}|^4 = (|\mathbf{Q}|^2)^2.$$

Here a, b, c are constants depending on materials and temperature in general with $b, c > 0$. In particular, the parameter a plays a key role in the isotropic–nematic phase transition, which is usually assumed by $a = A(T - T_*)$, where T is the temperature and T_* is the critical temperature at which the isotropic phase loses stability.

All the (possible) critical points of the bulk energy f_b are given by

$$\mathbf{Q} = s\left(\mathbf{nn} - \frac{1}{3}\mathbf{I}\right), \quad s \in \left\{s_0 = 0, s_\pm = \frac{-b \pm \sqrt{b^2 - 24ac}}{4c}\right\}.$$

Stability or instability of the critical points are shown in Table 2.1, where the three critical temperatures are given by

$$T_c = \frac{b^2}{27Ac} + T_*, \quad T_{II} = \frac{b^2}{24Ac} + T_*. \tag{2.24}$$

The proof of these assertions is straightforward. When the temperature satisfies $T < T_*$, the isotropic state loses stability and the bulk energy is minimized by

Table 2.1. Stability/instability of critical points for LdG energy.

Temperature	Critical points		
	s_0	s_-	s_+
$T < T_*$	unstable	unstable	global minimizer
$T_* < T < T_c$	local minimizer	unstable	global minimizer
$T_c < T < T_{II}$	global minimizer	unstable	local minimizer
$T_{II} < T$	global minimizer	none	none

tensors in the minimal manifold

$$\mathcal{M} = \left\{ s_+\left(\mathbf{nn} - \frac{1}{3}\mathbf{I}\right) : s_+ = \frac{-b + \sqrt{b^2 - 24ac}}{4c}, \mathbf{n} \in \mathbb{S}^2 \right\}. \tag{2.25}$$

One should note that the polynomial energy is phenomenological, that is, the precise physical meaning of coefficients a, b, c is not very clear and cannot easily be determined *a priori*. Moreover, there is no term forcing the tensor to be in the physical space $\mathbb{Q}_{phy}$, and thus $\mathbf{Q}$ may have eigenvalues greater than $2/3$ or less than $-1/3$. Another point that should be taken into account is that the polynomial bulk energy is a finitely truncated Taylor expansion of the real bulk energy around $\mathbf{Q} = 0$. Therefore it is only valid near the isotropic–nematic transition temperature T_*.

To obtain a reliable tensorial model for low-temperature materials (far from the transition point), a natural method is to take the minimal entropy approximation from the molecular energy, which has been applied by Ball and Majumdar (2010). More precisely, for given $\mathbf{Q} \in \mathbb{Q}_{phy}$, one can define the energy as

$$F_b(\mathbf{Q}) = \min_{f \in \mathcal{A}_{\mathbf{Q}}} \int_{\mathbb{S}^2} f(\mathbf{m}) \ln f(\mathbf{m}) - \alpha|\mathbf{Q}|^2, \tag{2.26}$$

where

$$f \in \mathcal{A}_{\mathbf{Q}} = \left\{ f : f \geq 0, \int_{\mathbb{S}^2} f = 1, \int_{\mathbb{S}^2} \left(\mathbf{mm} - \frac{1}{3}\mathbf{I}\right) f = \mathbf{Q} \right\}.$$

The above energy can also be obtained by replacing the orientation distribution function with the Bingham distribution of given second moment $\mathbf{Q}$. In other words, for given $\mathbf{Q} \in \mathbb{Q}_{phy}$, let $\mathbf{B}_{\mathbf{Q}}$ be the unique trace-free symmetric matrix (see Li, Wang and Zhang (2015) for a proof) satisfying

$$\frac{\int_{\mathbb{S}^2} (\mathbf{mm} - \frac{1}{3}\mathbf{I}) \exp(\mathbf{B}_{\mathbf{Q}} : \mathbf{mm}) \, \mathrm{d}\mathbf{m}}{\int_{\mathbb{S}^2} \exp(\mathbf{B}_{\mathbf{Q}} : \mathbf{mm}) \, \mathrm{d}\mathbf{m}} = \mathbf{Q}, \tag{2.27}$$

and let the Bingham distribution $f_{\mathbf{Q}}$ be given by

$$f_{\mathbf{Q}}(\mathbf{m}) = \frac{\exp(\mathbf{B}_{\mathbf{Q}} : \mathbf{mm})}{Z_{\mathbf{Q}}}, \quad Z_{\mathbf{Q}} = \int_{\mathbb{S}^2} \exp(\mathbf{B}_{\mathbf{Q}} : \mathbf{mm}). \tag{2.28}$$

Then the minimum in (2.26) is attained by $f_{\mathbf{Q}}$, that is,

$$F_b(\mathbf{Q}) = \int_{\mathbb{S}^2} f_{\mathbf{Q}}(\mathbf{m}) \ln f_{\mathbf{Q}}(\mathbf{m}) - \alpha|\mathbf{Q}|^2 = \mathbf{B}_{\mathbf{Q}} : \mathbf{Q} - \ln Z_{\mathbf{Q}} - \alpha|\mathbf{Q}|^2.$$

Indeed, note that for a fixed second moment $\mathbf{Q}$, the minimum is achieved by the distribution satisfying

$$\ln f - \mathbf{B} : \mathbf{mm} = \mathrm{c},$$

for some constant c and trace-free symmetric matrix $\mathbf{B}$, which implies that f must take the form (2.28) with $\mathbf{B}$ given by (2.27).

On the other hand, for any $\mathbf{B} \in \mathbb{Q}$, let

$$\omega(\mathbf{B}) = \ln \int_{\mathbb{S}^2} \exp(\mathbf{B} : \mathbf{mm})\, \mathrm{d}\mathbf{m}$$

be a convex function for $\mathbf{B}$; then the entropy part $\mathbf{B}_{\mathbf{Q}} : \mathbf{Q} - \ln Z_{\mathbf{Q}}$ is equal to

$$\max_{\mathbf{B} \in \mathbb{Q}} \{\mathbf{B} : \mathbf{Q} - \omega(\mathbf{B})\},$$

which is the Legendre transform of the function $\omega(\mathbf{B})$. We refer to Li *et al.* (2015) for detailed discussions.

To capture the inhomogeneity of the alignment of LC molecules, one has to take into consideration the elastic energy. The formulation of the elastic energy should be frame-indifferent and usually it is assumed to be quadratic in $\nabla\mathbf{Q}$. Some examples are $V_i = V_i(\mathbf{Q}, \nabla\mathbf{Q})$:

$$V_1 = Q_{ij,k}Q_{ij,k}, \quad V_2 = Q_{ij,j}Q_{ik,k}, \quad V_3 = Q_{ij,k}Q_{ik,j}, \quad V_4 = Q_{ij}Q_{ik,l}Q_{jk,l}.$$

The difference $V_2 - V_3$ can be written as $\partial_k(Q_{ik}Q_{ij,j} - Q_{ij}Q_{ik,j})$, which is a null Lagrangian. The following energy form is commonly used as the elastic part energy for NLCs:

$$F^{(e)}[\mathbf{Q}, \nabla\mathbf{Q}] = L_1|\nabla\mathbf{Q}|^2 + L_2 Q_{ij,j}Q_{ik,k} + L_3 Q_{ik,j}Q_{ij,k} + L_4 Q_{lk}Q_{ij,k}Q_{ij,l}. \tag{2.29}$$

The L_2–L_4 terms correspond to the anisotropic elasticity of LC materials.

Formally, if we force $\nabla\mathbf{Q}(\mathbf{x})$ to minimize the bulk energy in the LdG energy at each point $\mathbf{x}$, then $\mathbf{Q}(\mathbf{x}) = s(\mathbf{n}(\mathbf{x})\mathbf{n}(\mathbf{x}) - \mathbf{I}/3)$, and the full energy reduces to the Oseen–Frank energy (2.13) with the coefficients given by

$$\begin{aligned} k_1 &= 2s^2(2L_1 + L_2 + L_3 - 2sL_4), & k_2 &= 4s^2(L_1 - sL_4), \\ k_3 &= 2s^2(2L_1 + L_2 + L_3 + 4sL_4), & k_4 &= 2s^2(2L_1 + L_3 - sL_4). \end{aligned} \tag{2.30}$$

When $L_4 = 0$, the energy (2.29) is coercive (Longa, Monselesan and Trebin 1987), that is,

$$F^{(e)}[\nabla\mathbf{Q}] \geq c_0|\nabla\mathbf{Q}|^2 \quad \text{for some } c_0 > 0,$$

provided that

$$L_1 > 0, \quad -L_1 < L_3 < 2L_1, \quad L_1 + \frac{5}{3}L_2 + \frac{1}{6}L_3 > 0.$$

On the other hand, if $L_4 \neq 0$, the energy is not bounded from below (Ball and Majumdar 2010). However, if the L_4 term is neglected, due to the form (2.30), we can only recover the Oseen–Frank energy with $k_1 = k_3$.

Defects in the $\mathbf{Q}$-tensor theory are not characterized by singularities of $\mathbf{Q}$. Indeed, for minimizers of the LdG energy with suitable boundary conditions, it is usually smooth everywhere, since the corresponding Euler–Lagrange equation is a semilinear elliptic system. To observe defects, one has to look at the uniaxial limit of the solution. This is reasonable, since the elastic constants are usually small, which means that the bulk energy will force the $\mathbf{Q}$-tensor to be in the minimal manifolds $\mathcal{M}$ defined in (2.25). Singularities of the limit $\mathbf{Q}$-tensor should be regarded as the set of defects. There are a number of results studying the uniaxial limit of minimizers to the LdG energy with certain boundary conditions. We skip to Section 3.1 for further discussions.

2.3.2. *Dynamic* **Q***-tensor models*

The dynamical $\mathbf{Q}$-tensor theories for LCs can be classified into two types. The first are derived directly from physical considerations such as the variational principle. The Beris–Edwards model (Beris and Edwards 1994) and the Qian–Sheng model (Qian and Sheng 1998) belong to this class. Given the free energy $F(\mathbf{Q}, \nabla\mathbf{Q})$, the variation is denoted by

$$\mu_{\mathbf{Q}} = \frac{\delta F(\mathbf{Q}, \nabla\mathbf{Q})}{\delta\mathbf{Q}}.$$

Then the Beris–Edwards model and Qian–Sheng model can be written in the form

$$\frac{\partial\mathbf{Q}}{\partial t} + \mathbf{v}\cdot\nabla\mathbf{Q} = D(\mu_{\mathbf{Q}}) + S(\mathbf{Q}, \mathbf{D}) + \mathbf{\Omega}\cdot\mathbf{Q} - \mathbf{Q}\cdot\mathbf{\Omega}, \tag{2.31}$$

$$\frac{\partial\mathbf{v}}{\partial t} + \mathbf{v}\cdot\nabla\mathbf{v} = -\nabla p + \nabla\cdot(\sigma^{dis} + \sigma^{s} + \sigma^{a} + \sigma^{d}), \tag{2.32}$$

$$\nabla\cdot\mathbf{v} = 0,$$

where $D(\mu_{\mathbf{Q}})$ is the diffusion term, $S(\mathbf{Q},\mathbf{D})$ is the velocity-induced term, σ^d is the distortion stress, σ^a is the anti-symmetric part of orientational-induced stress, $\sigma^s = \gamma S(\mathbf{Q},\mu_{\mathbf{Q}})$ is the symmetric stress induced by the molecular alignments, which conjugates to $S(\mathbf{Q},\mathbf{D})$ (γ is a constant), and σ^{dis} is the additional dissipation stress.

In both systems, modulo some constants, σ^a and σ^d are the same:

$$\sigma^d_{ij} = \frac{\partial E(\mathbf{Q},\nabla\mathbf{Q})}{\partial(\mathbf{Q}_{kl,j})}\mathbf{Q}_{kl,i}, \quad \sigma^a = \mathbf{Q}\cdot\mu_{\mathbf{Q}} - \mu_{\mathbf{Q}}\cdot\mathbf{Q}.$$

In the Beris–Edwards system the other terms are given by

$$D_{BE} = -\Gamma\mu_{\mathbf{Q}}, \quad \sigma^{dis}_{BE} = \beta\mathbf{D}, \quad \sigma^s_{BE} = S_{BE}(\mathbf{Q},\mu_{\mathbf{Q}}),$$
$$S_{BE}(\mathbf{Q},A) = \xi\left(\left(\mathbf{Q}+\frac{1}{3}\mathrm{Id}\right)\cdot A + A\cdot\left(\mathbf{Q}+\frac{1}{3}\mathrm{Id}\right) - 2\left(\mathbf{Q}+\frac{1}{3}\mathrm{Id}\right)(A:\mathbf{Q})\right),$$

while in the Qian–Sheng system they are given by

$$D_{QS} = -\Gamma\mu_{\mathbf{Q}}, \quad \sigma^s_{QS} = -\frac{1}{2}\frac{\mu_2^2}{\mu_1}\mu_{\mathbf{Q}}, \quad S_{QS}(\mathbf{Q},\mathbf{D}) = -\frac{1}{2}\frac{\mu_2}{\mu_1}\mathbf{D},$$
$$\sigma^{dis}_{QS} = \beta_1\mathbf{Q}(\mathbf{Q}:\mathbf{D}) + \beta_2\mathbf{D} + \beta_3(\mathbf{Q}\cdot\mathbf{D}+\mathbf{D}\cdot\mathbf{Q}).$$

We remark that in Qian and Sheng's original formulation, the inertial effect is also considered.

Another kind of dynamical **Q**-tensor model is obtained by various closure approximations from Doi's kinetic theory. The main idea is to derive the evolution equation for the second moment **Q** from the evolution equation for the orientation distribution function f. This is a natural form of model reduction, and the parameters can be calculated from the kinetic equations rather than being phenomenologically determined. However, by a direct calculation, one can find that the evolution of **Q** depends on the fourth moment of f, which cannot be determined by **Q**. In order to 'close' the equation at the level of the second moment tensor, one needs to represent the fourth moment by **Q** approximately. Doi introduced the simplest approximation:

$$\langle\mathbf{mmmm}\rangle_f = \langle\mathbf{mm}\rangle_f\langle\mathbf{mm}\rangle_f.$$

Various other closure methods have been presented, such as the HL1/HL2 closure (Hinch and Leal 1976) and the Bingham closure (Chaubal and Leal 1998). We refer to Feng, Chaubal and Leal (1998) for a summary and a comparison between these closure methods. All of these models can capture many qualitative features of the LC dynamics effectively. However, they do not obey the energy dissipation law.

2.3.3. *A systematic way to derive new* **Q***-tensor models*

Han *et al.* (2015) proposed a systematic way to derive a **Q**-tensor model from the molecular theory. The main idea can be explained as follows. We start from the non-local Onsager molecular energy functional (2.8) with suitable given interaction kernel $\mathcal{B}_\varepsilon$, and then approximate the orientation distribution function by a suitable function of its second moment. Then the energy can be entirely determined by the second moment and is thus reduced to a **Q**-tensor type model. This procedure can be used not only for the nematics but also other phases for rod-like molecules and even other shapes (Xu and Zhang 2014, Xu, Ye and Zhang 2018, Xu and Zhang 2018).

For NLCs, we choose Onsager's energy functional (2.8), with $\mathcal{B}_\varepsilon$ being the excluded volume potential (2.9). Note that $\mathcal{B}_\varepsilon$ is translation-invariant, so we let $B(\mathbf{x}-\mathbf{x}',\mathbf{m},\mathbf{m}') = \mathcal{B}_\varepsilon(\mathbf{x},\mathbf{m};\mathbf{x}',\mathbf{m}')$, which is even in $\mathbf{x}-\mathbf{x}'$.

Make the Taylor expansion for the orientational distribution function $f(\mathbf{x}',\mathbf{m}')$ with respect to $\mathbf{x}'$ at $\mathbf{x}$ ($\mathbf{r}=\mathbf{x}'-\mathbf{x}$):

$$\begin{aligned} f(\mathbf{x}',\mathbf{m}') &= f(\mathbf{x}+\mathbf{r},\mathbf{m}') \\ &= f(\mathbf{x},\mathbf{m}') + \nabla f(\mathbf{x},\mathbf{m}')\cdot\mathbf{r} + \frac{1}{2}\nabla^2 f(\mathbf{x},\mathbf{m}') : \mathbf{r}^\top\mathbf{r} + \cdots . \end{aligned} \tag{2.33}$$

Then the energy can be expanded as

$$\begin{aligned} A[f] = \int_\Omega\int_{\mathbb{S}^2} \biggl\{ & f(\mathbf{x},\mathbf{m})(\ln f(\mathbf{x},\mathbf{m})-1) \\ & + \frac{1}{2}\int_{\mathbb{S}^2} M^{(0)}(\mathbf{m},\mathbf{m}') f(\mathbf{x},\mathbf{m}') f(\mathbf{x},\mathbf{m})\,\mathrm{d}\mathbf{m}' \biggr\}\,\mathrm{d}\mathbf{m}\,\mathrm{d}\mathbf{x} \\ & + \frac{1}{2}\int_\Omega\int_{\mathbb{S}^2}\int_{\mathbb{S}^2} f(\mathbf{x},\mathbf{m}) M^{(1)}(\mathbf{m},\mathbf{m}')\cdot\nabla f(\mathbf{x},\mathbf{m}')\,\mathrm{d}\mathbf{m}'\,\mathrm{d}\mathbf{m}\,\mathrm{d}\mathbf{x} \\ & - \frac{1}{4}\int_\Omega\int_{\mathbb{S}^2}\int_{\mathbb{S}^2} M^{(2)}(\mathbf{m},\mathbf{m}') : \nabla f(\mathbf{x},\mathbf{m}')\nabla f(\mathbf{x},\mathbf{m})\,\mathrm{d}\mathbf{m}'\,\mathrm{d}\mathbf{m}\,\mathrm{d}\mathbf{x} + \cdots , \end{aligned} \tag{2.34}$$

where, for a given kernel function $B(\mathbf{r};\mathbf{m},\mathbf{m}')$, the moments $M^{(k)}(\mathbf{m},\mathbf{m}')$ ($k = 0,1,2,\ldots$) are defined by

$$\begin{aligned} M^{(0)}(\mathbf{m},\mathbf{m}') &= \int B(\mathbf{r},\mathbf{m},\mathbf{m}')\,\mathrm{d}\mathbf{r}, \\ M^{(k)}(\mathbf{m},\mathbf{m}') &= \int B(\mathbf{r},\mathbf{m},\mathbf{m}')\,\underbrace{\mathbf{r}\otimes\cdots\otimes\mathbf{r}}_{k\text{ times}}\,\mathrm{d}\mathbf{r} \quad (k \geq 1). \end{aligned}$$

These moments depend on the geometric shape of LC molecules. For nematic molecules, they are commonly treated as ellipsoids or spherocylinders. Han *et al.* (2015) explicitly calculated the first three moments by considering the molecules as spherocylinders with length L and diameter D:

$$\begin{aligned} M^{(0)}(\mathbf{m},\mathbf{m}') &= 2L^3\left(\eta|\mathbf{m}\times\mathbf{m}'| + \pi\eta^2 + \frac{2}{3}\pi\eta^3\right),\\ M^{(1)}(\mathbf{m},\mathbf{m}') &= 0,\\ M^{(2)}(\mathbf{m},\mathbf{m}') &= B_1\mathbf{I} + B_2(\mathbf{mm}+\mathbf{m}'\mathbf{m}') + B_3(\mathbf{mm}'+\mathbf{m}'\mathbf{m})(\mathbf{m}\cdot\mathbf{m}'), \end{aligned}$$

where $\eta = D/L$ and B_i are functions of $\mathbf{m}\cdot\mathbf{m}'$ (for details see Han *et al.* 2015, Appendix):

$$\begin{cases} B_1(\mathbf{m}\cdot\mathbf{m}') = L^4D\left(\dfrac{2|\mathbf{m}\times\mathbf{m}'|\eta^2}{3} + \dfrac{\pi\eta^3}{2} + \dfrac{4\pi\eta^4}{15}\right),\\ B_2(\mathbf{m}\cdot\mathbf{m}') = L^4D\left(\dfrac{|\mathbf{m}\times\mathbf{m}'|}{6} + \dfrac{\pi\eta(1+\eta)}{3} + \dfrac{\pi\eta^3}{4} + \dfrac{2\eta^2}{3|\mathbf{m}\times\mathbf{m}'|}\right),\\ B_3(\mathbf{m}\cdot\mathbf{m}') = L^4D\eta^2\left(\dfrac{2\arcsin(\mathbf{m}\cdot\mathbf{m}')}{3(\mathbf{m}\cdot\mathbf{m}')} - \dfrac{2}{3|\mathbf{m}\times\mathbf{m}'|}\right). \end{cases}$$

The first line in (2.34) is independent of space variation of the probability distribution function f, which gives the bulk energy part. The other terms, which depend on space variation of f, provide the elastic part of the free energy.

To derive tensor models from molecular models, we need to use $\mathbf{Q}(x)$ to express the total energy. Since it is unrealistic to recover f by a finite number of moments, we need to make closure approximation. We choose the Bingham closure here because it keeps physical constraints on the eigenvalues and preserves the energy structure for dynamics. We also take the density variation into consideration, that is,

$$f(\mathbf{x},\mathbf{m}) = c(\mathbf{x})f_{\mathbf{Q}}(\mathbf{m}), \quad \text{with } f_{\mathbf{Q}} \text{ given by (2.28).} \tag{2.35}$$

The bulk energy is then approximated by

$$\begin{aligned} F_{bulk} = \int_\Omega \biggl\{ & c(\mathbf{x})\ln c(\mathbf{x}) + c(\mathbf{x})\int_{\mathbb{S}^2}(f_{\mathbf{Q}}(\mathbf{x},\mathbf{m})(\ln f_{\mathbf{Q}}(\mathbf{x},\mathbf{m})-1))\,\mathrm{d}\mathbf{m}\\ & + \frac{c^2(x)}{2}\int_{\mathbb{S}^2} M^{(0)}(\mathbf{m},\mathbf{m}')f_{\mathbf{Q}}(\mathbf{x},\mathbf{m}')f_{\mathbf{Q}}(\mathbf{x},\mathbf{m})\,\mathrm{d}\mathbf{m}'\,\mathrm{d}\mathbf{m}\biggr\}\,\mathrm{d}\mathbf{x}. \end{aligned} \tag{2.36}$$

Note that the above energy can be viewed as a functional of $c(\mathbf{x})$ and $\mathbf{Q}(\mathbf{x})$. If the singular term $|\mathbf{m}\times\mathbf{m}'|$ in $M^{(0)}(\mathbf{m},\mathbf{m}')$ is replaced by its smooth alternative $|\mathbf{m}\times\mathbf{m}'|^2$, we may arrive at

$$F_{bulk} = \int_\Omega c(\mathbf{x})(\ln c(\mathbf{x}) + \mathbf{Q}(\mathbf{x})\colon \mathbf{B}_{\mathbf{Q}}(\mathbf{x}) - \ln Z_{\mathbf{Q}}(\mathbf{x}) - \alpha L^3 c(\mathbf{x})|\mathbf{Q}(\mathbf{x})|^2)\mathrm{d}\mathbf{x},$$

where α is a dimensionless constant.

To derive an elastic energy convenient to use, we consider only finite terms in (2.34). For the nematic phase, it is natural to neglect terms whose derivatives are of order greater than one since the first-order derivatives dominate the elastic energy part. If one would like to consider the smectic phase, it seems enough to keep only the terms whose derivatives are of order no greater than two.

Now we need to express

$$\int_{\mathbb{S}^2}\int_{\mathbb{S}^2} f_{\mathbf{Q}}(\mathbf{x},\mathbf{m})M^{(2)}(\mathbf{m},\mathbf{m}')f_{\mathbf{Q}}(\mathbf{x},\mathbf{m}')\,\mathrm{d}\mathbf{m}'\,\mathrm{d}\mathbf{m}' \tag{2.37}$$

in terms of the tensor $\mathbf{Q}$. Thus we have to separate the variables of $\mathbf{m}$ and $\mathbf{m}'$ in $M^{(l)}(\mathbf{m},\mathbf{m}')$. This cannot be done precisely in general, since there are some terms like $|\mathbf{m}\times\mathbf{m}'|$. One has to treat them as functions of $\mathbf{m}\cdot\mathbf{m}'$ and use polynomial expansions, such as Taylor expansions or Legendre polynomial expansions, up to a finite order, to approximate them. We skip the details and just present the reduced elastic energy after approximating:

$$\begin{aligned}F_{elastic} = \frac{1}{2}\int_{\Omega}\Big\{&J_1|\nabla c|^2 + J_2|\nabla(c\mathbf{Q})|^2 + J_3|\nabla(c\mathbf{Q}_4)|^2 + J_4\partial_i(cQ_{ij})\partial_j c\\&+ J_5(\partial_i(cQ_{ik})\partial_j(cQ_{jk}) + \partial_i(cQ_{jk})\partial_j(cQ_{ik}))\\&+ J_6(\partial_i(cQ_{4iklm})\partial_j(cQ_{4jklm}) + \partial_i(cQ_{4jklm})\partial_j(cQ_{4iklm}))\\&+ J_7\partial_i(cQ_{4ijkl})\partial_j(cQ_{kl})\Big\}\,\mathrm{d}\mathbf{x}.\end{aligned} \tag{2.38}$$

Here $\mathbf{Q}_4 = \mathbf{Q}_4[f_{\mathbf{Q}}]$ is defined in (A.1). The coefficients $J_i(1 \le i \le 7)$ depend only on parameters L,η and can be explicitly calculated. Combining (2.36) and (2.38), we obtain an energy in tensorial form derived from Onsager's molecular theory:

$$F^{Mol}(c,\mathbf{Q},\nabla c,\nabla\mathbf{Q}) = F_{bulk} + F_{elastic}.$$

The density variation can be neglected in most cases, especially when defects are absent. Then the energy can be further simplified into a form that depends only on $\mathbf{Q}$ and $\nabla\mathbf{Q}$.

If we further assume the uniaxiality of the $\mathbf{Q}$-tensor, then we obtain a vector model with elastic coefficients given by molecular parameters. We refer to Han *et al.* (2015) for details. The procedure of reduction from microscopic molecular theories to macroscopic continuum theories is illustrated in Figure 2.2. The microscopic interpretation of elastic coefficients in the Oseen–Frank theory has also been studied in Gelbart and Ben-Shaul (1982) and many other related works.

A similar procedure can be applied to derive the dynamical equation based on the dynamical Doi–Onsager equation. The main step is to calculate the evolution of $\mathbf{Q}$ from the evolution equation for f. For simplicity of presentation, we assume the density is constant and assume the energy takes the simplest form:

$$F(\mathbf{Q}) = \int \mathbf{Q}(\mathbf{x}) : \mathbf{B}_{\mathbf{Q}}(\mathbf{x}) - \ln Z_{\mathbf{Q}}(\mathbf{x}) - \frac{\alpha}{2}\mathbf{Q}(\mathbf{x}) : \mathbf{Q}^{\varepsilon}(\mathbf{x})\,\mathrm{d}\mathbf{x}, \tag{2.39}$$

with

$$\mathbf{Q}^{\varepsilon} = \int_{\mathbb{R}^3} g_{\varepsilon}(\mathbf{x}-\mathbf{x}')\mathbf{Q}(\mathbf{x}')\,\mathrm{d}\mathbf{x}'.$$

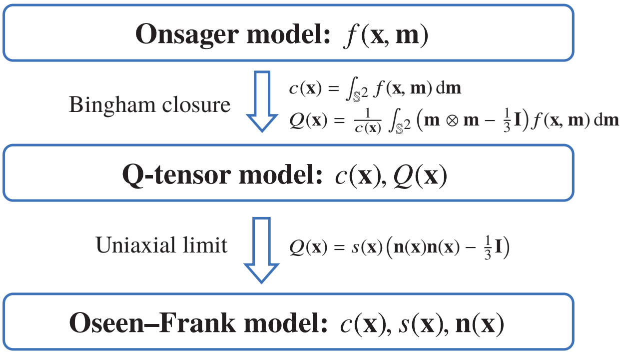

Figure 2.2. Reduction from microscopic molecular theories to macroscopic continuum theories.

This energy can be derived directly from the Onsager energy functional (2.8) with non-local Maier–Saupe potential (2.10).

As higher-order moments will be involved, we also replace them with the corresponding moments of the approximated Bingham distribution. Namely, we denote

$$M_{\mathbf{Q}}^{(4)} = \int_{\mathbb{S}^2} \mathbf{mmmm} f_{\mathbf{Q}}\,\mathrm{d}\mathbf{m}, \quad M_{\mathbf{Q}}^{(6)} = \int_{\mathbb{S}^2} \mathbf{mmmmmm} f_{\mathbf{Q}}\,\mathrm{d}\mathbf{m},$$

and

$$\begin{aligned}
\mathcal{M}_{\mathbf{Q}}(A) &= \frac{1}{3}A + \mathbf{Q}\cdot A - A : M_{\mathbf{Q}}^{(4)},\\
\mathcal{N}_{\mathbf{Q}}(A)_{\alpha\beta} &= \partial_i\bigg\{\bigg[\gamma_\perp\bigg(M^{(4)}_{\mathbf{Q}\alpha\beta kl}\delta_{ij} - \frac{\delta_{\alpha\beta}}{3}Q_{kl}\delta_{ij}\bigg)\\
&\quad + (\gamma_\parallel - \gamma_\perp)\bigg(M^{(6)}_{Q\alpha\beta klij} - \frac{\delta_{\alpha\beta}}{3}M^{(4)}_{Qklij}\bigg)\bigg]\partial_j A_{kl}\bigg\}.
\end{aligned}$$

We also let

$$\mu_{\mathbf{Q}} := \frac{\delta F(\mathbf{Q})}{\delta\mathbf{Q}} = B_{\mathbf{Q}} - \alpha\mathbf{Q}^{\varepsilon}.$$

Noting that

$$3\mathbf{Q} = 2\alpha\mathcal{M}_{\mathbf{Q}}(B_{\mathbf{Q}}),$$

we can obtain a closed **Q**-tensor system from the Doi–Onsager equation (2.11):

$$\begin{aligned}
\frac{\partial\mathbf{Q}}{\partial t} + \mathbf{v}\cdot\nabla\mathbf{Q} &= \frac{\varepsilon}{De}\mathcal{N}_{\mathbf{Q}}(\mu_{\mathbf{Q}}) - \frac{2}{De}(\mathcal{M}_{\mathbf{Q}} + \mathcal{M}_{\mathbf{Q}}^{\top})(\mu_{\mathbf{Q}}) + (\mathcal{M}_{\mathbf{Q}} + \mathcal{M}_{\mathbf{Q}}^{\top})(\kappa^{\top}),\\
\frac{\partial\mathbf{v}}{\partial t} + \mathbf{v}\cdot\nabla\mathbf{v} &= -\nabla p + \frac{\gamma}{Re}\Delta\mathbf{v} + \frac{1-\gamma}{2Re}\nabla\cdot(\mathbf{D} : M_{\mathbf{Q}}^{(4)})\\
&\quad + \frac{1-\gamma}{DeRe}(2\nabla\cdot\mathcal{M}_{\mathbf{Q}}(\mu_{\mathbf{Q}}) + \mathbf{Q} : \nabla\mu_{\mathbf{Q}}).
\end{aligned} \tag{2.40}$$

The system (2.40) obeys the following energy dissipation law:

$$\begin{aligned}\frac{\mathrm{d}}{\mathrm{d}t}&\left\{\int_{\mathbb{R}^3}\frac{1}{2}|\mathbf{v}|^2\,\mathrm{d}x+\frac{1-\gamma}{ReDe}F(Q)\right\}\\&=-\frac{1}{Re}\int_{\mathbb{R}^3}\left\{\gamma|\mathbf{D}|^2+\frac{1-\gamma}{2}M^{(4)}_{\mathbf{Q}}:(\mathbf{D}\otimes\mathbf{D})\right.\\&\qquad\left.-\frac{\varepsilon(1-\gamma)}{De^2}\mu_{\mathbf{Q}}:\mathcal{N}\mu_{\mathbf{Q}}+\frac{4(1-\gamma)}{De^2}\mu_{\mathbf{Q}}:\mathcal{M}_{\mathbf{Q}}\mu_{\mathbf{Q}}\right\}\mathrm{d}x.\end{aligned}$$

We can also replace the energy (2.39) in (2.40) with a general local energy $F(\mathbf{Q},\nabla\mathbf{Q})$ to obtain a dynamical system in local form. The energy law is kept regardless of the particular choice of $F(\mathbf{Q},\nabla\mathbf{Q})$.

Since the system (2.40) is derived from the Doi–Onsager equation by the Bingham closure, it keeps many important physical properties. First, the system preserves the energy structure, which is violated by other closure models. Second, the parameters have definite physical meaning as opposed to being phenomenologically determined. Third, the eigenvalues of $\mathbf{Q}$ satisfy the physical constraint: $\lambda_i\in\{-1/3,\ 2/3\}$ $(i=1,2,3)$ if they are satisfied initially. Moreover, both translational and rotational diffusion can be kept in the formulation, and the translational diffusion can be anisotropic.

Finally, we make some comparisons between the system (2.40) with the Beris–Edward and Qian–Sheng models. The system (2.40) can be written similarly to (2.31)–(2.32):

$$\begin{aligned}\frac{\partial\mathbf{Q}}{\partial t}+\mathbf{v}\cdot\nabla\mathbf{Q}&=D(\mu_{\mathbf{Q}})+S(\mathbf{Q},\mathbf{D})+\mathbf{\Omega}\cdot\mathbf{Q}-\mathbf{Q}\cdot\mathbf{\Omega},\\\frac{\partial\mathbf{v}}{\partial t}+\mathbf{v}\cdot\nabla\mathbf{v}&=-\nabla p+\nabla\cdot(\sigma^{dis}+\sigma^s+\sigma^a+\sigma^d),\\\nabla\cdot\mathbf{v}&=0.\end{aligned}\tag{2.41}$$

Here

$$D(\mu_{\mathbf{Q}})=\frac{\varepsilon}{De}\mathcal{N}(\mu_{\mathbf{Q}})+\frac{2}{De}(\mathcal{M}_{\mathbf{Q}}+\mathcal{M}_{\mathbf{Q}}^{\top})(\mu_{\mathbf{Q}}),$$

where the first and second terms account for the translational and rotational diffusion respectively. In the Beris–Edwards and Qian–Sheng models, the diffusion term is simply taken as $\lambda\mu_Q$, which is different to the choice here. We remark that $\mu_{\mathbf{Q}}:\nabla\mathbf{Q}$ is equivalent to

$$\partial_j\left(\frac{\partial F}{\partial(Q_{kl,j})}Q_{kl,i}\right)$$

modulo a pressure term, and

$$(\mathcal{M}_{\mathbf{Q}}-\mathcal{M}_{\mathbf{Q}}^{\top})(\mu_{\mathbf{Q}})=\mathbf{Q}\cdot\mu_{\mathbf{Q}}-\mu_{\mathbf{Q}}\cdot\mathbf{Q},$$

so the stress terms σ^a and σ^d in our model, modulo some constants, are the same as in those two models:

$$\sigma^d_{ij} = \frac{\partial F(\mathbf{Q}, \nabla\mathbf{Q})}{\partial(Q_{kl,j})} Q_{kl,i}, \quad \sigma^a = \mathbf{Q}\cdot\mu_{\mathbf{Q}} - \mu_{\mathbf{Q}}\cdot\mathbf{Q}. \tag{2.42}$$

The dissipation stress is given by

$$\sigma^{dis} = \frac{2\gamma}{Re}\mathbf{D} + \frac{1-\gamma}{2Re}\mathbf{D} : M^{(4)}_{\mathbf{Q}}.$$

The two conjugated terms $S(\mathbf{Q}, \mathbf{D})$ and

$$\sigma^s = -\frac{1-\gamma}{ReDe} S(\mathbf{Q}, \mu_{\mathbf{Q}})$$

are given by

$$S(\mathbf{Q}, A) = (\mathcal{M}_{\mathbf{Q}} + \mathcal{M}^\top_{\mathbf{Q}})(A).$$

Note that if we apply Doi's closure $\langle\mathbf{mmmm}\rangle_f \sim \langle\mathbf{mm}\rangle_f\langle\mathbf{mm}\rangle_f$ in $M^{(4)}_{\mathbf{Q}}$, then

$$(\mathcal{M}_{\mathbf{Q}} + \mathcal{M}^\top_{\mathbf{Q}})(A) \sim \left(\mathbf{Q} + \frac{1}{3}\mathrm{Id}\right)\cdot A + A\cdot\left(\mathbf{Q} + \frac{1}{3}\mathrm{Id}\right) - 2\left(\mathbf{Q} + \frac{1}{3}\mathrm{Id}\right)(A : \mathbf{Q}),$$

which is indeed the corresponding term $S_{BE}(\mathbf{Q}, A)$ in the Beris–Edwards system with $\xi = 1$.

3. Mathematical analysis for different liquid crystal models

In this section we review some analysis results for various LC models. Since there has been great progress in this active area, we do not intend to cover all topics but instead concentrate on the analysis of defects, the well-posedness theory of dynamical theories, and the connections between them. Some of them were introduced in Section 2 and will not be presented again.

3.1. *Analysis of defects*

The LdG model and Oseen–Frank model have been widely used to study the properties of equilibrium configurations under various conditions.

In vector theories, the simplest configuration containing a defect is

$$\mathbf{n}(\mathbf{x}) = \frac{\mathbf{x}}{|\mathbf{x}|}, \tag{3.1}$$

known as the hedgehog. It is not hard to verify that the hedgehog is always a weak solution of the Euler–Lagrange equation for any choice of k_i. For the stability, it has been proved that the hedgehog is stable if $8(k_2 - k_1) + k_3 \geq 0$ (Cohen and Taylor 1990) and not stable if $8(k_2 - k_1) + k_3 < 0$ (Hélein 1987). One can construct other typical configurations of point defects. For example, in the one-constant case, for any $\mathbf{R} \in O(3)$,

$$\mathbf{n}(\mathbf{x}) = \mathbf{R}\frac{\mathbf{x}}{|\mathbf{x}|}$$

is always a solution of the Euler–Lagrange equation. Moreover, it is always stable (Brezis, Coron and Lieb 1986). For the general case, the choice of $\mathbf{R}$ is limited. If $k_1 = k_3$, $\mathbf{R}$ has to be $\pm\mathbf{I}$ or any 180° rotation. When the k_i are distinct, $\mathbf{R}$ must be $\pm\mathbf{I}$. The corresponding stability has been analysed by Kinderlehrer, Walkington and Ou (1993).

Moreover, by considering a suitable surface energy, the free boundary problems have also been analytically studied to explore optimal shapes of LC droplets (Lin and Poon 1996, Shen, Liu and Calderer 2002). For more results on the analysis of the Oseen–Frank and related models, we refer to the survey paper by Lin and Liu (2001).

The vector theory can provide macroscopic information on the alignment for the defect configuration, whereas in order to study the fine structure of defect cores we need to use $\mathbf{Q}$-tensor models. Given the boundary condition $\mathbf{Q}(\mathbf{x}) = s_+(\mathbf{n}(\mathbf{x})\mathbf{n}(\mathbf{x}) - \frac{1}{3}\mathbf{I})$ with $\mathbf{n}(\mathbf{x})$ given by (3.1), three kinds of equilibrium solution are found numerically (Mkaddem and Gartland Jr 2000), which are called radial hedgehog, ring disclination and split core respectively. These solutions are illustrated in Figure 4.1(a–c). Recently, in the low-temperature limit, Yu (2020) proved the existence of axially symmetric solutions describing ring disclination and split core.

The radial hedgehog solution in the ball $B_R(0)$ can be represented in the form

$$\mathbf{Q}(\mathbf{x}) = h(|\mathbf{x}|)\left(\mathbf{n}(\mathbf{x})\mathbf{n}(\mathbf{x}) - \frac{1}{3}\mathbf{I}\right), \quad \mathbf{n}(\mathbf{x}) = \frac{\mathbf{x}}{|\mathbf{x}|}, \tag{3.2}$$

where h satisfies the ODE

$$h''(r) + \frac{2}{r}h'(r) - \frac{6}{r^2}h(r) = ah(r) - \frac{b}{3}h^2 + \frac{2c}{3}h^3, \tag{3.3}$$

$$h(0) = 0, \quad h(R) = s_+. \tag{3.4}$$

Gartland Jr and Mkaddem (1999) proved the instability of the radial hedgehog solution (3.2) when the temperature a is very low and the radius R of the ball is large. Majumdar (2012) proved that if a is closed to zero or R is small, the radial hedgehog solution is locally stable. For the whole space case, *i.e.* $R = \infty$, Ignat, Nguyen, Slastikov and Zarnescu (2015) showed that the radial hedgehog solution is locally stable for a closed to zero and unstable for large $|a|$. The monotonicity and uniqueness of the solution h to (3.3) is studied in Lamy (2013).

As defects in $\mathbf{Q}$-tensor theory are not the singularities of order tensor $\mathbf{Q}$ but the regions with rapid changes of $\mathbf{Q}$, one may study the uniaxial limit of LdG model to analyse the properties of defect sets. Most of these results concentrate on the case $L_2 = L_3 = L_4 = 0$, $L_1 = L$.

Consider the strong anchoring boundary condition

$$\mathbf{Q}|_{\partial\Omega} = s_+\left(\mathbf{n}_b(\mathbf{x})\mathbf{n}_b(\mathbf{x}) - \frac{1}{3}\mathbf{I}\right), \quad \mathbf{n}_b \in C^\infty(\partial\Omega, \mathbb{S}^2). \tag{3.5}$$

Let $\mathbf{Q}^L$ be the global minimizers of the Landau–de Gennes energy

$$F_L(\mathbf{Q}, \nabla\mathbf{Q}) = \int_\Omega \frac{L}{2}|\nabla\mathbf{Q}|^2 + \frac{a}{2}|\mathbf{Q}|^2 - \frac{b}{3}\operatorname{tr}\mathbf{Q}^3 + \frac{c}{4}|\mathbf{Q}|^4 \,\mathrm{d}\mathbf{x},$$

with boundary condition (3.5). Majumdar and Zarnescu (2010) proved the following results.

Theorem 3.1. For a sequence $L_k \to 0$, the minimizers $\mathbf{Q}^{L_k} \to \mathbf{Q}_*$ in the Sobolev space $H^1(\Omega)$, where $\mathbf{Q}_* \in H^1(\Omega, \mathcal{M})$ is the minimizer of

$$\int_\Omega |\nabla\mathbf{Q}|^2 \,\mathrm{d}\mathbf{x}, \quad \text{with } \mathbf{Q} \in \mathcal{M} \text{ and satisfying (3.5).}$$

In addition, the convergence is uniform away from the (possible) singularities of $\mathbf{Q}_*$.

Moreover, away from the singular points of $\mathbf{Q}_*$, the convergence was further refined by Nguyen and Zarnescu (2013). Note that the fact that the limit map $\mathbf{Q}_* \in H^1(\Omega)$ implies the line defects is excluded in this case.

Bauman, Park and Phillips (2012) investigated the uniaxial limit of the Landau–de Gennes energy with $L_2, L_3 \neq 0$ on a 2D bounded domain. By assuming that $\mathbf{e}_3$ is always an eigenvector of $\mathbf{Q}$, they proved that if the boundary data have non-zero degree, then there will be a finite number of defects of degree $\pm 1/2$. This problem models the behaviour of a thin LC material with its top and bottom surfaces constrained to having a principal axis $\mathbf{e}_3$, and the limiting defects correspond to vertical disclination lines at those locations. The line defects in the full three-dimensional domain have been investigated by Canevari (2017), who proved that the minimizers $\mathbf{Q}^{(L)}$ converge to a limit map with straight line segment singularities, by assuming the logarithmic bound of the energy:

$$F \leq CL|\ln L|.$$

Some related results are also given in Golovaty and Montero (2014) and Canevari (2015).

3.2. *Relation between the non-local Onsager energy and the Oseen–Frank energy*

The orientation distribution function f contains detailed configurational information on molecules. However, it is difficult to apply, especially when studying the macroscopic behaviour of configurations, as it often leads to very high computational costs. Thus the **Q**-tensor theory and the Ericksen–Leslie theory are used more often in analysis and computational simulations. Then it raises a natural question: Are these models consistent with each other? This issue is fundamental but highly non-trivial from the analysis perspective.

We briefly show how to derive it formally. We expand the mean-field potential as

$$\mathcal{U}_\varepsilon f = U_0[f] + \varepsilon U_1[f] + \varepsilon^2 U_2[f] + \cdots, \tag{3.6}$$

where $U_0[f] = \mathcal{U}f$ and for $k \geq 1$

$$U_k[f](\mathbf{x},\mathbf{m},t) = \frac{1}{(2k)!}\int_{\mathbb{R}^3}\int_{\mathbb{S}^2} \alpha|\mathbf{m}\times\mathbf{m}'|^2 g(\mathbf{y})(\mathbf{y}\cdot\nabla)^{2k} f(\mathbf{x},\mathbf{m}',t)\,\mathrm{d}\mathbf{m}'\,\mathrm{d}\mathbf{y}.$$

Direct computation shows that

$$\begin{aligned}\mathcal{U}_\varepsilon[f] - U[f] &= \int_{\mathbb{R}^3}\int_{\mathbb{S}^2} \alpha|\mathbf{m}\times\mathbf{m}'|^2 g_\varepsilon(\mathbf{x}-\mathbf{x}')(f(\mathbf{x}',\mathbf{m}',t) - f(\mathbf{x},\mathbf{m}',t))\,\mathrm{d}\mathbf{m}'\,\mathrm{d}\mathbf{x}'\\
&= \int_{\mathbb{R}^3}\int_{\mathbb{S}^2} \alpha|\mathbf{m}\times\mathbf{m}'|^2 g(\mathbf{y})(f(\mathbf{x}+\sqrt{\varepsilon}\mathbf{y},\mathbf{m}',t) - f(\mathbf{x},\mathbf{m}',t))\,\mathrm{d}\mathbf{m}'\,\mathrm{d}\mathbf{y}\\
&= \int_{\mathbb{R}^3}\int_{\mathbb{S}^2} \alpha|\mathbf{m}\times\mathbf{m}'|^2 g(\mathbf{y})\Bigg(\sum_{k\geq 1}\frac{\varepsilon^{k/2}}{k!}(\mathbf{y}\cdot\nabla)^k f(\mathbf{x},\mathbf{m}',t)\Bigg)\,\mathrm{d}\mathbf{m}'\,\mathrm{d}\mathbf{y}\\
&= \int_{\mathbb{R}^3}\int_{\mathbb{S}^2} \alpha|\mathbf{m}\times\mathbf{m}'|^2 g(\mathbf{y})\Bigg(\sum_{k\geq 1}\frac{\varepsilon^{k}}{(2k)!}(\mathbf{y}\cdot\nabla)^{2k} f(\mathbf{x},\mathbf{m}',t)\Bigg)\,\mathrm{d}\mathbf{m}'\,\mathrm{d}\mathbf{y}.\end{aligned}$$

We let ($U_0[f] = U[f]$):

$$U_k[f](\mathbf{x},\mathbf{m},t) = \frac{1}{(2k)!}\int_{\mathbb{R}^3}\int_{\mathbb{S}^2} \alpha|\mathbf{m}\times\mathbf{m}'|^2 g(\mathbf{y})(\mathbf{y}\cdot\nabla)^{2k} f(\mathbf{x},\mathbf{m}',t)\,\mathrm{d}\mathbf{m}'\,\mathrm{d}\mathbf{y}.$$

Denote

$$\mathbf{M}[f] = \int_{\mathbb{S}^2} m_i m_j f(\mathbf{x},\mathbf{m})\,\mathrm{d}\mathbf{m}, \quad G_{kl} = \int g(\mathbf{y}) y_k y_l\,\mathrm{d}\mathbf{y}.$$

Then

$$U_1[f](\mathbf{x},\mathbf{m}) = -\frac{\alpha}{2}G_{kl}\mathbf{m}\mathbf{m}\colon \partial_k\partial_l\mathbf{M}[f]. \tag{3.7}$$

The energy can then be expanded as

$$\begin{aligned}A_\varepsilon[f] = &\int_\Omega\int_{\mathbb{S}^2} f(\mathbf{x},\mathbf{m})(\ln f(\mathbf{x},\mathbf{m}) - 1) + \frac{1}{2}f(\mathbf{x},\mathbf{m})U_0[f](\mathbf{x},\mathbf{m})\,\mathrm{d}\mathbf{m}\,\mathrm{d}\mathbf{x}\\
&+ \frac{\varepsilon\alpha}{4}\int_\Omega G_{kl}\partial_k\mathbf{M}[f]\colon \partial_l\mathbf{M}[f]\,\mathrm{d}\mathbf{x} + O(\varepsilon^2).\end{aligned} \tag{3.8}$$

The leading-order term is a local energy which can be written as

$$\int_\Omega A_0[f(\mathbf{x},\cdot)]\,\mathrm{d}\mathbf{x}, \tag{3.9}$$

with

$$A_0[f] = \int_{\mathbb{S}^2} f(\mathbf{m})(\ln f(\mathbf{m}) - 1) + \frac{1}{2}f(\mathbf{m})U_0[f]\,\mathrm{d}\mathbf{m}. \tag{3.10}$$

Theorem 2.1 informs us that the global minimizers of the above energy are given by

$$f_0(\mathbf{m}) = h_{\eta,\mathbf{n}}(\mathbf{m}) := \frac{1}{Z}\mathrm{e}^{\eta(\mathbf{m}\cdot\mathbf{n})^2}, \quad Z = \int_{\mathbb{S}^2}\mathrm{e}^{\eta(\mathbf{m}\cdot\mathbf{n})^2}\,\mathrm{d}\mathbf{m}, \tag{3.11}$$

where $\mathbf{n} \in \mathbb{S}^2$ is an arbitrary unit vector, and η satisfies the relation

$$\eta = 0 \quad \text{or} \quad \frac{\int_0^1 \mathrm{e}^{\eta z^2}\,\mathrm{d}z}{\int_0^1 z^2(1-z^2)\,\mathrm{e}^{\eta z^2}\,\mathrm{d}z} = \alpha.$$

Substituting (3.11) into (3.8), we can derive that for minimizers, the energy can be written as

$$A_\varepsilon = \text{const.} + \varepsilon\frac{1}{2}G\alpha S_2^2|\nabla\mathbf{n}(\mathbf{x})|^2 + O(\varepsilon^2) \tag{3.12}$$

with

$$S_2 = \frac{\int_0^1 (3z^2-1)\,\mathrm{e}^{\eta z^2}\,\mathrm{d}z}{2\int_0^1 \mathrm{e}^{\eta z^2}\,\mathrm{d}z} \quad \text{and} \quad G = \frac{1}{3}\int g(\mathbf{y})|\mathbf{y}|^2\,\mathrm{d}\mathbf{y},$$

in which the leading non-trivial term is the one-constant form of the Oseen–Frank energy. One may also derive the general Oseen–Frank energy for more complicated (and realistic) interaction kernel $\mathcal{B}_\varepsilon(\mathbf{x};\mathbf{m},\mathbf{m}')$. We refer to E and Zhang (2006) for details. Liu and Wang (2018*b*) proved that the minimizers or critical points of the Onsager functional converge to minimizers or critical points of the one-constant Oseen–Frank energy. Taylor (2018) proved the Γ-convergence from the Onsager functional to a two-constant Oseen–Frank energy.

3.3. *Dynamics: analysis of various models*

The analysis of models for LC flow has been a hot topic in the analysis and PDE community during the past few decades, not only because these dynamical models provide typical and concrete examples of the hydrodynamical model for general complex fluids, but also because of the beautiful and complicated structures in these models and the corresponding deep challenges. As the results for the well-posedness and long-time behaviour of dynamical LC models are numerous, we only mention some of them here, and these are far from complete.

The long-time behaviour of the Smoluchowski equations without the hydrodynamics was studied by Vukadinovic (2009). For the full Doi–Onsager hydrodynamical model, the local well-posedness of strong solutions was established by Zhang and Zhang (2008). However, the global existence of weak solutions remains open. For recent work on the existence and properties of solutions to the dynamical **Q**-tensor models, we refer to papers by Paicu and Zarnescu (2012), Abels, Dolzmann and Liu (2014), Huang and Ding (2015), Wilkinson (2015), Liu and Wang (2018*a*) and the references therein.

The analysis of the Ericksen–Leslie model was initiated by Lin (1991), who presented a simplified Ericksen–Leslie system (without Leslie's stress). Moreover, Lin and Liu (1995, 1996) proposed a regularized model based on the Ginzburg–Landau approximation and proved the long-time asymptotic, existence and partial regularity. We refer to Section 5.1 for the explicit formulation of these simplified or regularized systems. There are many studies devoted to the existence of global weak solutions to the simplified or more general Ericksen–Leslie system in both $\mathbb{R}^2$ (Lin, Lin and Wang 2010, Hong 2011, Hong and Xin 2012, Huang, Lin and Wang 2014) and $\mathbb{R}^3$ (Lin and Wang 2016). The local well-posedness of strong solutions for the general Ericksen–Leslie system was proved by Wang, Zhang and Zhang (2013) for the whole space case and by Hieber, Nesensohn, Prüss and Schade (2016) on bounded domains with the Neumann boundary condition. Recently, the well-posedness for the Ericksen–Leslie system including the inertial term was considered (Jiang and Luo 2019, Cai and Wang 2020).

Another important issue in the analysis part is the generation or movement of singularities of solutions to the Ericksen–Leslie equation, which characterizes the dynamical behaviour of defects in LC flow. For the simplified equation, Huang, Lin, Liu and Wang (2016) constructed solutions in a 3D bounded domain with Dirichlet boundary data where the direction field blows up at finite time while the velocity field remains smooth. Lai *et al.* (2019) proves that for any given set of points in $\mathbb{R}^2$, one can construct solutions with smooth initial data which blow up exactly at these points in a short time.

The above list of analysis results for the Ericksen–Leslie system is far from complete. For more analysis results on the Ericksen–Leslie system or its variants, we refer to the survey papers by Lin and Wang (2014), Hieber and Prüss (2016) and the references therein.

3.4. Dynamics: from Doi–Onsager to Ericksen–Leslie

The formal derivation of the Ericksen–Leslie equation from Doi's kinetic theory was first studied by Kuzuu and Doi (1983). However, the Ericksen stress is omitted since only the homogeneous case is considered. This derivation was extended to the inhomogeneous case by E and Zhang (2006), who found that the Ericksen stress can be recovered from the body force which comes from the inhomogeneity of the chemical potential; see (2.11).

The derivations in Kuzuu and Doi (1983) and E and Zhang (2006) are based on the Hilbert expansion (also called the Chapman–Enskog expansion) of solutions with respect to the small parameter ε:

$$\begin{aligned} f(t,\mathbf{x},\mathbf{m}) &= f_0(t,\mathbf{x},\mathbf{m}) + \varepsilon f_1(t,\mathbf{x},\mathbf{m}) + \varepsilon^2 f_2(t,\mathbf{x},\mathbf{m}) + \cdots, \\ \mathbf{v}(t,\mathbf{x}) &= \mathbf{v}_0(t,\mathbf{x}) + \varepsilon \mathbf{v}_1(t,\mathbf{x}) + \varepsilon^2 \mathbf{v}_2(t,\mathbf{x}) + \cdots. \end{aligned} \tag{3.13}$$

Substituting the above expansion into the system (2.11) and collecting the terms with the same order of ε, we can obtain a series of equations for $(f_0, \mathbf{v}_0; f_1, \mathbf{v}_1; \cdots)$.

The $O(\varepsilon^{-1})$ equation gives that f_0 satisfies

$$\mathcal{R}\cdot(\mathcal{R}f_0 + f_0\mathcal{R}\mathcal{U}f_0) = 0,$$

which means f_0 is a critical point of $A_0[f]$. So by Theorem 2.1 we can let

$$f_0(t,\mathbf{m},\mathbf{x}) = h_{\eta,\mathbf{n}(t,\mathbf{x})}(\mathbf{m}) \quad \text{for some } \mathbf{n}(t,\mathbf{x}) \in \mathbb{S}^2.$$

For the terms of order $O(\varepsilon^0)$, it holds that

$$\frac{\partial f_0}{\partial t} + \mathbf{v}_0\cdot\nabla f_0 = \mathcal{G}_{f_0} f_1 + \mathcal{R}\cdot(f_0\mathcal{R}U_1 f_0) - \mathcal{R}\cdot(\mathbf{m}\times(\nabla\mathbf{v}_0)^\top\cdot\mathbf{m}f_0), \tag{3.14}$$

$$\begin{aligned}\frac{\partial \mathbf{v}_0}{\partial t} + \mathbf{v}_0\cdot\nabla\mathbf{v}_0 &= -\nabla p_0 + \frac{\gamma}{Re}\Delta\mathbf{v}_0 + \frac{1-\gamma}{2Re}\nabla\cdot(\mathbf{D}_0 : \langle\mathbf{mmmm}\rangle_{f_0}) \\ &\quad - \frac{1-\gamma}{Re}\left\{\nabla\cdot\left\langle\mathbf{mm}\times\left(\mathcal{R}f_1 + \sum_{i+j+k=1} f_iU_jf_k\right)\right\rangle_1 + \langle\nabla U_1 f_0\rangle_{f_0}\right\}.\end{aligned} \tag{3.15}$$

Although the above system involves the next order term f_1, which is unknown as yet, it is a closed evolution system for the direction field $\mathbf{n}(t,\mathbf{x})$ and the velocity $\mathbf{v}_0(t,\mathbf{x})$. Indeed, it is equivalent to the Ericksen–Leslie system for $(\mathbf{n}(t,\mathbf{x}), \mathbf{v}_0(t,\mathbf{x}))$ with coefficients determined by the parameters in the Doi–Onsager equation, which will be shown in Theorem 3.3 and 3.4 in the next subsections.

3.4.1. Analysis of the linearized operator

Analysis of the linearized operator

$$\mathcal{G}_h f \overset{\text{def}}{=} \mathcal{R}\cdot(\mathcal{R}f + h\mathcal{R}\mathcal{U}f + f\mathcal{R}\mathcal{U}h) \tag{3.16}$$

around a critical point h plays an important role in the reduction of the system (3.14)–(3.15). Kuzuu and Doi (1983) assumed or presented some properties of the null space and spectra. With the help of complete classifications of critical points of the Maier–Saupe energy, these properties can be rigorously proved (Wang *et al.* 2015*b*).

We introduce two operators $\mathcal{A}_h$ and $\mathcal{H}_h$, which are defined by

$$\mathcal{A}_h f \overset{\text{def}}{=} -\mathcal{R}\cdot(h\mathcal{R}f) + \mathcal{U}f, \quad \mathcal{H}_h f \overset{\text{def}}{=} \frac{f}{h} + \mathcal{U}f.$$

We have the following important relation:

$$\mathcal{G}_h f = -\mathcal{A}_h\mathcal{H}_h f. \tag{3.17}$$

Then the null spaces of $\mathcal{G}_h$, $\mathcal{H}_h$ and $\mathcal{G}_h^*$ (the conjugate of $\mathcal{G}_h$) can be characterized by the following theorem.

Proposition 3.2. Let $h_i = h_{\eta_i,\mathbf{n}}, i = 1, 2$. For $\alpha > \alpha^*$, the following hold.

(1) $\mathcal{G}_{h_1}$ and $\mathcal{G}_{h_2}$ with $\eta_2 = 0$ have no positive eigenvalues, whereas $\mathcal{G}_{h_2}$ has at least one positive eigenvalue for $\eta_2 \neq 0$.

(2) If $\phi \in \operatorname{Ker}\mathcal{G}_{h_1}$, then $\mathcal{H}_{h_1}\phi = 0$.

(3) $\operatorname{Ker}\mathcal{G}_{h_1} = \{\boldsymbol{\Theta}\cdot\mathcal{R}h_1; \boldsymbol{\Theta}\in\mathbb{R}^3\}$ is a 2D space.

(4) $\operatorname{Ker}\mathcal{G}_{h_1}^* = \{\mathcal{A}_{h_1}^{-1}(\boldsymbol{\Theta}\cdot\mathcal{R}h_1); \boldsymbol{\Theta}\in\mathbb{R}^3\}$.

3.4.2. Derivation of the angular momentum equation

From (3.14) we have

$$\left\langle \frac{\partial f_0}{\partial t} + \mathbf{v}_0 \cdot \nabla f_0 + \mathcal{R} \cdot (\mathbf{m} \times (\nabla \mathbf{v}_0)^\top \cdot \mathbf{m} f_0) - \mathcal{R} \cdot (f_0 \mathcal{R} U_1 f_0), \psi \right\rangle_{L^2(\mathbb{S}^2)} = 0 \quad (3.18)$$

for any $\psi \in \operatorname{Ker} \mathcal{G}^*_{f_0}$. This equation provides the evolution equation for the vector field $\mathbf{n}(t, \mathbf{x})$. In fact the following result tells us that $\mathbf{n}(t, \mathbf{x})$ satisfies the evolution equation in the Ericksen–Leslie equation with some constants λ_1, λ_2.

As $\operatorname{Ker} \mathcal{G}^*_{\mathbf{n}} = \mathcal{A}_{\mathbf{n}} \operatorname{Ker} \mathcal{G}_{\mathbf{n}}$, we have $\psi_0 \in \operatorname{Ker} \mathcal{G}^*_{\mathbf{n}}$ if and only if there is a vector $\mathbf{\Theta}$ such that

$$-\mathcal{R} \cdot (h_{\mathbf{n}} \mathcal{R} \psi_0) = \Theta \cdot \mathcal{R} h_{\mathbf{n}}. \quad (3.19)$$

Theorem 3.3. Equation (3.18) holds if and only if $\mathbf{n}(\mathbf{x}, t)$ is a solution of

$$\mathbf{n} \times (\gamma_1(\partial_t \mathbf{n} + \mathbf{v} \cdot \nabla \mathbf{n} + \mathbf{\Omega} \cdot \mathbf{n}) + \gamma_2 \mathbf{D} \cdot \mathbf{n} - k_F \Delta \mathbf{n}) = 0, \quad (3.20)$$

with $\mathbf{v} = \mathbf{v}_0$ and some γ_1, γ_2 depending on α and k_F depending on α and the interaction kernel function g.

Proof. Let $\mathbf{W}$ be a matrix with components given by $W_{ij} = \int_{\mathbb{S}^2} \mathcal{A}^{-1}(\mathcal{R}_i f_0) \mathcal{R}_j f_0$. Then we have the following.

- $\mathbf{W}$ is symmetric.
- $\mathbf{W} \cdot \mathbf{n} = 0$.
- For any unit vector $\mathbf{p}$ satisfying $\mathbf{p} \cdot \mathbf{n} = 0$, $\mathbf{p}^\top \cdot \mathbf{W} \cdot \mathbf{p}$ is independent of $\mathbf{p}$.

Therefore $\mathbf{W}$ is a constant multiple of $\mathbf{I} - \mathbf{nn}$, or $\mathbf{W} = \gamma_1(\mathbf{I} - \mathbf{nn})$, say, and we have

$$\int_{\mathbb{S}^2} \mathcal{A}^{-1}(\mathbf{v} \cdot \mathcal{R} f_0) \mathbf{w} \cdot \mathcal{R}_j f_0 = \gamma_1 \mathbf{v} \cdot (\mathbf{I} - \mathbf{nn}) \cdot \mathbf{w}. \quad (3.21)$$

Now assume that $\psi = \mathcal{A}^{-1}(\Theta \cdot \mathcal{R} f_0)$ with $\Theta \in \mathbb{R}^3$. First we have

$$\frac{\mathrm{d} f_0}{\mathrm{d} t} = \mathbf{m} \cdot \dot{\mathbf{n}} f_0' = (\dot{\mathbf{n}} \times \mathbf{n}) \cdot \mathcal{R} f_0.$$

Hence

$$\left\langle \frac{\mathrm{d} f_0}{\mathrm{d} t}, \psi \right\rangle = \langle (\dot{\mathbf{n}} \times \mathbf{n}) \cdot \mathcal{R} f_0, \mathcal{A}^{-1}(\Theta \cdot \mathcal{R} f_0) \rangle = -\gamma_1 \Theta \cdot (\mathbf{n} \times \dot{\mathbf{n}}). \quad (3.22)$$

Next we have

$$\begin{aligned} \langle \mathcal{R} \cdot (\mathbf{m} \times \kappa \cdot \mathbf{m} f_0), \psi \rangle &= \langle \mathcal{R} \cdot (\mathbf{m} \times (\mathbf{D} - \mathbf{\Omega}) \cdot \mathbf{m} f_0), \psi \rangle \\ &= -\left\langle \frac{1}{2} \mathcal{A}(\mathbf{mm} \colon \mathbf{D}) + (\mathbf{n} \times (\mathbf{\Omega} \cdot \mathbf{n})) \cdot \mathcal{R} f_0, \mathcal{A}^{-1} \Theta \cdot \mathcal{R} f_0 \right\rangle \\ &= \langle \mathbf{m} \times (\mathbf{D} \cdot \mathbf{m}), \Theta f_0 \rangle - \langle (\mathbf{n} \times (\mathbf{\Omega} \cdot \mathbf{n})) \cdot \mathcal{R} f_0, \mathcal{A}^{-1} \Theta \cdot \mathcal{R} f_0 \rangle \\ &= (S_2 \mathbf{n} \times (\mathbf{D} \cdot \mathbf{n}) - \gamma_1 \mathbf{n} \times (\mathbf{\Omega} \cdot \mathbf{n})) \cdot \Theta. \quad (3.23) \end{aligned}$$

From (3.7) we have

$$\begin{aligned}-\langle \mathcal{R}\cdot(f_0\mathcal{R}U_1 f_0),\psi\rangle &= \langle U_1 f_0, \Theta\cdot\mathcal{R}f_0\rangle\\ &= \int_{\mathbb{S}^2}\alpha S_2 G\mathbf{m}\times(\Delta(\mathbf{nn})\cdot\mathbf{m})\cdot\Theta f_0\,\mathrm{d}\mathbf{m}\\ &= S_2^2\alpha G\Theta\cdot(\mathbf{n}\times\Delta\mathbf{n}).\end{aligned}$$

Let $\mathbf{h} = S_2^2\alpha G\Delta\mathbf{n}$. Then

$$-\langle \mathcal{R}\cdot(f_0\mathcal{R}U_1 f_0),\psi\rangle = \Theta\cdot(\mathbf{n}\times\mathbf{h}). \tag{3.24}$$

Let $\gamma_2 = -S_2$. Then, combining (3.22), (3.23) and (3.24), we obtain that for any $\Theta\in\mathbb{R}^3$,

$$\Theta\cdot(\mathbf{n}\times(\gamma_1(\partial_t\mathbf{n}+\mathbf{v}_0\cdot\nabla\mathbf{n}+\mathbf{\Omega}\cdot\mathbf{n})+\gamma_2\mathbf{D}\cdot\mathbf{n}-\mathbf{h})) = 0,$$

which completes our proof. Note that the induced Oseen–Frank energy is

$$E_{OF} = \frac{k_F}{2}|\nabla\mathbf{n}|^2, \quad \text{with } k_F = S_2^2\alpha G. \tag{3.25}$$

which agrees with the $O(\varepsilon)$ part of (3.12). □

3.4.3. *Derivation of the momentum equation*

Now we calculate the stress tensor in (3.15):

$$\begin{aligned}\tau_1 &= \int_{\mathbb{S}^2}\mathbf{mm}\times\Bigg(\mathcal{R}f_1+\sum_{i+j+k=1} f_i\mathcal{R}U_j[f_k]\Bigg)\,\mathrm{d}\mathbf{m},\\ \tau_2 &= \int_{\mathbb{S}^2} f_0\nabla U_1[f_0]\,\mathrm{d}\mathbf{m},\\ \tau_3 &= \int_{\mathbb{S}^2} f_0\mathbf{mm}(\mathbf{mm}:\mathbf{D})\,\mathrm{d}\mathbf{m}.\end{aligned}$$

From (3.7) we have

$$\begin{aligned}\tau_2 &= \int_{\mathbb{S}^2} -\frac{\alpha S_2}{2}Gf_0(\mathbf{m}\cdot\mathbf{n})\nabla(\mathbf{mm}:\Delta(\mathbf{nn}))\,\mathrm{d}\mathbf{m}\\ &= \int_{\mathbb{S}^2}\frac{\alpha S_2}{2}G\nabla f_0(\mathbf{m}\cdot\mathbf{n})\mathbf{mm}:\Delta(\mathbf{nn})\,\mathrm{d}\mathbf{m} + \text{gradient term}\\ &= \frac{\alpha S_2^2}{2}G\nabla(\mathbf{nn}):\Delta(\mathbf{nn}) + \text{gradient term}\\ &= -\alpha S_2^2 G\nabla\mathbf{n}_k\Delta\mathbf{n}_k + \text{gradient term}\\ &= -\alpha S_2^2 G\nabla\cdot(\nabla\mathbf{n}\odot\nabla\mathbf{n}) + \text{gradient term},\end{aligned}$$

which is actually the Ericksen tensor σ^E up to a pressure term with the Oseen–Frank energy given by (3.25).

For the stress of τ_1, we can write

$$\tau_1 = \langle \mathbf{mm} \times \mathcal{R}(\mathcal{H} f_1 + U_1[f_0])\rangle_{f_0}.$$

It can be decomposed into two parts, τ_1^S and τ_1^A, which are symmetric and antisymmetric respectively. By the identity (A.5), the symmetric part satisfies

$$\begin{aligned}\tau_1^S &= \frac{1}{2}\int_{\mathbb{S}^2}\left(\mathbf{mm} - \frac{1}{3}\mathbf{I}\right)\left\{\frac{\partial f_0}{\partial t} + \mathbf{v}_0 \cdot \nabla f_0 + \mathcal{R}\cdot(\mathbf{m} \times (\nabla \mathbf{v}_0)^\top \cdot \mathbf{m} f_0)\right\} \mathrm{d}\mathbf{m}\\ &= \frac{1}{2}((\partial_t + \mathbf{v}_0 \cdot \nabla)\langle \mathbf{mm}\rangle_{f_0} + 2\mathbf{D} : \langle \mathbf{mmmm}\rangle_{f_0}\\ &\quad - (\mathbf{D} - \mathbf{\Omega}) \cdot \langle \mathbf{mm}\rangle_{f_0} - \langle \mathbf{mm}\rangle_{f_0} \cdot (\mathbf{D} + \mathbf{\Omega})),\end{aligned}$$

where we used equation (A.7) in the last equality.

For any antisymmetric matrix $\mathbf{A}$ we have

$$\begin{aligned}&\langle \mathbf{mm} \times f_0 \mathcal{R}(\mathcal{H} f_1 + U_1[f_0])\rangle_{f_0} : \mathbf{A}\\ &\quad = \langle [\mathbf{m} \times (\mathbf{A} \cdot \mathbf{m})] \cdot \mathcal{R}(\mathcal{H} f_1 + U_1[f_0])\rangle_{f_0}\\ &\quad = -\langle [\mathbf{m} \times (\mathbf{A} \cdot \mathbf{m})] \cdot \mathcal{R}(\mathcal{H} f_1 + U_1[f_0])\rangle_{f_0}\\ &\quad = -\langle [\mathbf{n} \times (\mathbf{A} \cdot \mathbf{n})] \cdot \mathcal{R}(\mathcal{H} f_1 + U_1[f_0])\rangle_{f_0}\\ &\quad = -\langle [\mathbf{n} \times (\mathbf{A} \cdot \mathbf{n})] \cdot \mathcal{R} U_1[f_0]\rangle_{f_0}\\ &\quad = -[\mathbf{n} \times (\mathbf{A} \cdot \mathbf{n})] \cdot (\mathbf{n} \times \mathbf{h})\\ &\quad = \frac{1}{2}(\mathbf{nh} - \mathbf{hn}) : \mathbf{A},\end{aligned}$$

which implies

$$\tau_1^A = \frac{1}{2}(\mathbf{nh} - \mathbf{hn}).$$

From (A.4) we have

$$\begin{aligned}\tau_3 &= \int_{\mathbb{S}^2} f_0 \mathbf{mm}(\mathbf{mm} : \mathbf{D})\, \mathrm{d}\mathbf{m}\\ &= S_4 \mathbf{nn}(\mathbf{D} : \mathbf{nn}) + \frac{2(S_2 - S_4)}{7}(\mathbf{nD} \cdot \mathbf{n} + \mathbf{D} \cdot \mathbf{nn}) + 2\left(\frac{S_4}{35} - \frac{2S_2}{21} + \frac{1}{15}\right)\mathbf{D}.\end{aligned}$$

Combining the above equations and noting that

$$\mathbf{h} = \gamma_1 \mathbf{N} + \gamma_2 \mathbf{D} \cdot \mathbf{n},$$

we can obtain the following theorem.

Theorem 3.4. Equation (3.15) is equivalent to

$$\partial_t \mathbf{v}_0 + \mathbf{v}_0 \cdot \nabla \mathbf{v}_0 = -\nabla p + \nabla \cdot (\sigma^E + \sigma^L), \tag{3.26}$$

where the stress terms are defined by

$$\begin{aligned}\sigma^E &= -k_F \nabla \cdot (\nabla \mathbf{n} \odot \nabla \mathbf{n}),\\ \sigma^L &= \frac{\gamma}{Re}\mathbf{D} + \frac{1-\gamma}{Re}(\alpha_1(\mathbf{nn}\colon \mathbf{D})\mathbf{nn} + \alpha_2 \mathbf{nN} + \alpha_3 \mathbf{Nn}\\ &\quad + \alpha_4 \mathbf{D} + \alpha_5 \mathbf{nn}\cdot\mathbf{D} + \alpha_6 \mathbf{D}\cdot\mathbf{nn}),\end{aligned}$$

with coefficients $\alpha_i (i = 1, 2, \ldots, 6)$ given by

$$\begin{aligned} &\alpha_1 = -\frac{S_4}{2}, && \alpha_2 = -\frac{1}{2}(S_2 - \gamma_1), && \alpha_3 = -\frac{1}{2}(S_2 + \gamma_1),\\ &\alpha_4 = \frac{4}{15} - \frac{5}{21}S_2 - \frac{1}{35}S_4, && \alpha_5 = \frac{1}{7}S_4 + \frac{6}{7}S_2, && \alpha_6 = \frac{1}{7}S_4 - \frac{1}{7}S_2. \end{aligned} \tag{3.27}$$

3.4.4. *Higher-order terms and the control of the remainder terms*

We can also perform the higher-order expansion in a similar way up to any order of ε. Then we arrive at a series of equations for $(f_i(t, \mathbf{x}, \mathbf{m}), \mathbf{v}_i(t, \mathbf{x}))$ $(i = 0, 1, 2, \ldots)$. In principle, these high-order terms provide more accurate corrections for approximate solutions. However, it is not known so far whether the expansion in the right-hand side of (3.13) is convergent. Moreover, even the existence of corrector solutions $(f_i(t, \mathbf{x}, \mathbf{m}), \mathbf{v}_i(t, \mathbf{x}))$ is not clear, although the equations can be derived explicitly.

Rigorous confirmation of the validity of expansion (3.13) requires the following:

- existence of smooth solutions to $(f_i(t, \mathbf{x}, \mathbf{m}), \mathbf{v}_i(t, \mathbf{x}))$ for all $i \geq 0$,
- bounding the difference between the true solution $(f_\varepsilon, \mathbf{v}_\varepsilon)$ and the approximate solutions

$$\begin{aligned} f^{(k)}(t, \mathbf{x}, \mathbf{m}) &= \sum_{i=1}^{k} \varepsilon^i f_i(t, \mathbf{x}, \mathbf{m}),\\ \mathbf{v}^{(k)}(t, \mathbf{x}) &= \sum_{i=1}^{k} \varepsilon^i \mathbf{v}_i(t, \mathbf{x}). \end{aligned} \tag{3.28}$$

  Indeed, we need the bound to tend to 0 as $\varepsilon \to 0$.

The proof of the first part relies on the local existence of smooth solutions to the Ericksen–Leslie equations, which is proved in Wang *et al.* (2013). Indeed, let $(\mathbf{n}(t, \mathbf{x}), \mathbf{v}_0(t, \mathbf{x}))$ be a solution on time interval $[0, T]$ satisfying the Ericksen–Leslie system with parameters suitably given; then we can construct a corresponding solution $(f_0(t, \mathbf{x}, \mathbf{m}), \mathbf{v}_0(t, \mathbf{x})) = (h(\mathbf{m}\cdot\mathbf{n}(t, \mathbf{x})), \mathbf{v}(t, \mathbf{x}))$ to (3.14)–(3.15). The construction of $(f_1(t, \mathbf{x}, \mathbf{m}), \mathbf{v}_1(t, \mathbf{x}))$ is rather subtle, since the system is nonlinear and this implies that the existing time may be smaller than T in general. However, by carefully examining the inherent structure of the system, one may find that $(f_1(t, \mathbf{x}, \mathbf{m}), \mathbf{v}_1(t, \mathbf{x}))$ could be constructed by solving a linear system, and thus the existing time can be extended to $[0, T]$. The system for $(f_k(t, \mathbf{x}, \mathbf{m}), \mathbf{v}_k(t, \mathbf{x}))$ $(k \geq 2)$ is straightforwardly linear and can be solved directly.

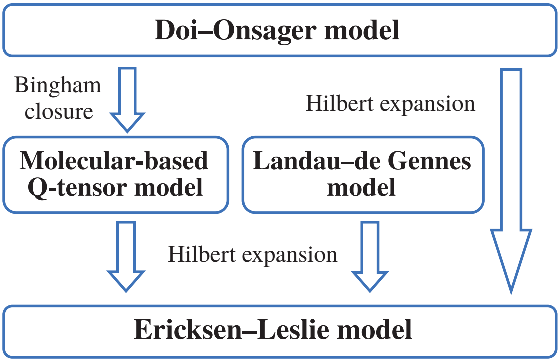

Figure 3.1. Reduction to the Ericksen–Leslie theory from the Doi–Onsager theory or the dynamic **Q**-tensor theory.

The second part, *i.e.* estimates for the difference, is much more difficult. The key ingredients are the spectral analysis for the linearized operator $\mathcal{G}_h$ and a lower bound estimate for a bilinear functional related to a modified non-local version of $\mathcal{G}_h$. We refer to Wang *et al.* (2015*b*) for details.

3.5. *Dynamics: other relations*

The connection between the dynamic **Q**-tensor model and the Ericksen–Leslie model can be directly derived. One may refer to Beris and Edwards (1994) or Qian and Sheng (1998) for the derivation from the Beris–Edward model or Qian–Sheng model to the Ericksen–Leslie theory respectively. The correspondence of parameters can also be found. For rigorous justifications, one may apply the similar procedure discussed in Section 3.4. We refer to Wang, Zhang and Zhang (2015*a*) and Li *et al.* (2015) for the uniaxial limit of the dynamic **Q**-tensor models such as the Beris–Edwards model, the molecular-based dynamic **Q**-tensor model and the inertial Qian–Sheng model, respectively. These results are summarized in Figure 3.1.

The above discussions build a solid correspondence between the Ericksen–Leslie theory and the Doi–Onsager theory or the dynamic **Q**-tensor theory. However, they are based on the framework of smooth solutions, which relies on the existence of a smooth solution of the Ericksen–Leslie system. Thus it excludes the possibility of defects. To resolve this problem, one needs to study the relations between weak solutions. Liu and Wang (2018*c*) tackled this issue, and proved that the solutions to the Doi–Onsager equation without hydrodynamics converge to the weak solution of the harmonic map heat flow – the gradient flow of the one-constant Oseen–Frank energy.

4. Numerical methods for computing stable defects of liquid crystals

In this section we review recent developments in numerical methods for computing stable defect patterns of LCs. We will focus on NLC systems again and apply the LdG theory as the model system to provide a sample of relatively new progress on the development of numerical algorithms that are applicable to general LC problems. Two numerical approaches will be reviewed in order to obtain a local minimum for a given energy functional. One is the energy-minimization-based approach, which follows the idea of ‘discretize-then-minimize’, and the other is to solve the gradient flow dynamics.

4.1. Energy-minimization-based approach

The energy-minimization-based approach first discretizes the free energy by introducing a suitable spatial discretization to the order parameter of system, and then adopts some optimization methods to compute local minimizers of the discrete free energy. From an optimization point of view, solving the gradient flow equation corresponds to the gradient descent method on the discrete free energy. An energy-minimization-based approach enables us to apply some advanced optimization methods, such as Newton-type methods or quasi-Newton methods, which may be able to find local minimizers of the discrete free energy more efficiently.

The idea of computing defect structures in LCs by an energy-minimization-based approach can be traced back to some early work on the Oseen–Frank model in the late 1980s. Cohen *et al.* (1987) obtained several LC configurations by numerically minimizing the Oseen–Frank energy. However, due to the lack of convexity of the unit-length constraint, the convergence of their algorithms is difficult to establish. A significant improvement was made by Alouges (1997), who proposed an energy-decreasing algorithm for the one-constant Oseen–Frank model. The convergence of this algorithm is proved in a continuous setting. Later, Adler *et al.* (2015) proposed an energy-minimization finite-element approach to the Oseen–Frank model by using Lagrangian multipliers and the penalty method, which can be applied to the cases with elastic anisotropy and electric/flexoelectric effects (Adler *et al.* 2015, Adler, Emerson, MacLachlan and Manteuffel 2016). A surface finite element method was developed for the surface Oseen–Frank problem to study the orientational ordering of NLCs on curved surfaces (Nitschke *et al.* 2018, Nestler, Nitschke, Praetorius and Voigt 2018). For the Ericksen model, Nochetto *et al.* (2017) proposed a structure-preserving discretization of the LC energy with piecewise linear finite elements, and developed a quasi-gradient flow scheme for computing discrete equilibrium solutions that have the property of strictly monotone decreasing energy. They also proved Γ-convergence of discrete global minimizers to continuous ones as the mesh size goes to zero. A similar idea has been applied to the generalized Ericksen model with eight independent ‘elastic’ constants (Walker 2020) and a uniaxially constrained $\mathbf{Q}$-tensor model (Borthagaray, Nochetto and Walker 2020).

For the full **Q**-tensor model, Gartland Jr *et al.* (1991) constructed a numerical procedure that minimizes the LdG free-energy model, which is based on a finite-element discretization to the tensor order parameter, and a direct minimization scheme based on Newton's method and successive over-relaxation. The corresponding analytical and numerical issues of this numerical procedure were addressed by Davis and Gartland Jr (1998), who proved the well-posedness of the discrete problem. As well as being more physically realistic, the full **Q**-tensor model has the advantage that the corresponding optimization problem is almost unconstrained (as the eigenvalue constraint is normally satisfied due to the boundary condition in a certain parameter region), although it might require higher computational cost since **Q** has five degrees of freedom.

In recent years we have incorporated the spectral method with energy-minimization techniques and successfully applied our approach to different confined LC systems, including three-dimensional spherical droplets (Hu, Qu and Zhang 2016), three-dimensional cylinders (Hu *et al.* 2016, Han, Hu, Zhang and Zhang 2019), nematic shells (Qu, Wei and Zhang 2017), nematic wells (Yin *et al.* 2020*a*) and LC colloids (Wang *et al.* 2017, Tong, Wang and Zhang 2017, Wang, Zhang and Chen 2018). From a computational perspective, as an efficient numerical method with high accuracy, the spectral method makes an accurate free-energy calculation for 3D problems possible and enables us to determine the phase diagram of some complicated LC systems (Wang *et al.* 2017).

To apply the spectral method to different confined LC systems, one can either identify an appropriate coordinate system, *i.e.* map the physical domain to a regular computational domain (Hu *et al.* 2016, Wang *et al.* 2017), or use a phase-field-type method (Wang *et al.* 2018) to deal with the underlying geometry and the boundary conditions. Then the free energy can be discretized by introducing a spectral discretization to the order parameter **Q**. Since the order parameter **Q** is a traceless symmetric tensor, it can be written as

$$\mathbf{Q} = \begin{bmatrix} q_1 & q_2 & q_3 \\ q_2 & q_4 & q_5 \\ q_3 & q_5 & -q_1 - q_4 \end{bmatrix}. \tag{4.1}$$

We can introduce a spectral approximation to q_i separately. The local minimizers of the resulting discrete free energy $\mathcal{F}_h(\Xi)$ can be computed by some optimization methods, such as the Broyden–Fletcher–Goldfarb–Shanno (BFGS) method. Here $\Xi \in \mathbb{R}^{5\times K}$ consists of all expansion coefficients and K is the number of basis functions.

The key step in the above numerical procedure is to compute the gradient of the discrete free energy $\mathcal{F}_h(\Xi)$ with respect to Ξ. To illustrate the idea, we consider a simple system with a scalar order parameter φ and a free energy

$$\mathcal{F}[\varphi] = \int W(\varphi, \nabla\varphi)\,\mathrm{d}\mathbf{x}. \tag{4.2}$$

We can discretize the free energy $\mathcal{F}(\varphi)$ by introducing a spectral approximation to

$$\varphi = \sum_{i=1}^{K} \xi_i \phi_i, \tag{4.3}$$

where ϕ_i are the basis functions and ξ_i are the expansion coefficients that must be determined during the optimization procedure. The derivative of $\mathcal{F}_h(\Xi)$ with respect to ξ_i can be computed directly as

$$\frac{\partial}{\partial \xi_i}\mathcal{F}_h(\Xi) = \int \frac{\partial W}{\partial \varphi}\phi_i + \frac{\partial W}{\partial \nabla\varphi} \cdot \nabla\phi_i \,\mathrm{d}\mathbf{x}, \tag{4.4}$$

which is easy to compute via numerical integration. Note that the weak form of the Euler–Lagrange equation of the free energy (4.2) is given by

$$\left(\frac{\partial W}{\partial \varphi}, \psi\right) + \left(\frac{\partial W}{\partial \nabla\varphi}, \nabla\psi\right) = 0, \tag{4.5}$$

where ψ is a test function and $(.,.)$ is the standard L^2-inner production. Hence the stationary points of the discrete free energy $\mathcal{F}_h(\Xi)$ are exactly the numerical solutions of the Euler–Lagrange equation $(\delta\mathcal{F})/(\delta\varphi) = 0$ obtained by a Galerkin method. The idea of discretization first can be extended to dynamics cases with variational structure; we refer the interested reader to Doi, Zhou, Di and Xu (2019) and Liu and Wang (2020*a*) for some recent developments. In particular, by using the strategy of 'discretize-then-variation', Liu and Wang (2020*b*) proposed a variational Lagrangian scheme for a phase field model, which has an advantage in capturing the thin diffuse interface with a small number of mesh points. Such a numerical methodology can certainly be applied to a liquid crystal system and will have potential advantages in computing the defect structures.

Next we discuss the choice of basis function. For three-dimensional unit spheres, Hu *et al.* (2016) choose the basis functions to be Zernike polynomials Z_{nlm} (Zernike 1934, Mahajan and Dai 2007), defined by

$$Z_{nlm}(r,\theta,\phi) = R_n^{(l)}(r) Y_{lm}(\theta,\phi), \tag{4.6}$$

where

$$R_n^{(l)} = \begin{cases} \displaystyle\sum_{s=0}^{(n-l)/2} N_{nls} r^{n-2s} & 0 \le \dfrac{n-l}{2} \in \mathbb{Z}, \\ 0 & \text{otherwise,} \end{cases}$$

$$N_{nls} = (-1)^s \sqrt{2n+3} \prod_{i=1}^{n-l} (n+l-2s+1+i) \prod_{i=1}^{l} \left(\frac{n-l}{2} - s + i\right) \frac{2^{l-n}}{s!(n-s)!},$$

$Y_{lm}(\theta,\phi) = P_l^{|m|}(\cos\theta)X_m(\phi)$ are the spherical harmonic functions with

$$X_m(\phi) = \begin{cases} \frac{1}{\pi}\cos m\phi & m \geq 0, \\ \frac{1}{\pi}\sin|m|\phi & m < 0, \end{cases}$$

and $P_l^m(x)$ ($m \geq 0$) are the normalized associated Legendre polynomials. The Zernike polynomials Z_{nlm} are orthogonal in the three-dimensional unit sphere, which can simplify the computation in (4.5). Similarly, for the 2D disk and cylindrical domain (Hu *et al.* 2016, Han *et al.* 2019), the authors choose 2D Zernike polynomials Z_{nl} as the basis functions.

The orthogonality of the basis functions is not required in the above numerical procedure. A disadvantage of using Zernike polynomials is that the value of $R_n^{(l)}(r)$ for given r is not easy to compute with high accuracy. Standard basis functions, such as Legendre and Chebyshev polynomials, might be better choices in numerical calculation for more general problems. For example, for spherical shells and unbounded domains outside one or two spheres (Wang *et al.* 2017, Tong *et al.* 2017, Noh *et al.* 2020), we can first map the physical domain to a computational domain,

$$\Omega = \{(\zeta,\mu,\varphi) \mid -1 \leq \zeta \leq 1, 0 \leq \mu < \pi, 0 \leq \varphi < 2\pi\},$$

and choose real spherical harmonics of (μ,φ) and Legendre polynomials of ζ as the basis functions.

To validate the algorithm, Hu *et al.* (2016) compared the numerical results of the radial hedgehog solution with its analytic form (Gartland Jr and Mkaddem 1999, Majumdar 2012). The radial hedgehog solution is a radial symmetric solution, in which the **Q** is given by

$$\mathbf{Q}_{RH}(\mathbf{r}) = h(|\mathbf{r}|)\left(\frac{\mathbf{r}}{|\mathbf{r}|}\otimes\frac{\mathbf{r}}{|\mathbf{r}|} - \frac{1}{3}\mathbf{I}\right), \quad 0 < |\mathbf{r}| \leq 1,$$

where $h(r)$ satisfies the second-order ODE (3.3), which can be solved accurately. By increasing the number of the basis in the Zernike polynomials using $N = 4k$, $L = 16$, $M = 4$, the numerical error in the total free energy decreases to as low as 10^{-10} (Hu *et al.* 2016). For more complicated solutions (without radial symmetry), Wang *et al.* (2017) exhibited the numerical error in free-energy calculations for the dipole and Saturn ring defect around a spherical particle immersed in an NLC. These numerical tests suggest that such numerical methods are adequate for an accurate free-energy calculation to determine the phase diagram of the system.

Finding minimizers of the LdG free energy is an unconstrained nonlinear optimization problem. The minimizers can be obtained by optimization methods such as the gradient descent method and quasi-Newton methods. A commonly used optimization method for such problems is the limit-memory Broyden–Fletcher–Goldfarb–Shanno (L-BFGS) method (Knyazev 2001). The energy-minimization-based numerical approach with L-BFGS usually converges to a local minimizer with a proper initial guess, but that is not necessarily guaranteed. To check whether the solution is a local minimizer, we need to justify the stability of the solution on the energy landscape F by computing the smallest eigenvalue λ_1 of its Hessian $\mathbb{H}(\mathbf{x}) = \nabla^2 F(\mathbf{x})$, the associated second variation of the reduced energy corresponding to $\mathbf{x}$ (Yin *et al.* 2019, Canevari, Harris, Majumdar and Wang 2020):

$$\lambda_1 = \min_{\mathbf{v}\in\mathbb{R}^n} \frac{\langle \mathbb{H}(\mathbf{x})\mathbf{v}, \mathbf{v}\rangle}{\langle \mathbf{v}, \mathbf{v}\rangle}, \tag{4.7}$$

where $\langle\cdot,\cdot\rangle$ is the standard inner product in $\mathbb{R}^n$. The solution is locally stable or metastable if $\lambda_1 > 0$. In practice, λ_1 can be computed by solving the gradient flow equation of $\mathbf{v}$:

$$\frac{\partial \mathbf{v}}{\partial t} = -\frac{2\gamma}{\langle \mathbf{v}, \mathbf{v}\rangle}\left(\mathbb{H}\mathbf{v} - \frac{\langle \mathbb{H}\mathbf{v}, \mathbf{v}\rangle}{\langle \mathbf{v}, \mathbf{v}\rangle}\right), \tag{4.8}$$

where γ is a relaxation parameter and $\mathbb{H}(\mathbf{x})\mathbf{v}$ can be approximated by

$$\mathbb{H}(\mathbf{x})\mathbf{v} \approx -\frac{\nabla F(\mathbf{x} + l\mathbf{v}) - \nabla F(\mathbf{x} - l\mathbf{v})}{2l} \tag{4.9}$$

for some small constant l. We can choose $\gamma(t)$ to accelerate the convergence of the dynamic system (4.8) (Yin *et al.* 2019).

The first example of minimizing the LdG free energy is to calculate the possible equilibria of NLCs confined in a three-dimensional ball with different kinds of anchoring conditions (Hu *et al.* 2016). For the strong radial anchoring condition, three different configurations are obtained: the radial hedgehog, ring disclination and split core solutions (Figure 4.1(a–c)). In the radial hedgehog solution $\mathbf{Q}$ is uniaxial everywhere with a central point defect, which is a rare example of a pure uniaxial solution for the Landau–de Gennes model (Lamy 2015, Majumdar and Wang 2018). For low temperature and large domain size, the point defect broadens into a disclination ring. The disclination ring solution is a symmetry-breaking configuration. The split core solution contains a +1 disclination line in the centre with two isotropic points at both ends, the existence of which is proved in Yu (2020) under the rotational symmetric assumption. The authors also consider the relaxed radial anchoring condition, which allows $s = s(\mathbf{x})$ to be a free scalar function on $\partial\Omega$. Besides the radial hedgehog, disclination ring and split core configurations, one more solution is obtained for this boundary condition, as shown in Figure 4.1(d). Two rings of isotropic points form on the sphere. Between the two rings, on the surface $\mathbf{Q}$ is uniaxial and oblate ($s < 0$). Inside the ball, there is a strong biaxial region close to the surface. For a planar boundary condition, the authors find three stable solutions (Figure 4.1(e–f)). In Figure 4.1(e), two +1 point defects form at two poles. As the temperature decreases, the point defect on the surface splits into two +1/2 point defects. In Figure 4.1(f), the four +1/2 point defects on the sphere form the vertices of a tetrahedron. Inside the ball, there are disclination lines which intersect with the spherical surface on the above-mentioned point defects. The

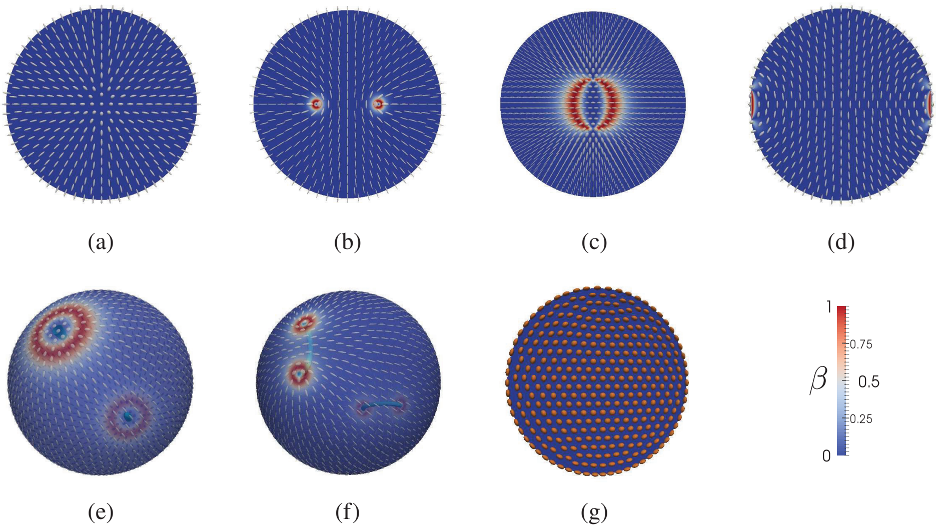
(a) (b) (c) (d)

(e) (f) (g)

Figure 4.1. (Credit: Hu *et al.* 2016.) Possible equilibria under various anchoring conditions. (a–c) Three equilibria under the strong radial anchoring condition on the x–z plane: radial hedgehog (a), ring disclination (b) and split core (close-up view) (c). (d) Equilibrium under the relaxed radial anchoring condition. (e–f) Two equilibria for the planar anchoring condition. (g) A uniaxial solution for the planar anchoring condition. Here $\beta = 0$ and $\mathbf{Q}$ is oblate everywhere. The colour bar indicates $\beta = 1 - 6((\operatorname{tr}\mathbf{Q}^3)^2/(\operatorname{tr}\mathbf{Q}^2)^3)$, with red for biaxial and blue for uniaxial. The values of β (represented by colour) and the $\mathbf{Q}$-tensor (represented by ellipsoid glyphs) arise from numerical simulation. The cyan tubes inside the ball in (e–f) are the isosurfaces of $c_l = \lambda_1 - \lambda_2$, the difference between two largest eigenvalues of $\mathbf{Q}$.

configuration in Figure 4.1(e) has two segments of +1 disclination lines with one isotropic end buried inside the ball and the other end connecting the surface. As the temperature decreases, the +1 disclination splits into a +1/2 disclination with both ends open at the surface. Another metastable solution is shown in Figure 4.1(g). In this configuration $\mathbf{Q}$ is uniaxial everywhere and has radial symmetry. But unlike the radial hedgehog solution, $\mathbf{Q}$ is oblate ($s < 0$) everywhere rather than prolate.

For the 2D disk and 3D cylinder, Hu *et al.* (2016) obtained minimizers on the unit disk with boundary condition $\mathbf{Q}(\cos\phi, \sin\phi) = s_+(\mathbf{n}\otimes\mathbf{n} - \mathbf{I}/3)$, where

$$\mathbf{n} = \left(\cos\frac{k}{2}\phi, \sin\frac{k}{2}\phi, 0\right), \quad k = \pm 1, \pm 2, \ldots,$$

is kept in the x–y plane at the boundary. They found that the solutions are predictable. For large temperature and large domain, there is a semi-radial solution in

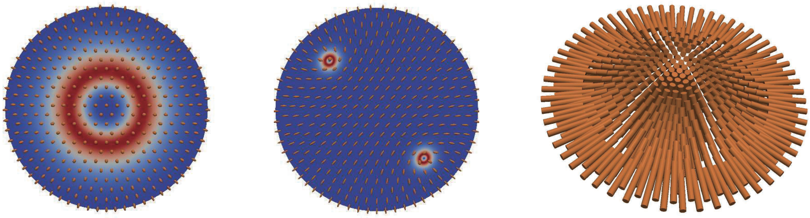

(a) planar radial (PR) (b) planar polar (PP) (c) escape radial (ER)

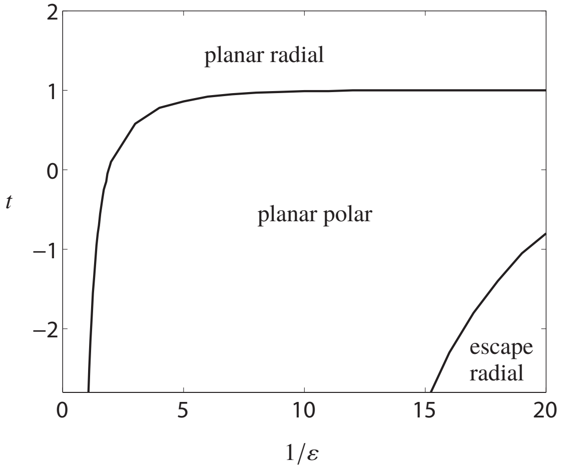

(d) phase diagram

Figure 4.2. (Credit: Hu *et al.* 2016.) Three equilibria: (a) planar radial, (b) planar polar and (c) escape radial for the radial anchoring condition on a 2D disk. β is shown in colour in (a–b) with red indicating biaxial and blue uniaxial. Ellipsoids represent the **Q**-tensor. Golden solid bars in (c) represent the eigendirection corresponding to the largest eigenvalue. (d) Phase diagram of the planar radial, planar polar and escape radial configurations. The partition is based on the lowest energy of the three.

which all the eigenvalues are rotational symmetric and the eigenvectors are invariant along the r-direction determined by the boundary condition. The semi-radial solution has a central defect with winding number determined by the boundary constraint. As the temperature decreases and the domain size increases, the semi-radial solution becomes unstable and the central defect quantizes to defect points with $+1/2$ or $-1/2$ winding number. The number of $1/2$ defects is determined by the conservation of the total winding number. When k of the boundary condition is even, there is a non-singular harmonic map solution, a phenomenon that Sonnet, Kilian and Hess (1995) referred to as ‘escape into the third dimension’. Both the escape solution and the quantized $\pm 1/2$ solutions are stable for low temperature.

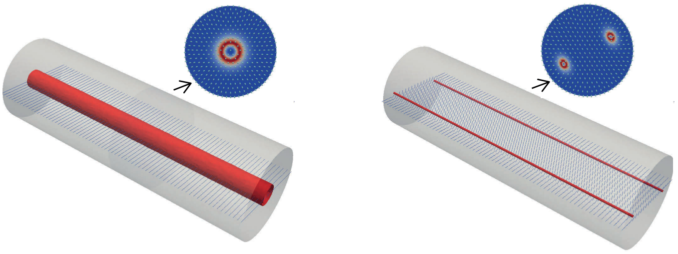

(a) planar radial (PR) (b) planar polar (PP)

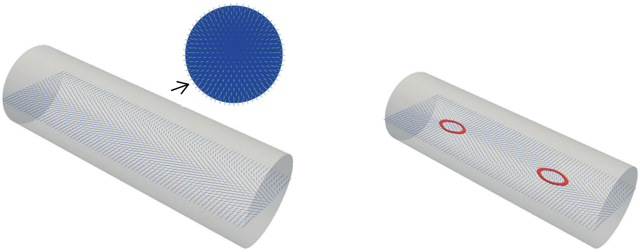

(c) escape radial (ER) (d) escape radial with ring defect (ERRD)

Figure 4.3. (Credit: Han *et al.* 2019.) Four equilibria of NLCs confined in a cylinder with the homeotropic anchoring condition: (a) planar radial, (b) planar polar, (c) escape radial and (d) escape radial with ring defect. Disclination lines are represented by the red isosurface of c_l. The disk in the upper-right corner is the transversal view of the structure in (a–c). The ellipsoid on the disk represents the $\mathbf{Q}$-tensor on the disk and the colour corresponds to β, ranging from 0 (blue) to 1 (red).

As the temperature decreases further, the free energy of the escape solution will be lower. When $k = 2$ or with planar boundary conditions, there are three known configurations: planar radial (PR), planar polar (PP) and escape radial (ER), as shown in Figure 4.2. The planar radial has one $+1$ point defect at the centre; the planar polar solution has two $+1/2$ point defects that form on opposite locations on the disk; the escape radial has no defect in which $\mathbf{Q}$ is uniaxial everywhere with s being constant and $\mathbf{n}$ being a harmonic map for the given boundary condition. A phase diagram for these three configurations is shown in Figure 4.2(d).

With z-axial invariance, the PR, PP and ER configurations (Figure 4.3(a–c)) are still stable equilibria of NLCs confined in a cylinder with homeotropic boundary conditions. Without axial invariance, the escape radial with ring defect (ERRD) configuration (Figure 4.3(d)) is also a stable equilibrium, which has two disclination rings lying on a plane parallel to the axial direction of the cylinder. Two disclination rings can be considered as the broadening of two point defects with topological charge $+1$ and -1 (Brada, Kralj, Svetec and Zumer 2003). The ERRD solution can be considered as a quenched metastable state formed by joining ER configurations with opposite pointing directions, which means the free energy of ERRD is always higher than ER.

For the liquid crystal colloid (LCC) system, Wang *et al.* (2017) presented a detailed numerical investigation of the LdG free-energy model under the one-constant approximation for systems of single and double spherical colloidal particles immersed in an otherwise uniformly aligned NLC. For strong homeotropic anchoring with one spherical particle, two types of configuration are obtained, namely quadrupolar (also known as Saturn-ring structure) and dipolar states, as illustrated in Figure 4.4. In the quadrupolar state, a $-1/2$ disclination line forms a ring located at the equator and the entire $\mathbf{Q}$-tensor has an axisymmetry about the z-axis and reflection symmetry with respect to the x–y plane through the centre of the sphere. The dipolar solution is an axisymmetric configuration and contains no reflection symmetry with respect to the x–y plane. The defect ring in the dipolar state is near the top of the sphere. The phase diagram for the single-particle problem is shown in Figure 4.4(g). Below the critical temperature of isotropic–nematic phase transition, the dipolar state is stable for large particle systems and can only be found to the right of the dashed curve, which represents its stability limit. The quadrupolar pattern can be found as the stable or metastable state over the entire parameter space below the critical temperature.

To study the case with two spherical particles of equal radii placed in a nematic fluid, Wang *et al.* (2017) introduced the bispherical coordinates (ξ, μ, ϕ) $(-\xi_0 \leq \xi \leq \xi_0, 0 \leq \mu < \pi$ and $0 \leq \phi < 2\pi)$ (Fukuda *et al.* 2004), and chose real spherical harmonics of (μ, φ) and Legendre polynomials of ζ $(\zeta = \xi/\xi_0)$ as basis functions. The relation between bispherical coordinates (ξ, μ, ϕ) and Cartesian coordinates (x, y, z) is

$$x = a\frac{\sin\mu}{\cosh\xi - \cos\mu}\cos\phi, \quad y = a\frac{\sin\mu}{\cosh\xi - \cos\mu}\sin\phi, \quad z = a\frac{\sinh\xi}{\cosh\xi - \cos\mu},$$

where $a = \sqrt{(D/2)^2 - R^2}$, R is the ball's radius, and D is the distance between the centres of the two spherical particles. At a fixed ϕ, $\xi = \mu = 0$ corresponds to infinity, and the surface of constant ξ represents the sphere given by

$$x^2 + y^2 + (z - a\coth\xi)^2 = \frac{a^2}{\sinh^2\xi}. \tag{4.10}$$

So the surfaces of the two spherical particles are represented by $\xi = \pm\xi_0$ and $\xi_0 = \cosh^{-1}(D/2R)$. Inspired by the configuration of single particles in an NLC, Wang *et al.* (2017) considered the dimer complex composed of a dipole–dipole pair, a quadrupole–quadrupole pair and a dipole–quadrupole pair; see Figure 4.5. They found three stable state configurations in the dimer system, namely an entangled hyperbolic defect (H), unentangled defect rings (U_γ) and parallel dipoles (D_0), after the free energy is minimized with respect to both the far-field nematic director (represented by $\gamma \in [0, \pi/2]$) and inter-particle distance D/R. Both the H and U_γ

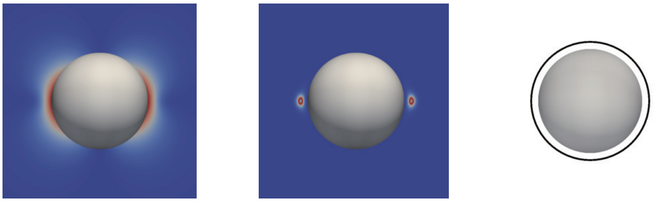

(a) (b) (c) quadrupolar

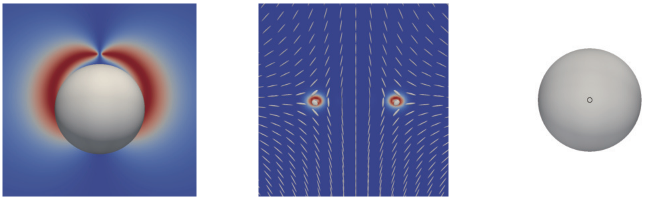

(d) (e) (f) dipolar

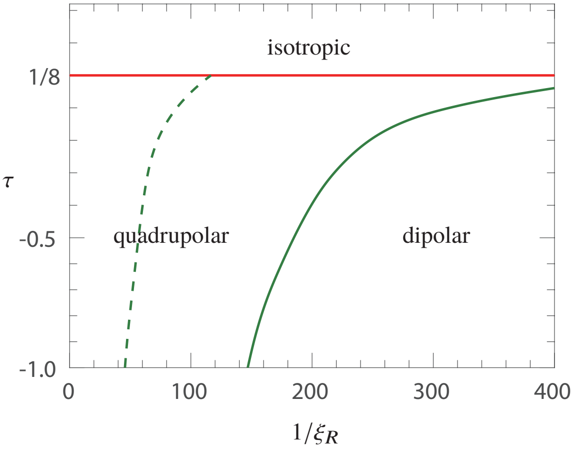

(g) phase diagram

Figure 4.4. (Credit: Wang *et al.* 2017.) Two equilibria of NLCs surrounding a spherical particle: (a–c) quadrupolar state and (d–f) dipolar state, with the corresponding regimes in the phase diagram (g), where these states have the lowest free energies and the dashed line represents the stability limit of the dipolar state. Each state is illustrated by using three views: side views of the **Q**-tensor element Q_{11} (a, d), the same side views of the biaxiality coefficient β (b, e), and top views of the defect location (c, f), indicated by the black circles produced by plotting the isosurface of $c_l = 0.1$. (e) An enlarged version of the defect area on top of the sphere, where the tensor field (white ellipsoids) indicates a $-1/2$ defect line.

states are variations of the quadrupolar structure in Figure 4.4. The H state, in which $\gamma = \pi/2$, is only stable in systems with extremely small particle size. Due to the two defect rings both having the same winding number $-1/2$, in U_γ the portions of the defect rings near the sphere–sphere centre locally repel each other. As these portions are twisted upwards and downwards, the original spherical axes tilt in order to accommodate a larger distance between these two repelling portions. The value of the optimal γ deviates from $\gamma = \pi/2$ starting from the isotropic–nematic transition line and increases as the system moves to a smaller particle size state. In D_0, the far-field tilt angle is given by $\gamma = 0$. Beyond the three free-energy ground states, six metastable states can be computed. We refer the interested reader to Wang *et al.* (2017) for more detailed discussions.

For more complex geometries, phase field approaches or diffuse interface methods (Yue, Feng, Liu and Shen 2004) can be incorporated into the above numerical framework. For example, combining the phase field method with the Fourier spectral method, Wang *et al.* (2018) investigated the formation of three-dimensional colloidal crystals in a nematic liquid crystal dispersed with a large number of spherical particles. They computed the corresponding defect structures in the space-filler nematic liquid crystal induced by the presence of the spherical surface of the colloids, and found multiple configurations for each given particle size and that the most stable state is determined by a comparison of the free energies. Their numerical studies show that from large to small colloidal particles, a sequence of 3D colloidal structures, which range from quasi-one-dimensional (columnar), to quasi-two-dimensional (planar) and truly three-dimensional, are found to exist.

Besides NLCs, similar numerical techniques can be applied to cholesteric LCs. Tong *et al.* (2017) investigated the defect structures around a spherical colloidal particle in a cholesteric LC, *i.e.* $\Omega = \mathbb{R}^3 \backslash B(0,1)$. In order to deal with the inhomogeneity of the cholesteric LC at infinity, they first identified the ground state $\mathbf{Q}_0$ and used spectral methods to approximate $\mathbf{Q} - \mathbf{Q}_0$. Instead of using classical orthogonal systems on the unbounded domain, such as Laguerre polynomials, they combined the exponential mapping and the truncation techniques to capture the property of $\mathbf{Q} - \mathbf{Q}_0$. The mapping between the computational domain (ρ, θ, ϕ) and the physical domain (r, θ, ϕ) is given by

$$r = \sinh\left(\frac{\rho + 1}{2} L\right), \quad \rho \in [-1, 1], \tag{4.11}$$

where r is the radial distance in the spherical coordinates. Figure 4.6 shows two types of defect configurations obtained in a cholesteric LC by their numerical simulation for strong homeotropic anchoring: the twisted Saturn ring (Figures 4.6(a–c)) and the cholesteric dipole (Figures 4.6(d–f)). Similar numerical methods can be used to study defect structures in the cholesteric LC and the blue phase under different geometric constraints (Fukuda *et al.* 2010, Guo *et al.* 2016, Darmon *et al.* 2016).

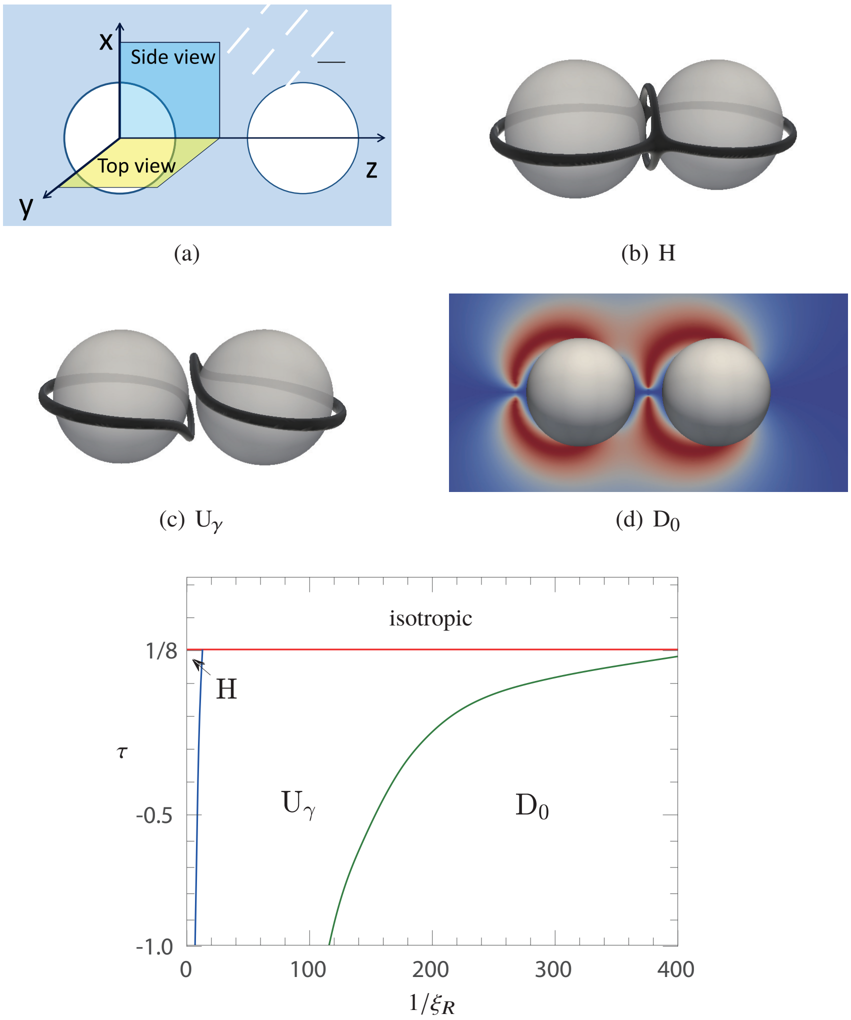

(a) (b) H

(c) U_γ (d) D_0

(e) phase diagram

Figure 4.5. (Credit: Wang *et al.* 2017.) (a) Sketch of the coordinate system for a dimer problem. (b) Entangled hyperbolic defect (H) state where $\gamma = \pi/2$. (c) Unentangled defect rings (U_γ) where $\gamma = \pi/2$. (d) Parallel dipole–dipole state (D_0) where $\gamma = 0$. (e) Phase diagram describing the regimes where these defect states have free-energy minima in terms of a reduced temperature τ and reduced spherical radius $1/\xi_R$. The phase diagram was determined based on the ground-state calculation, after consideration of all other possibilities including minimization with respect to the particle distance D and tilt angle γ. Parts (b) and (c) are illustrations of the defect lines determined from isosurface of the largest eigenvalue of $\mathbf{Q}$, $\lambda_1 = 0.25$; (d) is the cross-section view of Q_{11}.

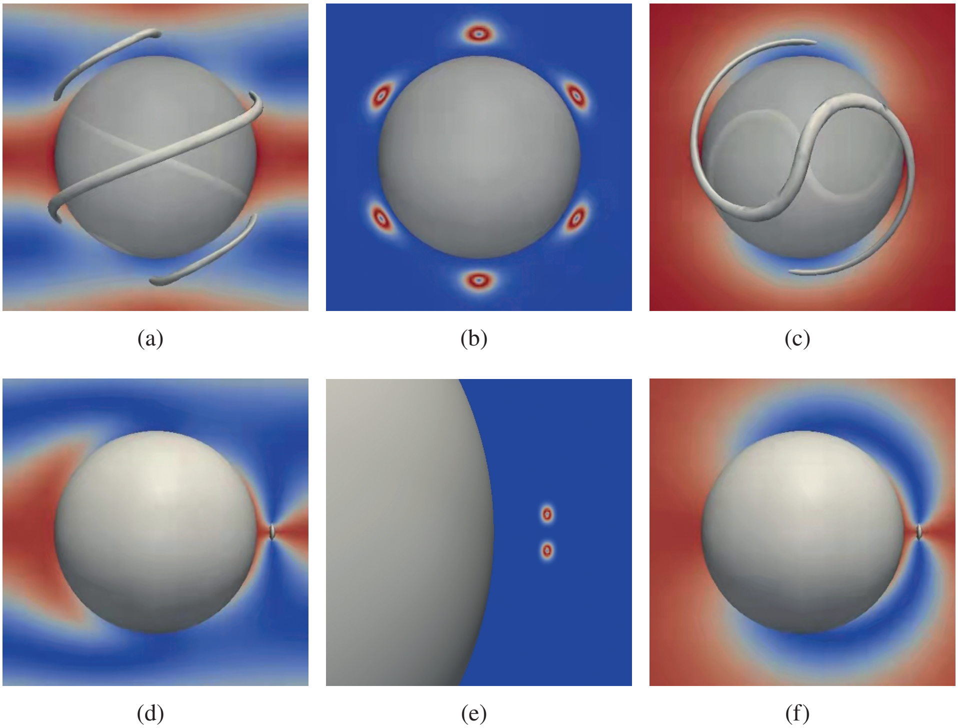

Figure 4.6. (Credit: Tong *et al.* 2017.) Two possible configurations around a spherical particle: (a–c) defect structures in the twisted Saturn ring, (d–f) defect structures in the cholesteric dipole.

4.2. *Gradient flow approach*

Gradient flow is a dynamics driven by a free energy. There are quite a number of works devoted to obtaining the defect patterns by solving the gradient flow equation corresponding to different LC systems (Fukuda *et al.* 2004, Ravnik and Žumer 2009, Canevari *et al.* 2017, Wang *et al.* 2019, MacDonald *et al.* 2020). For the LdG theory, the corresponding L^2-gradient flow equation can be written as

$$\frac{\partial \mathbf{Q}}{\partial t} = -\gamma \frac{\delta \mathcal{F}}{\delta \mathbf{Q}}, \tag{4.12}$$

where $\gamma > 0$ is the dissipative coefficient. An advantage of the gradient flow approach is that it also provides partial information on the dynamical evolution of the defect structure.

From the numerical perspective, the main challenge in developing numerical schemes for gradient flow systems is to maintain the energy dissipation property at the discrete level. During the past few decades, energy-stable numerical schemes for gradient flow systems have been studied extensively; examples include fully implicit schemes (Xu, Li, Wu and Bousquet 2019, Du and Feng 2020), convex splitting methods (Elliott and Stuart 1993, Eyre 1998), stabilization methods (Shen and Yang 2010, Cai, Shen and Xu 2017*a*), invariant energy quadratization (Yang 2016, Zhao, Yang, Gong and Wang 2017) and the scalar auxiliary variable (SAV) approach (Shen *et al.* 2018, Shen, Xu and Yang 2019).

In a recent work, Shen *et al.* (2019) developed a second-order unconditionally energy-stable scheme based on SAV and Crank–Nicolson for the LdG theory, in which the LdG free energy is given by

$$\mathcal{F}[\mathbf{Q}] = \mathcal{F}_{\mathrm{b}}[\mathbf{Q}] + \mathcal{F}_{\mathrm{el}}[\mathbf{Q}, \nabla\mathbf{Q}], \tag{4.13}$$

where

$$\begin{aligned}
\mathcal{F}_{\mathrm{b}} &= \int f_{\mathrm{b}}(\mathbf{Q}) = \int \frac{A}{2}\operatorname{tr}\mathbf{Q}^2 - \frac{B}{3}\operatorname{tr}\mathbf{Q}^3 + \frac{C}{4}(\operatorname{tr}\mathbf{Q}^2)^2 \,\mathrm{d}\mathbf{x},\\
\mathcal{F}_{\mathrm{el}} &= \int \frac{L_1}{2}|\nabla\mathbf{Q}|^2 + \frac{L_2}{2}Q_{ik,i}Q_{jk,j} + \frac{L_3}{2}Q_{jk,i}Q_{ij,k}\,\mathrm{d}\mathbf{x}.
\end{aligned}$$

Here $C > 0$, $L_1 > 0$ and $L_1 + L_2 + L_3 > 0$, so the total energy is bounded from below. Due to the quartic term $C(\operatorname{tr}\mathbf{Q}^2)^2$, there exists $a_1, C_0 > 0$ such that $f_b(\mathbf{Q}) - a_1\operatorname{tr}\mathbf{Q}^2/2 + C_0 > 0$. Let r be the scalar auxiliary variable defined by

$$r(t) = \sqrt{\mathcal{F}_1} := \sqrt{\mathcal{F}_{\mathrm{b}} - \int_\Omega \frac{a_1}{2}\operatorname{tr}\mathbf{Q}^2 + C_0} \tag{4.14}$$

and

$$\mathcal{L} = a_1\mathbf{Q} + \frac{\delta\mathcal{F}_e}{\delta\mathbf{Q}}. \tag{4.15}$$

Then the gradient flow equation can be rewritten as

$$\begin{aligned}
\frac{\partial\mathbf{Q}}{\partial t} &= -\mu,\\
\mu &= \mathcal{L}\mathbf{Q} + \frac{r(t)}{\sqrt{\mathcal{F}_1}}\frac{\delta\mathcal{F}_1}{\delta\mathbf{Q}},\\
r_t &= \frac{1}{2\sqrt{\mathcal{F}_1}}\int_\Omega \frac{\delta\mathcal{F}_1}{\delta\mathbf{Q}} : \mathbf{Q}_t\,\mathrm{d}\mathbf{x}.
\end{aligned} \tag{4.16}$$

The corresponding numerical scheme is given by

$$\begin{aligned}
\frac{\mathbf{Q}^{n+1} - \mathbf{Q}^n}{\Delta t} &= -\mu^{n+1/2},\\
\mu^{n+1/2} &= \frac{1}{2}(\mathbf{Q}^{n+1} + \mathbf{Q}^n) + \frac{r^{n+1} + r^n}{2\sqrt{\mathcal{F}_1[\bar{\mathbf{Q}}^{n+1/2}]}}\frac{\delta\mathcal{F}_1}{\delta\mathbf{Q}}[\bar{\mathbf{Q}}^{n+1/2}],\\
r^{n+1} - r^n &= \int_\Omega \frac{1}{2\sqrt{\mathcal{F}_1[\bar{\mathbf{Q}}^{n+1/2}]}}\left(\frac{\delta\mathcal{F}_1}{\delta\mathbf{Q}}[\bar{\mathbf{Q}}^{n+1/2}]\right)_{ij}(\mathbf{Q}^{n+1}_{ij} - \mathbf{Q}^n_{ij})\,\mathrm{d}\mathbf{x}.
\end{aligned} \tag{4.17}$$

For the LdG free energy with cubic term ($L_4 Q_{kl} Q_{ij,k} Q_{ij,l}$), although the total free energy is not bounded below (Ball and Majumdar 2010), Cai *et al.* (2017*a*) constructed an unconditionally stable numerical scheme for the 2D **Q**-tensor by a stabilizing technique. They also established uniqueness, solvability and convergence for such a scheme. The convergence analysis leads to the well-posedness of the original PDE system for the 2D **Q**-tensor model. They presented several numerical examples to validate and demonstrate the effectiveness of their scheme.

4.3. Machine learning approach

Over the past decade, machine learning has made a huge impact on the research areas of materials and soft matter, showing the highly powerful and effective performance attained by using the techniques of deep learning. Here we just take a recent work by Walters *et al.* (2019) as an example of the LC system to demonstrate this trend. Walters *et al.* (2019) investigated a problem for identifying the topological defects of rod-like molecules confined in a square box from 'images'. Unlike conventional images with correlated physical features, where supervised machine learning has been successful, these images are coordinated files generated from an off-lattice sampling. A single-line structure $[l, x_l, y_l, \theta_l]$ is given for each rod-like molecule, where $[x_l, y_l, \theta_l]$ specifies the location coordinates and angular orientation of the molecule labelled l, and the labels are not related. The task is to identify the four defect patterns from the off-lattice data, and two types of machine-learning procedure are considered: the feedforward neural network (FNN) and the recurrent neural network (RNN). It is shown that FNN is not readily appropriate for studying defect types in this off-lattice model. However, with a coarse-grained position sorting in the initial data input, referred to as *presorting*, effective learning can be realized by FNN. In contrast, RNN performs exceptionally well at identifying defect states in the absence of presorting. Most importantly, Walters *et al.* (2019) pointed out that by dividing the whole image into small cells, an RNN approach with the data in each cell as an input can detect the types and positions of nematic defects in each image instead of the naked eye.

5. Numerical methods for computing liquid crystal hydrodynamics

In this section we review some progress on numerical methods for studying LC hydrodynamics, including vector models, tensor models and molecular models.

5.1. Vector models

An NLC flow behaves like a regular liquid with molecules of similar size, and also displays anisotropic properties due to the molecule alignment, which is usually described by the local director field. The Ericksen–Leslie equations have been used to describe the flow of NLCs, and have attracted much theoretical and numerical research. According to the macroscopic hydrodynamic theory of NLCs established by Ericksen (1961) and Leslie (1979), Lin (1989) proposed simplified Ericksen–Leslie equations for an NLC flow:

$$\begin{cases} \partial_t \mathbf{u} + (\mathbf{u}\cdot\nabla)\mathbf{u} - \nu\Delta\mathbf{u} + \nabla p + \lambda\nabla\cdot((\nabla\mathbf{d})^\top\nabla\mathbf{d}) = \mathbf{0}, \\ \nabla\cdot\mathbf{u} = 0, \\ \partial_t \mathbf{d} + (\mathbf{u}\cdot\nabla)\mathbf{d} - \gamma\Delta\mathbf{d} - \gamma|\nabla\mathbf{d}|^2\mathbf{d} = \mathbf{0}. \end{cases} \tag{5.1}$$

Here $\mathbf{u}$ denotes the solenoidal velocity field, p denotes the pressure, and $\mathbf{d}$ denotes the molecular alignment satisfying a sphere constraint almost everywhere. The positive parameters ν, λ, γ are a fluid viscosity constant, an elastic constant and a relaxation time constant, respectively. The system (5.1) consists of the Navier–Stokes equations coupled with an extra anisotropic stress tensor and a convective harmonic map equation. Although simple, this system retains the core of the mathematical structure, such as strong nonlinearities and constraints, as well as the physical structure, such as the anisotropic effect of elasticity on the velocity vector field $\mathbf{u}$, of the original Ericksen–Leslie system. The first energy equality, which is established under certain boundary conditions, expresses the balance of energy in the system between the kinetic and elastic energies.

Badia *et al.* (2011*b*) provided an excellent overview of the numerical methods for (5.1). Since an almost-everywhere satisfaction of the sphere constraint restriction is not appropriate at a numerical level, two alternative approaches have been introduced: a penalty method and a saddle point method. With a Ginzburg–Landau penalty function $F_\varepsilon(\mathbf{d}) = (|\mathbf{d}|^2 - 1)^2/(4\varepsilon^2)$ to enforce the sphere constraint, a penalty formulation is obtained by weakening the constraint as

$$\begin{cases} \partial_t \mathbf{u} + (\mathbf{u}\cdot\nabla)\mathbf{u} - \nu\Delta\mathbf{u} + \nabla p + \lambda\nabla\cdot((\nabla\mathbf{d})^\top\nabla\mathbf{d}) = \mathbf{0}, \\ \nabla\cdot\mathbf{u} = 0, \\ \partial_t \mathbf{d} + (\mathbf{u}\cdot\nabla)\mathbf{d} + \gamma(f_\varepsilon(\mathbf{d}) - \Delta\mathbf{d}) = \mathbf{0}, \\ |\mathbf{d}| \leqslant 1, \end{cases} \tag{5.2}$$

where $f_\varepsilon(\mathbf{d}) = \nabla_{\mathbf{d}} F_\varepsilon(\mathbf{d})$, and the energy estimate for (5.2) was established by Lin and Liu (1995). Finite element methods of mixed types play an important role when designing numerical approximations for the penalty formulation in order to preserve the intrinsic energy estimate. Alternatively, with a Lagrange multiplier q to enforce the sphere constraint, a saddle point formulation reads as

$$\begin{cases} \partial_t \mathbf{u} + (\mathbf{u}\cdot\nabla)\mathbf{u} - \nu\Delta\mathbf{u} + \nabla p + \lambda\nabla\cdot((\nabla\mathbf{d})^\top\nabla\mathbf{d}) = \mathbf{0}, \\ \nabla\cdot\mathbf{u} = 0, \\ \partial_t \mathbf{d} + (\mathbf{u}\cdot\nabla)\mathbf{d} + \gamma(q\mathbf{d} - \Delta\mathbf{d}) = \mathbf{0}, \\ |\mathbf{d}| = 1, \end{cases} \tag{5.3}$$

and the energy estimate for (5.3) was derived by Badia, Guillén-González and Gutiérrez-Santacreu (2011*a*). These approaches are suitable for their numerical approximation by finite elements, since a discrete version of the restriction is enough to prove the desired energy estimate. The penalized Ginzburg–Landau problem (5.2) can be stated in a saddle point framework as well,

$$\begin{cases} \partial_t \mathbf{u} + (\mathbf{u}\cdot\nabla)\mathbf{u} - \nu\Delta\mathbf{u} + \nabla p + \lambda\nabla\cdot((\nabla\mathbf{d})^\top\nabla\mathbf{d}) = \mathbf{0}, \\ \nabla\cdot\mathbf{u} = 0, \\ \partial_t \mathbf{d} + (\mathbf{u}\cdot\nabla)\mathbf{d} + \gamma(q\mathbf{d} - \Delta\mathbf{d}) = \mathbf{0}, \\ |\mathbf{d}|^2 - 1 = \varepsilon^2 q, \end{cases} \tag{5.4}$$

which establishes a connection between (5.2) and (5.3).

The numerical approximation of the Ericksen–Leslie equations is difficult and computationally expensive because of the coupling between the nonlinear terms and the constraint conditions. Liu and Walkington (2000) dealt with the approximation of (5.2) for 2D domains, and established convergence of finite element approximations under appropriate regularity hypotheses with dependence on the penalty parameter ε. Du, Guo and Shen (2001) studied a Fourier-spectral method for (5.2) by proving its convergence in a suitable sense and establishing the existence of a global weak solution of the original problem and its uniqueness in the 2D case. The error estimates exhibit the spectral accuracy of the Fourier-spectral method, and a fully discrete scheme is constructed with a complete stability and error analysis. Feng and Prohl (2004) proved a convergence result for a Ginzburg–Landau-type equation where the dependence of ε is of polynomial order. Lin and Liu (2006) presented one of the simplest time-stepping schemes for the 2D Ginzburg–Landau problem (5.2), where the space is discretized by H^1-conforming finite elements and time is discretized implicitly with respect to the linear terms and semi-implicitly with respect to the nonlinear terms, while the anisotropic stress tensor is fully explicit. This scheme reduces the computational cost significantly, and larger-scale numerical simulations are allowed because only a sequence of two decoupled linear problems for the velocity–pressure pair and the director field need to be solved separately at each time step. Liu, Shen and Yang (2007) presented an efficient and accurate numerical scheme for (5.2) in a cylinder domain. The time discretization is based on a semi-implicit second-order rotational pressure-correction scheme and the Legendre–Galerkin method is used for the space variable. Annihilation of a hedgehog–antihedgehog pair with different types of transport is simulated numerically.

By introducing an auxiliary variable $\mathbf{w} = \nabla\mathbf{d}$, Liu and Walkington (2002) avoided using Hermite finite elements for the approximation of the director equation in (5.2) and formulated the director equation in the framework of mixed methods. They showed how a mixed method may be used to eliminate the need for Hermite finite elements and establish convergence of the method. Girault and Guillén-González

(2011) considered another auxiliary variable $\mathbf{w} = -\Delta\mathbf{d}$ to avoid the large number of extra degrees of freedom and the nonlinearity of the numerical schemes, and constructed a fully discrete mixed scheme that is linear, unconditionally stable and convergent towards (5.2). With an auxiliary variable $\mathbf{w} = -\Delta\mathbf{d} + f_\varepsilon(\mathbf{d})$, two finite-element Euler time-stepping schemes have been developed that are implicit for the linear terms and semi-implicit for the nonlinear terms. Specifically, Becker *et al.* (2008) proposed a fully implicit approximation to deal with the time integration of f_ε, while Guillén-González and Gutiérrez-Santacreu (2013) suggested a fully explicit one. The time step of the explicit scheme must be quite small if the size of ε is proportional to the space parameter h, but their numerical experiences have been demonstrated to be optimal. Lin, Liu and Zhang (2007) used convenient conformal C^0 finite elements in solving the problem in the weak form, and derived a discrete energy law for a modified midpoint time discretization scheme. A fixed iterative method is used to solve the resulting nonlinear system so that a matrix-free time evolution may be achieved and velocity and director variables may be solved separately.

Becker *et al.* (2008) presented a finite element scheme directly for the Ericksen–Leslie equations (5.1), which is a more difficult task than for the Ginzburg–Landau problem (5.2) because the sphere constraint $|\mathbf{d}| = 1$ is difficult to fulfil at the discrete level. Badia *et al.* (2011*a*) developed a linear semi-implicit algorithm that is unconditionally stable for both the Ginzburg–Landau problem and the Ericksen–Leslie problem, and it does not involve nonlinear iterations. Guillén-González and Koko (2015) proposed a two-substep viscosity-splitting time scheme for (5.3), which is a fully decoupled linear scheme from the computational point of view. The first substep couples diffusion and convection terms whereas the second one is concerned with diffusion terms and constraints. Some numerical experiments in 2D domains are carried out by using only linear finite elements in space, confirming numerically the viability and the convergence of this scheme.

Walkington (2011) considered numerical approximation of the flow of LCs governed by the Ericksen–Leslie equations. Care should be taken to develop numerical schemes that inherit the Hamiltonian structure of these equations and associated stability properties. Zhao, Yang, Li and Wang (2016) developed first-order and second-order coupled energy-stable numerical schemes for a modified Ericksen–Leslie hydrodynamic model, which can reduce to (5.1) with the omission of some terms. They presented two ways to develop decoupled schemes for the model, and showed the energy stability as well. They made prediction comparisons of the modified model with a reduced model, demonstrating quite different but more realistic orientational dynamics in flows of NLCs. Chen, Bao and Zhang (2016) investigated the kinematic transports of the defects in the NLC system by numerical experiments with difference schemes and the semi-implicit scheme which is more efficient although it does not preserve discrete energy relation. The presented development and interaction of the defects are partially consistent with the observation from the experiments.

Simulating the rise of Newtonian drops in an NLC is a computational challenge because of the numerical difficulties in handling moving and deforming interfaces as well as the complex rheology of NLCs. The anisotropic rheology of the LC can be represented by the Ericksen–Leslie theory, regularized to permit topological defects. Zhou, Yue and Feng (2007) simulated the rise of Newtonian drops in an NLC parallel to the far-field molecular orientation by computing the moving interface in a diffuse interface framework. The numerical results revealed interesting coupling between the flow field and the orientational field surrounding the drop, especially the defect configuration. For example, drops with planar anchoring on the surface rise faster than those with homeotropic anchoring due to the viscous anisotropy of the nematic LC. With both types of anchoring, the drag coefficient of the drop decreases with increasing Ericksen number as the flow-alignment of the nematic orientation reduces the effective viscosity of the LC.

LC droplets immersed in another fluid matrix or another liquid droplet immersed in LC matrices have many interesting technological applications (Yue *et al.* 2004). Based on an energetic variational approach, Yue *et al.* (2004) derived a phase field theory for immiscible mixtures of NLCs and viscous fluids. A novel phase transition mechanism is implemented to couple the NLC phase with the viscous fluid phase to arrive at the dissipative hydrodynamic model for incompressible fluid mixtures. Zhou *et al.* (2007) developed a decoupled, linear scheme for a simplified version of the phase field model, as well as a coupled, nonlinear scheme for the full model, and showed them to be unconditionally energy-stable with consistent discrete dissipative energy laws. The effectiveness of the presented numerical examples shows the effectiveness of the new model and the numerical schemes.

A number of models for smectic phase LCs have been developed and studied during the past two decades, and we will take one example of smectic LC hydrodynamics. Chen, Yang and Zhang (2017) considered the numerical approximations for solving a particular hydrodynamics coupled smectic-A model developed by E (1997). The model, which is derived from the variational approach of the modified Oseen–Frank energy, is a highly nonlinear system that couples the incompressible Navier–Stokes equations and a constitutive equation for the layer variable, but appears to be the minimal model of unknowns. The director field is assumed to be strictly equal to the gradient of the layer, and thus the total free energy is reduced to a simplified version with only one order parameter. Rather than imposing a non-convex constraint directly on the gradient of the layer variable, the free energy is modified by adding a Ginzburg–Landau-type penalization potential, which is a commonly used technique in LC theory. Two linear second-order time-marching schemes, which are unconditionally energy-stable, are developed with the invariant energy quadratization method for nonlinear terms in the constitutive equation, the projection method for the Navier–Stokes equations, and some subtle implicit–explicit treatments for the convective and stress terms. Various numerical experiments are presented to demonstrate the stability and the accuracy of the numerical schemes in simulating the dynamics under shear flow and the magnetic field.

5.2. Tensor models

In recent years, more complex problems of modelling the interaction of flow and molecular orientation in LCs have been studied. The hydrodynamic **Q**-tensor model has been applied to the flows of LCs and LC polymers. In particular, the non-dimensionalized hydrodynamic **Q**-tensor model of NLCs,

$$\begin{cases} \partial_t \mathbf{Q} + \mathbf{u}\cdot\nabla\mathbf{Q} - \mathbf{S}(\nabla\mathbf{u},\mathbf{Q}) = M\mathbf{H}, \\ \nabla\cdot\mathbf{u} = 0, \\ \partial_t \mathbf{u} + \mathbf{u}\cdot\nabla\mathbf{u} = -\nabla p + \eta\Delta\mathbf{u} + \nabla\cdot\Sigma - \mathbf{H}\nabla\mathbf{Q}, \end{cases} \tag{5.5}$$

can be derived from a variational approach together with the generalized Onsager principle. The molecular field **H**, which provides the driving motion, is related to the derivative of the free energy. For more details see Beris and Edwards (1994) and Wang (2002). Zhao and Wang (2016) developed first-order and second-order coupled energy-stable numerical schemes for the **Q**-tensor-based hydrodynamic model of NLC flows. They extended the first-order coupled scheme to a decoupled scheme, which is energy-stable as well. With the fully coupled schemes implemented in 2D space and time, they studied the defect dynamics for flow of NLCs in a channel. The methodology developed also provides a paradigm for developing energy-stable schemes for general hydrodynamic models of complex fluids with an energy dissipation law. Furthermore, Zhao *et al.* (2017) developed a second-order semi-discrete scheme in time, which is linear and unconditionally energy-stable at the semi-discrete level, to solve the governing system of equations by following the novel ‘energy quadratization’ strategy. Several numerical examples have been presented to demonstrate the usefulness of the model and the effectiveness of the numerical scheme in simulating defect dynamics in flows of LCs. Denniston, Orlandini and Yeomans (2001) described a lattice Boltzmann algorithm to simulate LC hydrodynamics in terms of a tensor order parameter, including a molecular field that provides the driving motion. They described a lattice Boltzmann algorithm in detail to simulate LC hydrodynamics. Backflow effects and the hydrodynamics of topological defects are naturally included in the simulations, as are non-Newtonian flow properties such as shear thinning and shear banding.

Ramage and Sonnet (2016) considered the NLC in a spatially inhomogeneous flow with a second-rank alignment tensor, whose evolution is determined by two coupled equations: a generalized Navier–Stokes equation for the flow, and a convection–diffusion-type equation for the alignments. A specific model with three viscosity coefficients allows the contribution of the orientation to the viscous stress to be cast in the form of an orientation-dependent force, which effectively decouples the flow and orientation to circumvent the fully coupled problem. They illustrated a time-discretized strategy for solving the flow-orientation problem using the Stokes flow in a lid-driven cavity.

Dispersing colloidal particles into LCs provides an approach to building a novel class of composite materials with potential applications. Much research has been devoted to the hydrodynamic equations governing their dynamical evolution to understand the physics and dynamical properties of such colloidal LC composites. Foffano *et al.* (2014) provided an overview of the theoretical understanding of the hydrodynamic properties of such materials from computer simulations, including a single particle and two particles forming a dimer and dispersion. They also raised a number of open questions in the dynamics of colloidal LC composites.

5.3. Molecular models

For the liquid crystalline polymer (LCP) model, the Doi–Hess theory by Doi and Edwards (1988) and Hess (1976) is the simplest and the most studied model. Many interesting dynamics have been found in rod-like nematic LCPs in a shear flow. Li *et al.* (2004) considered the stochastic model of concentrated LCPs in plane Couette flow, where the flow is one-dimensional while the configuration variable of the rod is restricted to the circle, and presented the local existence and uniqueness theorem for the solution to the coupled fluid–polymer system. Ji *et al.* (2008) considered the extended Doi model for nematic LCPs in the planar shear flow and studied the formation of microstructure and the dynamics of defects. They discretized the Fokker–Planck equation with the spherical harmonic spectral method and replicated multiple flow modes in the simulations. Ji *et al.* (2008) also gave a comparison between complete closure models, Bingham closure models and kinetic models.

Yu and Zhang (2007) presented a new kinetic hydrodynamic coupled model for the dilute LCP solution for inhomogeneous flow, which accounts for translational diffusion and density variation. The coupled kinetic hydrodynamic model is a combination of an extended Doi kinetic theory for rigid rod-like molecules and the Navier–Stokes equation for incompressible flow. They studied the microstructure formation and defect dynamics arising in LCPs in plane shear flow with mass conservation of LCPs in the whole flow region. The LCP molecular director is restricted in the shear plane, and LCP molecules are ensured anchoring at the boundary by an additional boundary potential. Plane Couette flow and Poiseuille flow were studied with a second-order difference scheme and the fourth-order Runge–Kutta method for time-stepping. Their numerical results in plane Couette flow predicted seven in-plane flow modes, four of which were reported by Rey and Tsuji (1998). In plane Poiseuille flow, the micro-morph is quasi-periodic in time when flow viscosity and molecular elasticity are comparable. Different local states, such as flow-alignment, tumbling or wagging, arise in different flow regions. To describe the microstructures and defect dynamics of LCP solutions, Yu, Ji and Zhang (2010) later proposed a general non-homogeneous extension of Doi's kinetic theory with translational diffusion and non-local potential. A reduced second-order moment model for isotropic long-range elasticity was obtained as an effective tool for numerical simulations of defect dynamics and texture evolution.

Their numerical results of in-plane rotational case show that this model qualitatively predicts complicated non-homogeneous director dynamics under moderate nematic potential strength, and the translational diffusion plays an important role in defect dynamics.

6. Numerical methods for computing transition pathways and the solution landscape of liquid crystals

NLCs often exhibit a number of ordered phases. When an ordered phase is metastable, phase transition proceeds via nucleation and growth under thermal fluctuations or external perturbations. Such a transition is often called a rare event, and can be characterized by a long waiting period around one local metastable state and followed by a sudden jump over the transition state to another stable state (Hänggi, Talkner and Borkovec 1990). Because the transition state is an unstable critical point of the LC free energy, *i.e.* an index-1 saddle point with a single unstable direction that connects two local minima, it is a great challenge to accurately compute the transition states and the transition pathways.

In this section we will first review the numerical methods to compute the transition states and transition pathways. Then we will introduce a novel solution landscape, which describes a pathway map consisting of all stationary points (*i.e.* extrema and saddle points) and their connections.

6.1. *Transition pathways*

There are two popular approaches to finding the saddle points and transition pathways. One is the class of surface-walking methods for finding saddle points starting from a single state, such as gentlest ascent dynamics (E and Zhou 2011) and the dimer-type method (Henkelman and Jónsson 1999, Zhang and Du 2012). The other approach is categorized as path-finding methods for computing a minimal energy path (MEP) that involves two end-states, including the nudged elastic band method (Jónsson *et al.* 1998) and the string method (E *et al.* 2002).

In the case when the object of interest is the most probable transition path between metastable/stable states of the smooth potential energy, it is known that for overdamped Langevin dynamics the most probable path for the transition is the MEP. This purpose is well served by the string method, which was first proposed by E, Ren and Vanden-Eijnden (2002) and has some variants (E, Ren and Vanden-Eijnden 2007, Du and Zhang 2009, Ren and Vanden-Eijnden 2013, Samanta and E 2013). The string method proceeds by evolving a string ϕ with intrinsic parametrization in the configuration space by using steepest descent dynamics for the MEP:

$$\boldsymbol{\phi}_t = -\nabla F^{\perp}(\boldsymbol{\phi}) + \lambda \boldsymbol{\tau}, \tag{6.1}$$

where $\nabla F^{\perp}(\boldsymbol{\phi})$ is the component of ∇F normal to $\boldsymbol{\phi}, \boldsymbol{\tau}$ denotes the unit tangent vector to $\boldsymbol{\phi}$, and λ is the Lagrange multiplier to impose the equal arc length constraint.

In the numerical algorithm, the string $\boldsymbol{\phi}$ is discretized to N nodes $\{\mathbf{Q}_i^n, i = 1, \ldots, N\}$, where n represents the iteration step. The string method adopts a time-splitting scheme via the following two-step procedure.

Step 1: string evolution. The current path $\{\mathbf{Q}_i^n, i = 1, \ldots, N\}$ is updated by following the gradient descent direction:

$$\bar{\mathbf{Q}}_i^{n+1} = \mathbf{Q}_i^n - \alpha_i \nabla F^{\perp}[\mathbf{Q}_i^n], \quad i = 1, 2, \ldots, N, \tag{6.2}$$

where α_i is a step size that is chosen as a constant or determined by the line search.

Step 2: string reparametrization. The nodes $\bar{\mathbf{Q}}_i^{n+1}$ are redistributed to obtain a new path $\mathbf{Q}_i^{n+1}$ by enforcing the equal arc length parametrization. One can calculate the arc length corresponding to the current nodes $\bar{\mathbf{Q}}_i^{n+1}$ and then use a linear or cubic spline interpolation to find $\mathbf{Q}_i^{n+1}$ by the equal arc length.

Parametrization by equal arc length gives good accuracy for the MEP, but not for the transition state. To achieve better estimation of the transition state and the energy barrier, one way is to use the energy-weighted arc length so that finer resolution can be achieved around the transition state (E *et al.* 2007). If the final minima are far from the transition state and too many nodes are needed for the whole MEP, the free-end nudged elastic band method can be used to obtain subtle detail around the transition state by allowing the last node not to be a minimum (Zhu *et al.* 2007).

To improve the accuracy of both the MEP and the transition state without using too many nodes, Han *et al.* (2019) proposed a multiscale scheme of the string method by applying a global coarse string and a local fine string. The global coarse string is used to obtain the whole MEP by connecting two minima, and then the local fine string is utilized to compute the local MEP by choosing two nodes with the highest energies on the global coarse string as the two ends for the case of a single energy barrier. Both strings follow the same two-step procedure described above to make the implementation straightforward, and better estimation of the transition state can be achieved by the local fine string. They implement the multiscale string method on numerical simulations of the transition pathway in a three-dimensional cylinder between PR and PP, with and without axial invariance, between ER and PP or ERRD for different values of temperature and cylinder radius.

For example, the transition pathway between ER and PP for fixed temperature and cylinder radius is shown in Figure 6.1. A pair of $+1/2$ disclination lines starts to form in the middle of the cylinder. These two disclination lines appear to join both their ends, hence forming a disclination ring (Figure 6.1(b)). The width of the ring is increasing when it is less than the distance between defects of a stable 2D PP layer (Figure 6.1(c)). Finally, the ring is broken by the top and bottom boundary and the line defect straightens to the PP line defect configuration (Figure 6.1(d)).

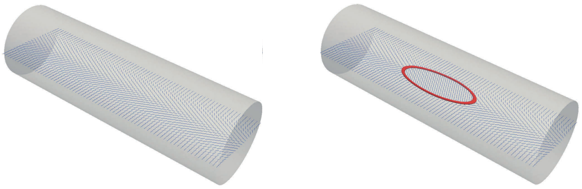

(a) escape radial (ER) (b) transition state

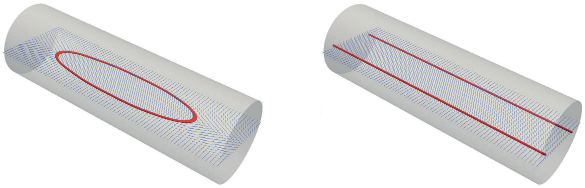

(c) intermediate state (d) planar polar (PP)

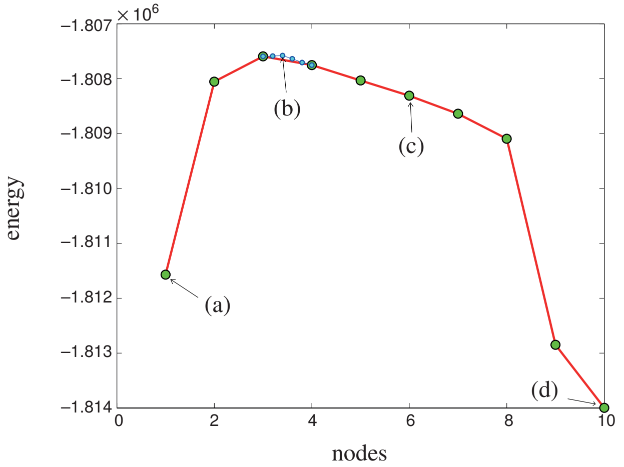

(e) minimum energy path

Figure 6.1. (Credit: Han *et al.* 2019.) Transition pathway from ER to PP. (a–d) Four states along the MEP (e), corresponding to the ER (a), the transition state (b), an intermediate state (the sixth node) (c) and the PP (d), respectively. In the MEP (e), the red line with green beads is the global coarse string and the blue line with blue beads is the local fine string.

The local fine string in Figure 6.1 finds a more accurate transition state than the global coarse string.

6.2. *Saddle points*

The classical transition state theory describes a sufficiently accurate transition process for systems with smooth energy landscapes. On the energy landscape, the transition state is a saddle point with the lowest energy that connects two neighbouring local minima, *i.e.* the index-1 saddle point. As long as the transition state is located, one can calculate the MEP using gradient flow from the transition state perturbed along both sides of its unstable direction.

Extensive surface-walking methods have been proposed to search for saddle points. A key character of such methods is to perform a systematic search for a saddle point starting from a given initial state, without knowing the final states. In this subsection we focus on a typical class of surface-walking methods, the so-called minimum-mode-following methods, where only the lowest eigenvalue and the corresponding eigenvector of the Hessian are needed and subsequently used together with the energy gradient (often referred to as the force) to compute transition states. Besides the eigenvector-following method of Cerjan and Miller (1981), the trajectory-following algorithm of Vincent, Goh and Teo (1992), the activation–relaxation technique of Mousseau and Barkema (1998) and the step and slide method of Miron and Fichthorn (2001), there are also examples of surface-walking methods, and we refer to the excellent reviews by Vanden-Eijnden *et al.* (2010) and Zhang, Ren, Samanta and Du (2016*b*).

E and Zhou (2011) proposed gentlest ascent dynamics, which is a dynamical formulation of the gentlest ascent method of Crippen and Scheraga (1971). It refers to the dynamical system

$$\begin{cases} \dot{\mathbf{x}} = -\nabla E(\mathbf{x}) + 2\dfrac{\langle \nabla E(\mathbf{x}), \mathbf{x}\rangle}{\langle \mathbf{v}, \mathbf{v}\rangle}\mathbf{v}, \\ \dot{\mathbf{v}} = -\nabla^2 E(\mathbf{x})\mathbf{v} + \dfrac{\langle \mathbf{v}, \nabla^2 E(\mathbf{x})\mathbf{v}\rangle}{\langle \mathbf{v}, \mathbf{v}\rangle}\mathbf{v}, \end{cases} \tag{6.3}$$

where $E(\cdot)$ represents the energy functional. Besides the position variable $\mathbf{x}$, another variable $\mathbf{v}$ represents the unstable direction. The dynamics (6.3) can drive $\mathbf{x}$ to climb out of the basin of attraction by following the ascent direction $\mathbf{v}$, which is the eigenvector that corresponds to the smallest eigenvalue of its Hessian, to find the saddle point. E and Zhou (2011) proved that the stable fixed points of this dynamical system are precisely the index-1 saddle points.

To avoid the calculation of the Hessian, Henkelman and Jónsson (1999) developed a dimer method using only first derivatives. Specifically, a dimer with two points is placed at the current position to compute the Hessian-vector multiplication with a finite difference scheme. The dimer method proceeds by alternately performing the rotation step for finding the lowest eigenmode and the translation step by using the modified force with either the steepest descent algorithm or the conjugate gradient method to search for the saddle point. Later, Zhang and Du (2012) proposed a shrinking dimer dynamics by introducing a dynamic reduction of the dimer length, and proved linear stability and convergence results for such dynamics. To accelerate the convergence and further improve the efficiency of the dimer-type methods, Zhang *et al.* (2016*a*) developed an optimization-based shrinking dimer (OSD) method by establishing a minimax optimization for the saddle searching problem and finding the unstable direction in an optimization framework. All these methods can be applied to the LC models for identifying the transition states accurately (Han *et al.* 2019).

Besides the investigations of the minima and index-1 saddle points on the energy landscape of NLCs in confinement, there has been substantial recent interest in the high-index saddle points of the LdG free energy, which are stationary points of the NLC free energy. The Morse index of a saddle point is the maximal dimension of a subspace on which its Hessian is negative definite, which is equal to the number of negative eigenvalues of its Hessian (Milnor *et al.* 1969). For example, a stable stationary point has index 0 and a transition state is an index-1 saddle point. In recent years, powerful numerical algorithms have been developed to find multiple solutions of nonlinear equations, including the gradient-square-minimization method (Angelani *et al.* 2000), the minimax method (Li and Zhou 2001), the deflation technique (Farrell *et al.* 2015) and the homotopy method (Mehta 2011, Hao, Hauenstein, Hu and Sommese 2014). Despite substantial progress in this direction, it is still a numerical challenge to systematically find saddle point solutions, especially those with high indices, of nonlinear systems of partial differential equations such as the Euler–Lagrange equation. Yin *et al.* (2019) proposed a high-index saddle dynamics (HiSD) to efficiently compute the saddle points of any index (including minima) for the LdG energy (Han *et al.* 2020*b*).

For a non-degenerate index-k saddle point $\hat{\mathbf{x}}$, the Hessian $\mathbb{H}(\mathbf{x}) = \nabla^2 E(\mathbf{x})$ at $\hat{\mathbf{x}}$ has exactly k negative eigenvalues $\hat{\lambda}_1 \leqslant \cdots \leqslant \hat{\lambda}_k$ with corresponding unit eigenvectors $\hat{\mathbf{v}}_1, \ldots, \hat{\mathbf{v}}_k$ satisfying $\langle \hat{\mathbf{v}}_j, \hat{\mathbf{v}}_i \rangle = \delta_{ij}$, $1 \leqslant i, j \leqslant k$. Define a k-dimensional subspace $\hat{\mathcal{V}} = \operatorname{span}\{\hat{\mathbf{v}}_1, \ldots, \hat{\mathbf{v}}_k\}$. Then $\hat{\mathbf{x}}$ is a local maximum on a k-dimensional linear manifold $\hat{\mathbf{x}} + \hat{\mathcal{V}}$ and a local minimum on $\hat{\mathbf{x}} + \hat{\mathcal{V}}^\perp$, where $\hat{\mathcal{V}}^\perp$ is the orthogonal complement space of $\hat{\mathcal{V}}$.

The HiSD dynamics for a k-saddle (k-HiSD) is given as follows:

$$\begin{cases} \beta^{-1}\dot{\mathbf{x}} = -\left(\mathbf{I} - 2\displaystyle\sum_{j=1}^{k} \mathbf{v}_j \mathbf{v}_j^\top\right) \nabla E(\mathbf{x}), \\ \gamma^{-1}\dot{\mathbf{v}}_i = -\left(\mathbf{I} - \mathbf{v}_i\mathbf{v}_i^\top - 2\displaystyle\sum_{j=1}^{i-1} \mathbf{v}_j \mathbf{v}_j^\top\right) \mathbb{H}(\mathbf{x})\mathbf{v}_i, \quad i = 1, \ldots, k, \end{cases} \tag{6.4}$$

where the state variable $\mathbf{x}$ and k direction variables $\mathbf{v}_i$ are coupled, $\mathbf{I}$ is the identity operator and $\beta, \gamma > 0$ are relaxation parameters. The k-HiSD dynamics (6.4) is coupled with an initial condition:

$$\mathbf{x}(0) = \mathbf{x}^0 \in \mathbb{R}^n, \quad \mathbf{v}_i(0) = \mathbf{v}_i^0 \in \mathbb{R}^n,\ i = 1, \ldots, k, \tag{6.5}$$

where $\mathbf{v}_1^0, \ldots, \mathbf{v}_k^0$ satisfy the orthonormal condition $\langle \mathbf{v}_i^0, \mathbf{v}_j^0 \rangle = \delta_{ij}, i, j = 1, 2, \ldots, k$. The first equation in (6.4) describes a transformed gradient flow, which allows $\mathbf{x}$ to move along ascent directions on the subspace $\hat{\mathcal{V}}$ and descent directions on the subspace $\hat{\mathcal{V}}^\perp$. The second equation in (6.4) is used to search for an orthonormal basis of $\hat{\mathcal{V}}$. Because the Hessian $\mathbb{H}(\mathbf{x})$ is self-adjoint in a gradient system, we can simply take $\mathbf{v}_i$ as a unit eigenvector corresponding to the ith smallest eigenvalue of $\mathbb{H}(\mathbf{x})$, which can be obtained from a constrained optimization problem,

$$\min_{\mathbf{v}_i \in \mathbb{R}^n} \langle \mathbb{H}(\mathbf{x})\mathbf{v}_i, \mathbf{v}_i \rangle \quad \text{subject to } \langle \mathbf{v}_j, \mathbf{v}_i \rangle = \delta_{ij},\ j = 1, 2, \ldots, i. \tag{6.6}$$

Then we minimize the k Rayleigh quotients (6.6) simultaneously by solving the second equation in (6.4). Furthermore, one can apply the locally optimal block preconditioned conjugate gradient (LOBPCG) method (Knyazev 2001) to calculate the smallest k eigenvalues and $\mathbf{v}_1, \ldots, \mathbf{v}_k$.

6.3. *Solution landscape of liquid crystals*

The solution landscape is a novel concept, which is defined as a pathway map consisting of all stationary points and their connections, presenting a hierarchy structure to show how minima are connected with index-1 saddle points, and how lower-index saddle points are connected to higher-index ones and finally to a parent state, *i.e.* the highest-index saddle point (Yin *et al.* 2020*a*). Solution landscapes not only advance the understanding of the relationships between the minima and the transition states on the energy landscape but also provide a full picture of the entire family of stationary points in both gradient systems and dynamical systems (Yin, Yu and Zhang 2020*b*).

To construct a solution landscape, one needs to apply HiSD and follow two algorithms – downward search to find all connected low-index saddles from a high-index saddle and upward search to find a connected high-index saddle – which drive the entire search to navigate up and down on the energy landscape (Yin *et al.* 2020*a*).

Downward search algorithm. Given an index-m saddle point $\hat{\mathbf{x}}$ and m unit eigenvectors $\hat{\mathbf{v}}_1, \ldots, \hat{\mathbf{v}}_m$ corresponding to the m negative eigenvalues $\hat{\lambda}_1 \leqslant \cdots \leqslant \hat{\lambda}_m$ of the Hessian $\mathbb{H}(\hat{\mathbf{x}})$ respectively, we search for a lower index-k ($k < m$) saddle point using HiSD dynamics (6.4). For the initial condition, we choose $\mathbf{x}(0) = \hat{\mathbf{x}} \pm \varepsilon\mathbf{u}$ for $\mathbf{x}$, where we perturb $\hat{\mathbf{x}}$ along a direction $\mathbf{u}$ with a small ε. The direction $\mathbf{u}$ can be chosen as $\hat{\mathbf{v}}_i$ or a linear combination of $(m - k)$ vectors in the set of unstable directions $\{\hat{\mathbf{v}}_{k+1}, \ldots, \hat{\mathbf{v}}_m\}$, whose negative eigenvalues have the smallest magnitudes. The other k eigenvectors $\hat{\mathbf{v}}_1, \ldots, \hat{\mathbf{v}}_k$ are the initial unstable directions $\mathbf{v}_i(0)$. A typical choice of initial conditions in a downward search is $(\hat{\mathbf{x}} \pm \varepsilon\hat{\mathbf{v}}_{k+1}, \hat{\mathbf{v}}_1, \ldots, \hat{\mathbf{v}}_k)$.

Normally a pair of index-k saddles can be found, corresponding to the ± sign of the initial searching direction.

Upward search algorithm. We can also search a high index-k saddle from a low index-m saddle $\hat{\mathbf{x}}$ ($m < k$) by using the HiSD method. Starting at an index-m saddle $\hat{\mathbf{x}}$, to search for a high index-k saddle, $(k - m)$ other unit eigenvectors $\hat{\mathbf{v}}_{m+1}, \dots, \hat{\mathbf{v}}_k$ corresponding to the smallest $k - m$ positive eigenvalues of the Hessian $\mathbb{H}(\hat{\mathbf{x}})$ are needed. The initial state $\mathbf{x}(0)$ is set as $\hat{\mathbf{x}} \pm \varepsilon \mathbf{u}$, where $\mathbf{u}$ is a linear combination of $\{\hat{\mathbf{v}}_{m+1}, \dots, \hat{\mathbf{v}}_k\}$, and a typical initial condition for k-HiSD in an upward search is $(\hat{\mathbf{x}} \pm \varepsilon \hat{\mathbf{v}}_k, \hat{\mathbf{v}}_1, \dots, \hat{\mathbf{v}}_k)$.

Each downward or upward search represents a pseudodynamics between a pair of saddle points, which presents valuable insights into transition pathways between stable and unstable solutions and the corresponding energy barriers. By repeating downward search and upward search, we are able to systematically find saddle points of all indices and uncover the complex connectivity of the solution landscape.

Yin *et al.* (2020*a*) demonstrated the success of the solution landscape and applied the LdG model to construct the pathway maps of 2D NLCs confined in a square domain with tangent boundary conditions (see Figure 6.2). One of the technical advantages of this method is to produce the entire family tree under a parent state.

For small nanoscale square domains, it is known that the well order reconstruction solution (WORS) is the unique solution with isotropic diagonals and is the global energy minimum in this asymptotic regime (Kralj and Majumdar 2014, Canevari *et al.* 2017). Moreover, the existence of WORS can be proved in arbitrarily sized nematic wells (Majumdar, Milewski and Spicer 2016). By studying the second variation of LdG free energy numerically, Wang *et al.* (2019) showed that the WORS is a high-index saddle point in a large well. In Figure 6.3(a), the Morse index of the WORS increases with the domain size and the WORS is always the parent state in the solution landscapes on a square domain. Intuitively, this is because the length of the diagonal defect lines increases as the domain size increases, and thus the WORS has an increasing number of unstable directions and an increasing Morse index with the increasing square edge length. Using WORS as the parent state (the highest-index saddle) and the HiSD method (Yin *et al.* 2019), Yin *et al.* (2020*a*) constructed a solution landscape on the square domain in Figure 6.2 and reported novel saddle point solutions with multiple interior defects, such as $N\pm$, $M\pm$, $S\pm$ and $T\pm$, that were not reported in the existing literature. Besides these new solutions, a solution landscape provides rich information on dynamical pathways. For example, two movies (a dynamic downward pathway sequence and an upward pathway sequence: see Figure 6.2) are shown in Yin *et al.* (2020*a*) to demonstrate the hidden physical processes and transitions on the complicated energy landscape of NLCs.

The solution landscape of the NLC system can be affected by many factors, such as material properties, external fields, temperature, boundary conditions and domain size and shape. Compared to a square domain, a hexagon is a generic

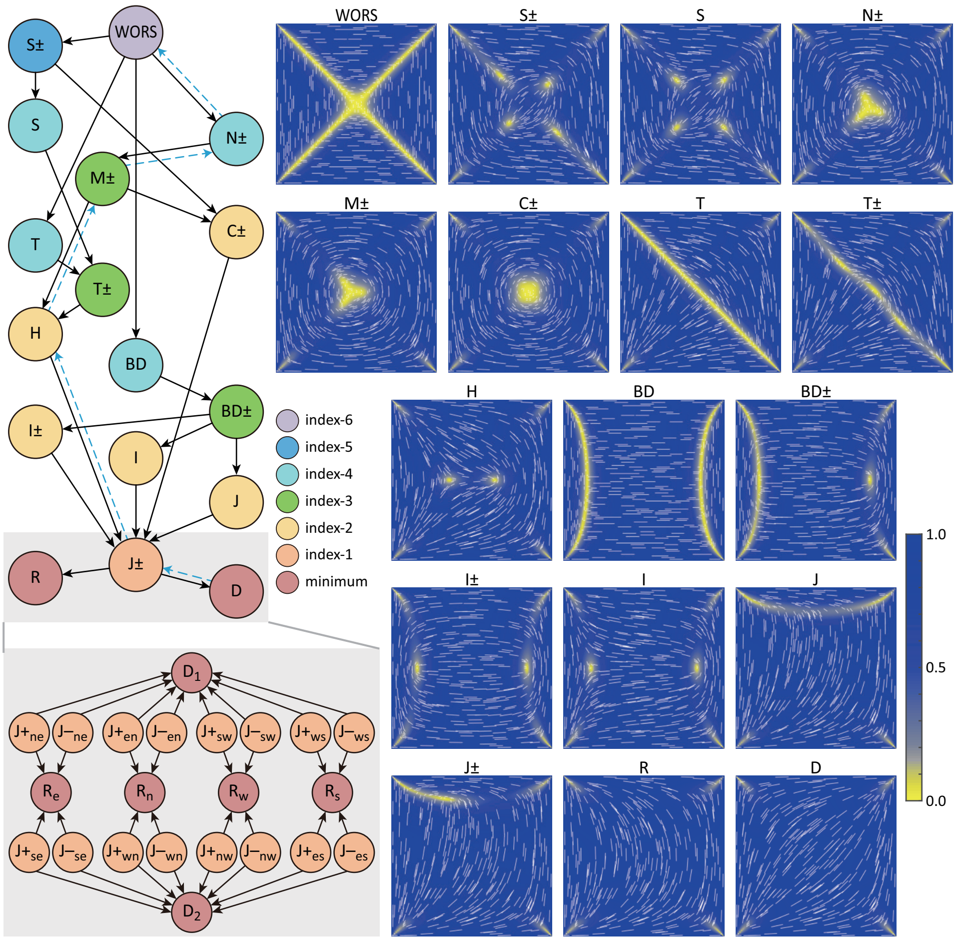

Figure 6.2. (Credit: Yin *et al.* 2020*a*.) Solution landscape of NLCs confined on a square for domain size $\lambda^2 = 50$.

regular polygon with an even number of sides. Han *et al.* (2020*b*) investigated the solution landscapes of NLCs confined in a hexagon with tangent boundary conditions. The ring solution, which is the analogue of the WORS, is a minimizer on a hexagon when the parameter of domain size λ is small enough. However, the ring solution becomes and remains an index-2 saddle point solution for large λ, *i.e.* the Morse index of the ring solution does not increase with λ. By using the HiSD method, the parent states in the solution landscapes of NLCs on a hexagon are found to be the ring solution, the index-3 T135 solution and the index-14 H* solution, where $\lambda^2 = 70$, 120 and 600 in Figure 6.3(b) respectively, and where T135 and H* solutions emerge through saddle-node bifurcations.

In the NLC system confined on a hexagon, the solution landscape is very complicated at $\lambda^2 = 600$ in Figure 6.4(a). There are three notable numerical findings,

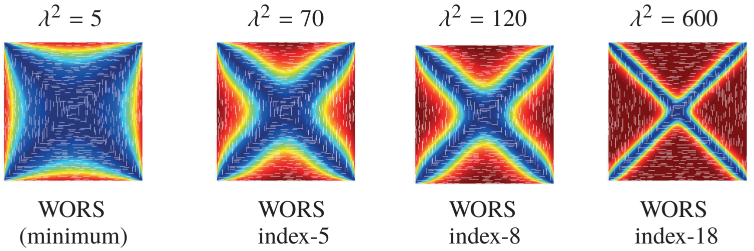

(a) parent state on a square

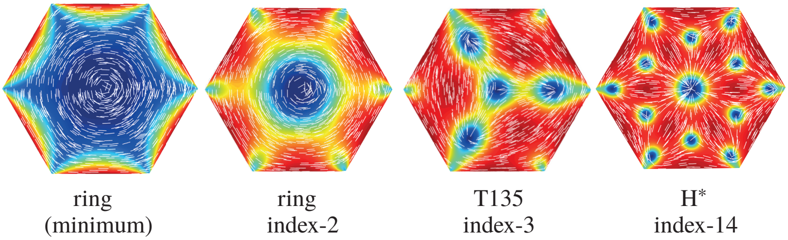

(b) parent state on a hexagon

Figure 6.3. (Credit: Han *et al.* 2020*b*.) Comparison of the parent states of the solution landscapes on the square (a) and the hexagon (b). The domain sizes are $\lambda^2 = 5$, 70, 120 and 600, respectively.

including a new stable T solution with an interior $-1/2$ defect, new H and TD classes of saddle point solutions with high symmetry and high indices, and new saddle points with asymmetric defect locations. Novel H class solutions with interior point defects have Morse indices ranging from 8 to 14, and the connectivity of these solutions is shown in Figure 6.4(b), as well as the corresponding configurations and their defect profiles. The parent state is the index-14 H* saddle point solution connecting to the lowest index-8 saddle point solution, labelled as H. The H class solutions look very similar to each other at first glance and their subtle differences are illustrated by plotting $|\mathbf{Q} - \mathbf{Q}^H|$, where $\mathbf{Q}$ is a critical point solution in the H class and $\mathbf{Q}^H$ is the index-8 H solution. The differences concentrate on the vertices with conspicuous red or white points in the dark blue background (Figure 6.4(b)). The vertex with a pinned $+1/3$ defect and a splay profile of direction is referred to as a *splay-like vertex*. The vertex with a $-1/6$ defect and a bend profile of direction is referred to as a *bend-like vertex*. These conspicuous points are localized near or at the bend-like vertices. The TD class solutions, in which TD is an abbreviation for ‘triangle double’, appear to be a superposition of two ring solutions on a regular triangle, with two interior $-1/2$ point defects and an interior $+1/2$ point defect. All saddle points in this class have three defective vertices, either bend-like or splay-like, and the connectivity of this class is shown in Figure 6.4(c). The lowest-index saddle point solution in this class is the index-3 TD solution with no bend-like vertices.

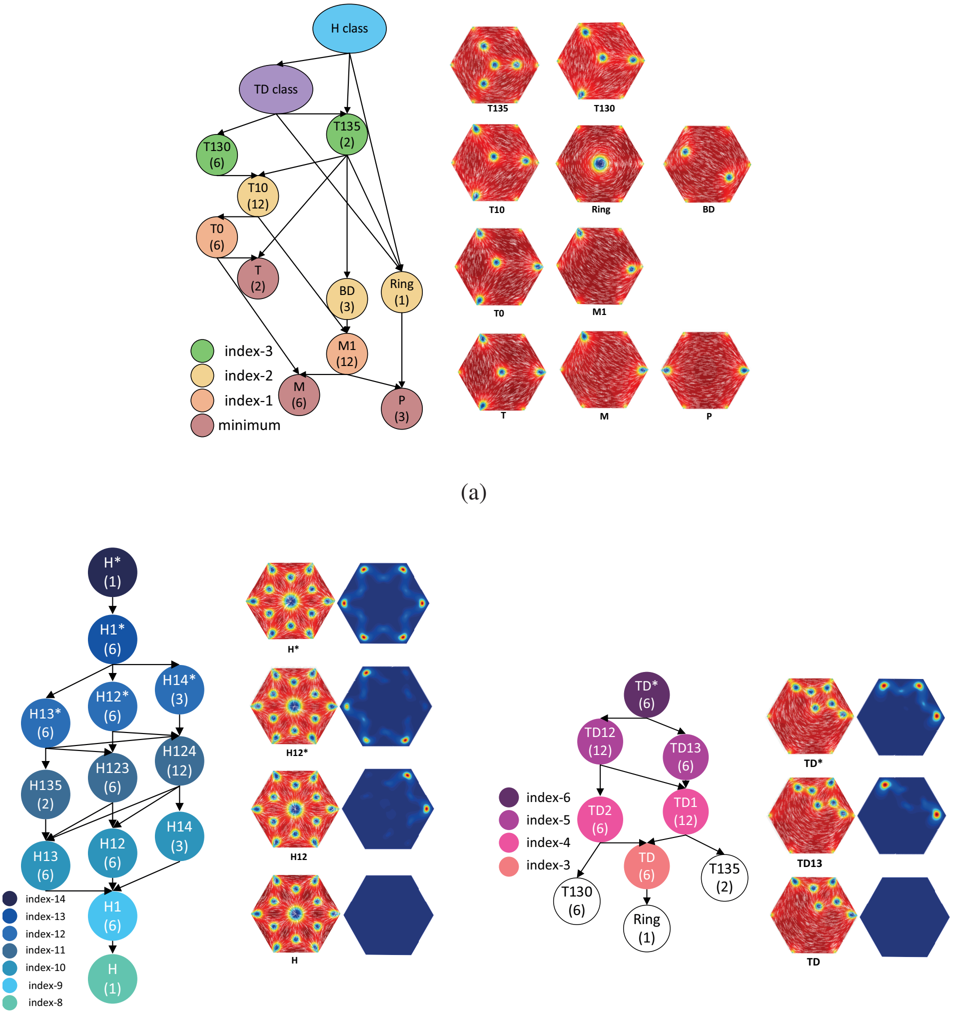

(a)

(b)

(c)

Figure 6.4. (Credit: Han *et al.* 2020*b*.) (a) Solution landscape on a hexagon at $\lambda^2 = 600$. The number in parentheses indicates the number of solutions without taking symmetry into account. The height of a node approximately corresponds to its energy. (b) Solution landscape of the H class, and the configurations of sample solutions and the corresponding plots of $|\mathbf{Q} - \mathbf{Q}^H|$, where $\mathbf{Q}$ is the sample solution in the H class and $\mathbf{Q}^H$ is the index-8 H solution. (c) Solution landscape of the TD class, and the configurations of sample solutions and the corresponding plots of $|\mathbf{P} - \mathbf{P}^{TD}|$, where $\mathbf{P}$ is the sample solution in the TD class and $\mathbf{P}^{TD}$ is the index-3 TD solution.

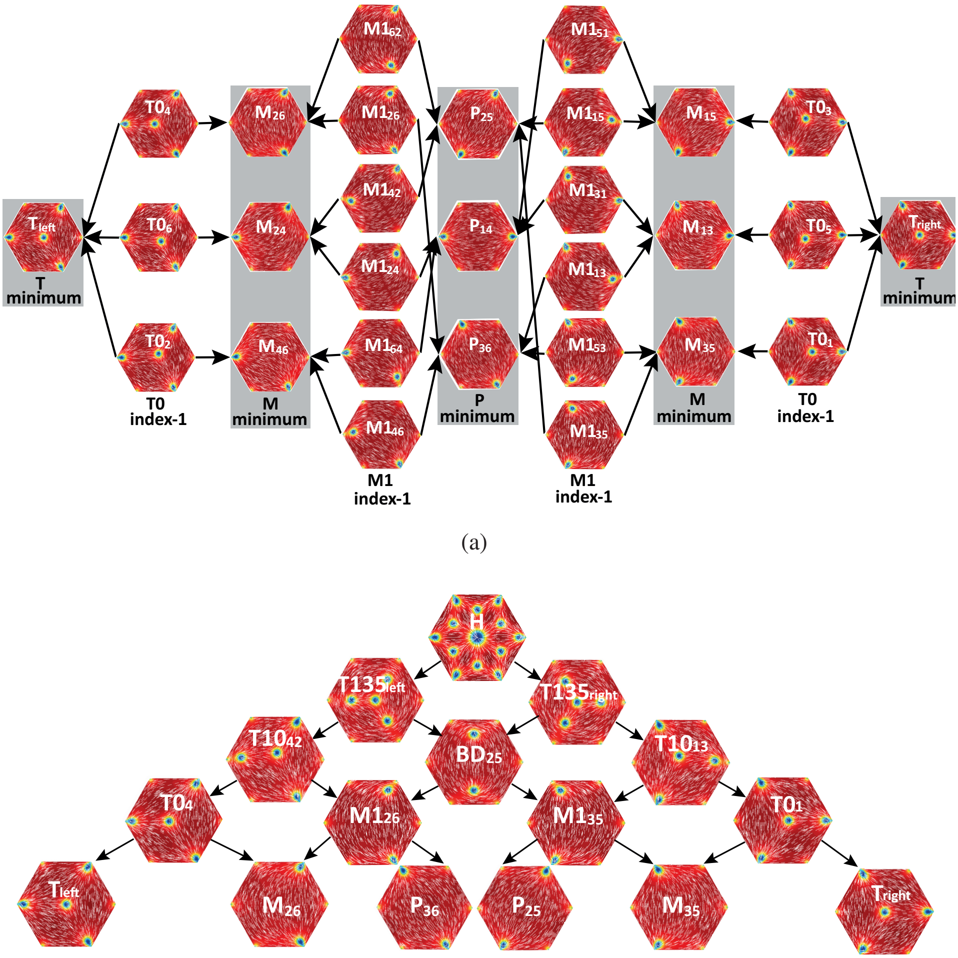

(a)

(b)

Figure 6.5. (Credit: Han *et al.* 2020*b*.) (a) Transition pathways between stable states including two T, six M and three P solutions at $\lambda^2 = 600$. (b) Solution landscape starting from the H solution. All local minima such as T_{left}, P_{36}, M_{26}, M_{35}, P_{25} and T_{right} are connected by the index-8 H solution.

A further innovative aspect of the solution landscape of NLCs is to provide rich information on dynamical pathways, which include transition pathways with a single transition state, multiple transition states, and dynamical pathways mediated by high-index saddle points. For example, in Figure 6.5(a), the transition pathway between T_{left} and M_{26} is connected by single transition state $\mathrm{T0}_4$. On the other hand, one transition pathway between P_{25} and P_{36} can be

$$\mathrm{P}_{25} \leftrightarrow \mathrm{M1}_{35} \leftrightarrow \mathrm{M}_{35} \leftrightarrow \mathrm{M1}_{53} \leftrightarrow \mathrm{P}_{36},$$

connected by two transition states $\mathrm{M1}_{35}$ and $\mathrm{M1}_{53}$. The 'longest' transition pathway appears to be the pathway between the two T solutions, T_{left} and T_{right}, even though T_{left} and T_{right} are two symmetric solutions related by a 60° rotation. One switching pathway between T_{left} and T_{right} can now be achieved by

$$\mathrm{T}_{left} \leftrightarrow \mathrm{T0}_4 \leftrightarrow \mathrm{M}_{26} \leftrightarrow \mathrm{M1}_{62} \leftrightarrow \mathrm{P}_{25} \leftrightarrow \mathrm{M1}_{15} \leftrightarrow \mathrm{M}_{15} \leftrightarrow \mathrm{T0}_3 \leftrightarrow \mathrm{T}_{right},$$

which indicates that the transition between two energetically close but configurationally far T solutions has to overcome four energy barriers.

Figure 6.5(b) shows how the different P, M and T solutions are connected by high-index saddle points. For example, the index-1 M1 connects stable M and P, and the index-1 T0 connects stable M and T. In contrast, two M or two P are connected by the index-2 BD. Furthermore, T_{left} and T_{right}, which are configurationally far away from each other, are connected by an index-8 H solution by the following HiSD:

$$\mathrm{T}_{left} \leftarrow \mathrm{T135}_{left} \leftarrow \mathrm{H} \rightarrow \mathrm{T135}_{right} \rightarrow \mathrm{T}_{right}.$$

The index-8 H solution is the stationary point in the intersection of the smallest closures on the energy landscape, which is able to connect every stable solution (two T, three P and six M solutions) through dynamical pathways in Figure 6.5(b). Han *et al.* (2020*b*) deduce that index-1 saddle points are efficient for connecting configurationally close stable solutions. For configurationally far stable states, they are generally connected by multiple transition states, or connected by a high-index saddle point.

7. Conclusion and future directions

LCs are fascinating examples of complex fluids that combine fluidity of fluids with the directionality of solids. During the past few decades, the study of LCs has grown tremendously due to widespread applications in the industry, such as display devices, photonic devices and biological sensors. Modelling, analysis and computation are indispensable tools for describing, understanding and predicting the physical phenomena related to LCs. The topics of LCs touch on a number of branches of physics, materials science and mathematics, creating problems of fundamental importance.

Theoretical studies of LCs are primarily concerned with how topology and geometry of the elements (macromolecules or anisotropic molecules) produce and affect the mesoscopic structure, and how the structure determines the properties of the materials. It is crucial to understand LC phenomena by building appropriate mathematical models and carrying out both theoretical analysis and numerical simulation. Scientific values of LCs include two major aspects.

Raising new mathematical problems. The study of LCs involves calculus of variations, PDEs, harmonic analysis and computational methods. For example, the Onsager model can be expressed as either a variation minimization problem, a nonlinear non-local integral equation or a PDE problem. In general, it is impossible to find all analytical solutions for such problems. This is because of the problem with special physical properties, which allows us to find all the solutions and prove that all solutions have axial symmetry. LCs are prone to defects, which correspond to mathematical singularities. The main reason is that the nature of such problems is a vector field. Mathematicians often use LCs to study singularities of harmonic maps. The **Q**-tensor theory is a regularization model for the vector model, involving mathematical problems such as eigenvalue degradation and multiscale analysis, which provides direction and guidance to relevant mathematical study. Furthermore, because of multiscale phenomena in complex fluids, it is desirable to study modelling and numerical methods in computational and applied mathematics.

Providing new methodologies. The choice of order parameter in the macroscopic model of LCs is key to understanding the connections between macroscopic theories and microscopic theories. For rod-like liquid crystals, the axially symmetric assumption is generally accepted by chemists, physicists and scientists in materials or mechanics. A strict mathematical proof can not only verify their intuition, but also achieve deep understanding of the mechanism of axial symmetry. Continuum NLC theories, which assume that macroscopic quantities of interest vary slowly on the molecular length scale, are typically defined in terms of a macroscopic order parameter and a free energy; the experimentally observable states correspond to energy minimizers. Mathematically, this reduces to analysing and numerically computing solutions of the associated Euler–Lagrange equations, which are a system of highly nonlinear and coupled partial differential equations. Recent years have seen a boom in analytical and numerical efforts to compute the solution landscapes of NLC systems.

Although tremendous progress has been achieved in both theoretical and numerical study of LCs over the past four decades, there are still many challenges in modelling and computation of LCs. Following the contents of this review, we list some of the challenges below.

Symmetry of equilibrium configurations. Symmetry is the central theme of LC studies. The axial symmetry of equilibrium solutions of Onsager's molecular energy plays a fundamental role in molecular kinetic theory. However, it is only proved for the Maier–Saupe potential. Proving analogous results for the Onsager potential – even for minimizers – is an important and difficult problem. For the Landau–de Gennes energy with isotropic elasticity, it is believed that the minimizing solutions corresponding to the hedgehog boundary condition in a three-dimensional ball are axially symmetric. Furthermore, all minimizers should be one of three types: radial hedgehog, ring disclination and split core. However, rigorous proofs are challenging. Similar problems can be raised for the 2D point defects, which are closely related to the disclinations in three-dimensional space. If the anisotropic elastic constants are not zero, the corresponding problems are more complicated and difficult. These problems are related to fine structures of the point defects and disclinations, which are of fundamental importance.

Analysis of the isotropic–nematic interface. The study of the profiles and structure of the two-phase interface is physically important and mathematically challenging. One of the simplest models is the energy functional with the order parameter being a scalar function, which has been widely studied during the past two decades. When the order parameter is a high-dimensional vector, the problem is much more difficult. Lin, Pan and Wang (2012) studied the asymptotic behaviour of minimizers for the high-dimensional problem. The phase transition interface between isotropic and nematic phases is even harder because it is not only high-dimensional but also involves anisotropic elasticity. The problem on the one-dimensional line has been studied in some special cases (Park, Wang, Zhang and Zhang 2017, Chen, Zhang and Zhang 2018). The general problem, such as properties of profiles, the boundary condition on the interface and the limit behaviour of the equilibrium configuration, needs further study.

Well-posedness, blow-up and long-time behaviour of solutions to different dynamical models. Although there are many works on the well-posedness of solutions to various dynamical models, some basic questions are still unsolved, for example the global existence of weak solutions to the three-dimensional Ericksen–Leslie system and the inhomogeneous Doi–Onsager equation. Constructing solutions that blow up at finite time are also of interest. In addition, the long-time dynamics would be complicated, even under a given flow field. For example, there are many periodic solutions, called kayaking, wagging, logrolling, *etc.* It would be interesting to rigorously prove existence of these solutions.

Dynamics of point defects, disclinations and two-phase interfaces. In the Ginzburg–Landau theory for superconductors, dynamics of vortices and filaments have been well understood. The method cannot be directly applied to similar problems in LCs, such as the uniaxial limit of the dynamical $\mathbf{Q}$-tensor system, due to some essential differences. First, the elasticity is usually anisotropic, which will cause complex phenomena such as backflows. Second, the $\mathbf{Q}$-tensor can become biaxial, and the minimizing manifold is isomorphic to the projective space $\mathbb{RP}^2$ which has topological properties different from $\mathbb{S}^2$ and $\mathbb{S}^1$. Third, the hydrodynamics will play an important role. The singularity set of the limit system can be isolated points, lines and surfaces, with co-dimension three, two and one respectively. The evolution of the singularity set is an interesting and challenging problem which may require deeper understanding of the profiles near the singularity set.

Relationship between different dynamical models. The rigorous derivation of the Ericksen–Leslie theory from the Doi–Onsager theory is only established for smooth solutions with isotropic elasticity ($k_1 = k_2 = k_3$). To generalize it to the anisotropic elasticity case would be an important problem. Moreover, as the defect solutions can only be described by weak solutions in the vector theory, justification of convergence for weak solutions is an important problem. However, analogous results for weak solutions are very few.

Solution landscapes of confined liquid crystals. NLCs in confinement typically exhibit multiple stable and unstable states, which correspond to stationary solutions of a free energy. A solution landscape of confined NLCs, a hierarchy of connected solutions, is able to provide rich and insightful information on the physical properties of these multisolution problems. The HiSD is an efficient numerical algorithm for computing saddle point solutions for LC systems, and has been successfully used to construct the solution landscapes of NLCs confined in a square and a hexagon. Solution landscapes reveal not only transition pathways between stable solutions connected by index-1 saddle points but also innovative dynamical pathways mediated by high-index saddle points. Several challenging analytical and numerical questions remain for the solution landscape, for instance the completion of the solution landscape. Can we obtain bounds for the Morse index of the parent state in the solution landscape? How do we estimate the number of the stationary solutions of a given free energy? Building a theoretical framework for the solution landscape is a big challenge as well as a great opportunity for applied mathematicians.

Finally, we would like to emphasize again that we only focus on the simplest NLC systems in the context of this review, and have barely touched upon the other LC systems. There is a crucial need for exhaustive theoretical and numerical studies of complex and unconventional LC systems, to complement thriving experimental work. Below we list a few examples in which the field is relatively open, the energies are more complex, and the solutions are less regular with new analytical and numerical challenges.

Phase transitions in multiphase liquid crystal systems. Recent experiments show NLC-cholesteric (by adding chiral particles) and NLC-smectic (by lowering the temperature) phase transitions in LC systems (Siavashpouri *et al.* 2017). Compared with single-phase LCs, these heterogeneous systems are inherently more complex with multiple competing NLCs, cholesteric/smectic and mixed solutions, novel solutions with phase separation, and interactions between phases (Gottarelli *et al.* 1983). Multiple phases in the heterogeneous system need to be analysed under the unified theory framework. For instance, the complex NLC-smectic or NLC-cholesteric systems can be analysed in terms of LdG-type energies with multiple-order parameters for coupled systems with smectic/cholesteric terms. The heterogeneous systems can also be analysed by molecular models. On the other hand, the accurate structures (*e.g.* interfaces between phases) and complex defects have multiscale properties. The field is relatively open with new analytical and numerical challenges.

Ferroelectric and ferromagnetic liquid crystals. LCs are sensitive to external fields such as electric fields and magnetic fields (Mertelj, Lisjak, Drofenik and Čopič 2013, Mertelj and Lisjak 2017, Chen *et al.* 2020, Bisht, Wang, Banerjee and Majumdar 2020). Due to the photoelectric effect, LCs are applied in display devices and have revolutionized the display industry. Besides normal LCs, a new ferroelectric LC has attracted extensive attention. Ferroelectric LC materials have the characteristics of high response speed, high contrast, high resolution and large capacity information display. They have good application prospects in the fields of display, optical interconnections and optical information processing. One future direction would be to develop suitable LC models from molecular models to macroscopic models to study the photoelectric effect of ferroelectric LCs and the design of voltage waveforms.

Active liquid crystal systems. The non-equilibrium phenomena studied in active matter systems are widespread in nature, playing an especially important role in biological phenomena (Marchetti *et al.* 2013, Keber *et al.* 2014, Prost, Jülicher and Joanny 2015). The active matter system is a typical non-equilibrium system, which is composed of a large number of active particles. These particles obtain energy for self-propulsion by converting other forms of energy into kinetic energy (Zhou, Sokolov, Lavrentovich and Aranson 2014). Due to the interaction between particles and particles, and particles and media, the entire system can exhibit extremely rich dynamic phenomena macroscopically. The active LC system is a paradigm of active systems for biologically inspired complex fluids with orientational alignment. In active LCs, the rod-like constituents endow the fluid they are immersed in with active stresses (*e.g.* in cells the motility arises from the interaction of myosin and actin). Their dynamic properties, phase transition process and external field responses are worthy of study and exploration.

Acknowledgement

We would like to thank Dr Yucen Han, Dr Yiwei Wang and Mr Jianyuan Yin for providing great assistance. We also thank Professors Yucheng Hu, Yuning Liu, Apala Majumdar, Jinhae Park and Zhifei Zhang for fruitful discussions and helpful comments. Wei Wang was partially supported by the National Natural Science Foundation of China no. 11922118 and 11931010. Lei Zhang was partially supported by the National Natural Science Foundation of China no. 12050002, 11861130351 and the Royal Society Newton Advanced Fellowship, in partnership with Apala Majumdar from Strathclyde. Pingwen Zhang was partially supported by the National Natural Science Foundation of China no. 21790340, 11421101.

We acknowledge the permission from the American Physical Society, Elsevier, Global Science Press and IOP Publishing to reproduce the figures used in this article.

Appendix

A.1. Elementary identities for the high-order moments

Let

$$\mathbf{Q}_2[f] = \left\langle \mathbf{mm} - \frac{1}{3}\mathbf{I} \right\rangle_f,$$

and define $\mathbf{Q}_4[f]$ as follows:

$$\begin{aligned} Q_{4\alpha\beta\gamma\mu}[f] = \Big\langle & m_\alpha m_\beta m_\gamma m_\mu - \frac{1}{7}(m_\alpha m_\beta \delta_{\gamma\mu} + m_\gamma m_\mu \delta_{\alpha\beta} + m_\alpha m_\gamma \delta_{\beta\mu} + m_\beta m_\mu \delta_{\alpha\gamma} \\ & + m_\alpha m_\mu \delta_{\beta\gamma} + m_\beta m_\gamma \delta_{\alpha\mu}) + \frac{1}{35}(\delta_{\alpha\beta}\delta_{\gamma\mu} + \delta_{\alpha\gamma}\delta_{\beta\mu} + \delta_{\alpha\mu}\delta_{\beta\gamma}) \Big\rangle_f. \end{aligned} \tag{A.1}$$

Let $P_k(x)$ be the kth Legendre polynomial and

$$S_2 = \langle P_2(\mathbf{m} \cdot \mathbf{n}) \rangle_{h_\mathbf{n}}, \quad S_4 = \langle P_4(\mathbf{m} \cdot \mathbf{n}) \rangle_{h_\mathbf{n}}, \tag{A.2}$$

which only depend on α. First we have the following lemma.

Lemma A.1.

$$\mathbf{Q}_2[h_\mathbf{n}] = S_2\left(\mathbf{nn} - \frac{1}{3}\right),$$

$$\begin{aligned} Q_{4\alpha\beta\gamma\mu}[h_\mathbf{n}] = S_4 \Big(& n_\alpha n_\beta n_\gamma n_\mu - \frac{1}{7}(n_\alpha n_\beta \delta_{\gamma\mu} + n_\gamma n_\mu \delta_{\alpha\beta} + n_\alpha n_\gamma \delta_{\beta\mu} \\ & + n_\beta n_\mu \delta_{\alpha\gamma} + n_\alpha n_\mu \delta_{\beta\gamma} + n_\beta n_\gamma \delta_{\alpha\mu}) + \frac{1}{35}(\delta_{\alpha\beta}\delta_{\gamma\mu} + \delta_{\alpha\gamma}\delta_{\beta\mu} + \delta_{\alpha\mu}\delta_{\beta\gamma}) \Big). \end{aligned}$$

Corollary A.2. Let $\mathbf{M} = \langle \mathbf{mm} \rangle_{h_\mathbf{n}}$, $\mathbf{M}^{(4)} = \langle \mathbf{mmmm} \rangle_{h_\mathbf{n}}$. We have

$$\mathbf{M} = S_2 \mathbf{nn} + \frac{1 - S_2}{3}\mathbf{I}, \tag{A.3}$$

$$\begin{aligned} M^{(4)}_{\alpha\beta\gamma\mu} = {} & S_4 n_\alpha n_\beta n_\gamma n_\mu + \frac{S_2 - S_4}{7}(n_\alpha n_\beta \delta_{\gamma\mu} + n_\gamma n_\mu \delta_{\alpha\beta} + n_\alpha n_\gamma \delta_{\beta\mu} + n_\beta n_\mu \delta_{\alpha\gamma} \\ & + n_\alpha n_\mu \delta_{\beta\gamma} + n_\beta n_\gamma \delta_{\alpha\mu}) + \left(\frac{S_4}{35} - \frac{2S_2}{21} + \frac{1}{15}\right)(\delta_{\alpha\beta}\delta_{\gamma\mu} + \delta_{\alpha\gamma}\delta_{\beta\mu} + \delta_{\alpha\mu}\delta_{\beta\gamma}). \end{aligned} \tag{A.4}$$

A.2. Some identities used in Section 3.4.3

For any constant vector $\mathbf{u}, \mathbf{w} \in \mathbb{R}^3$, and a vector field $\mathbf{v}(\mathbf{m})$ defined on $\mathbb{S}^2$,

$$\begin{aligned}
&\mathbf{u} \cdot \left(\int_{\mathbb{S}^2} \left(\mathbf{mm} - \frac{1}{3}\mathbf{I} \right) \mathcal{R} \cdot (f\mathbf{v}) \,\mathrm{d}\mathbf{m} \right) \cdot \mathbf{w} \\
&\quad = \int_{\mathbb{S}^2} \left((\mathbf{m} \cdot \mathbf{u})(\mathbf{m} \cdot \mathbf{w}) - \frac{1}{3}\mathbf{u} \cdot \mathbf{w} \right) \mathcal{R} \cdot (f\mathbf{v}) \,\mathrm{d}\mathbf{m} \\
&\quad = -\int_{\mathbb{S}^2} \mathcal{R}((\mathbf{m} \cdot \mathbf{u})(\mathbf{m} \cdot \mathbf{w})) \cdot (f\mathbf{v}) \,\mathrm{d}\mathbf{m} \\
&\quad = -\int_{\mathbb{S}^2} \mathbf{m} \times \mathbf{u} \cdot \mathbf{v}(\mathbf{m} \cdot \mathbf{w}) f + (\mathbf{m} \cdot \mathbf{u})(\mathbf{m} \times \mathbf{w}) \cdot \mathbf{v} f \,\mathrm{d}\mathbf{m} \\
&\quad = \mathbf{u} \cdot \langle \mathbf{m} \times \mathbf{vm} + \mathbf{mm} \times \mathbf{v} \rangle \cdot \mathbf{w}.
\end{aligned}$$

Hence we have

$$\int_{\mathbb{S}^2} \left(\mathbf{mm} - \frac{1}{3}\mathbf{I} \right) \mathcal{R} \cdot (f\mathbf{v}) \,\mathrm{d}\mathbf{m} = \langle \mathbf{m} \times \mathbf{vm} + \mathbf{mm} \times \mathbf{v} \rangle. \tag{A.5}$$

Let $\mathbf{v} = \mathcal{R}\mu$. We then have

$$\int_{\mathbb{S}^2} \left(\mathbf{mm} - \frac{1}{3}\mathbf{I} \right) \mathcal{R} \cdot (f\mathcal{R}\mu) \,\mathrm{d}\mathbf{m} = \langle \mathbf{m} \times \mathcal{R}\mu\mathbf{m} + \mathbf{mm} \times \mathcal{R}\mu \rangle. \tag{A.6}$$

Let $\mathbf{v} = \mathbf{m} \times \kappa \cdot \mathbf{m}$. We then have

$$\begin{aligned}
&\int_{\mathbb{S}^2} \left(\mathbf{mm} - \frac{1}{3}\mathbf{I} \right) \mathcal{R} \cdot (f\mathbf{m} \times \kappa \cdot \mathbf{m}) \,\mathrm{d}\mathbf{m} \\
&\quad = \langle \mathbf{m} \times (\mathbf{m} \times \kappa \cdot \mathbf{m})\mathbf{m} + \mathbf{mm} \times (\mathbf{m} \times \kappa \cdot \mathbf{m}) \rangle \\
&\quad = \langle 2(\mathbf{m} \cdot \kappa \cdot \mathbf{m})\mathbf{mm} - (\kappa \cdot \mathbf{m})\mathbf{m} - \mathbf{m}(\kappa \cdot \mathbf{m}) \rangle \\
&\quad = 2\mathbf{D} : \langle \mathbf{mmmm} \rangle - \mathbf{D} \cdot \langle \mathbf{mm} \rangle + \mathbf{\Omega} \cdot \langle \mathbf{mm} \rangle - \langle \mathbf{mm} \rangle \cdot (\mathbf{D} + \mathbf{\Omega}).
\end{aligned} \tag{A.7}$$

Lemma A.3. For any antisymmetric constant matrix $\mathbf{\Omega}$, we have

$$\begin{aligned}
\mathcal{R} \cdot (\mathbf{m} \times (\mathbf{\Omega} \cdot \mathbf{m}) f_0) &= (\mathbf{n} \times (\mathbf{\Omega} \cdot \mathbf{n})) \cdot \mathcal{R} f_0, \\
\mathcal{R} \cdot (\mathbf{m} \times (\mathbf{D} \cdot \mathbf{m}) f_0) &= \frac{1}{2}\mathcal{R} \cdot (f_0 \mathcal{R}(\mathbf{mm} : \mathbf{D})).
\end{aligned}$$

Proof. The lemma is a direct consequence of the following identities:

$$\begin{aligned}
&\mathcal{R} \cdot (\mathbf{m} \times (\mathbf{\Omega} \cdot \mathbf{m})) = \mathcal{R}_i(\epsilon^{ijk} m_j \Omega_{kl} m_l) = (\mathbf{I} - 3\mathbf{mm}) : \mathbf{\Omega} = 0, \\
&(\mathbf{m} \times (\mathbf{\Omega} \cdot \mathbf{m})) \cdot \mathcal{R} f_0 = (\mathbf{m} \times (\mathbf{\Omega} \cdot \mathbf{m})) \cdot (\mathbf{m} \times \mathbf{n}) f_0' \\
&\qquad = (\mathbf{n} \times (\mathbf{\Omega} \cdot \mathbf{n})) \cdot (\mathbf{m} \times \mathbf{n}) f_0' = (\mathbf{n} \times (\mathbf{\Omega} \cdot \mathbf{n})) \cdot \mathcal{R} f_0, \\
&\mathcal{R}(\mathbf{mm} : \mathbf{D}) = 2\mathbf{m} \times (\mathbf{D} \cdot \mathbf{m}).
\end{aligned}$$

This completes the proof. ☐

References

H. Abels, G. Dolzmann and Y. Liu (2014), Well-posedness of a fully coupled Navier–Stokes/Q-tensor system with inhomogeneous boundary data, *SIAM J. Math. Anal.* **46**, 3050–3077.

J. H. Adler, T. J. Atherton, D. B. Emerson and S. P. MacLachlan (2015), An energy-minimization finite-element approach for the Frank–Oseen model of nematic liquid crystals, *SIAM J. Numer. Anal.* **53**, 2226–2254.

J. H. Adler, D. B. Emerson, S. P. MacLachlan and T. A. Manteuffel (2016), Constrained optimization for liquid crystal equilibria, *SIAM J. Sci. Comput.* **38**, B50–B76.

F. Alouges (1997), A new algorithm for computing liquid crystal stable configurations: The harmonic mapping case, *SIAM J. Numer. Anal.* **34**, 1708–1726.

L. Ambrosio (1990), Existence of minimal energy configurations of nematic liquid crystals with variable degree of orientation, *Manuscripta Math.* **68**, 215–228.

L. Angelani, R. Di Leonardo, G. Ruocco, A. Scala and F. Sciortino (2000), Saddles in the energy landscape probed by supercooled liquids, *Phys. Rev. Lett.* **85**, 5356–5359.

S. Badia, F. Guillén-González and J. V. Gutiérrez-Santacreu (2011*a*), Finite element approximation of nematic liquid crystal flows using a saddle-point structure, *J. Comput. Phys.* **230**, 1686–1706.

S. Badia, F. Guillén-Gónzalez and J. V. Gutiérrez-Santacreu (2011*b*), An overview on numerical analyses of nematic liquid crystal flows, *Arch. Comput. Methods Eng.* **18**, 285.

I. Bajc, F. Hecht and S. Žumer (2016), A mesh adaptivity scheme on the Landau–de Gennes functional minimization case in 3D, and its driving efficiency, *J. Comput. Phys.* **321**, 981–996.

J. M. Ball (2017), Liquid crystals and their defects, in *Mathematical Thermodynamics of Complex Fluids*, Vol. 2200 of Lecture Notes in Mathematics, Springer, pp. 1–46.

J. M. Ball (2020), Axisymmetry of critical points for the Onsager functional. Available at arXiv:2008.04009.

J. M. Ball and A. Majumdar (2010), Nematic liquid crystals: From Maier–Saupe to a continuum theory, *Molecular Cryst. Liquid Cryst.* **525**, 1–11.

J. M. Ball and A. Zarnescu (2008), Orientable and non-orientable line field models for uniaxial nematic liquid crystals, *Molecular Cryst. Liquid Cryst.* **495**, 221–573.

J. M. Ball and A. Zarnescu (2011), Orientability and energy minimization in liquid crystal models, *Arch. Ration. Mech. Anal.* **202**, 493–535.

P. Bauman, J. Park and D. Phillips (2012), Analysis of nematic liquid crystals with disclination lines, *Arch. Ration. Mech. Anal.* **205**, 795–826.

R. Becker, X. Feng and A. Prohl (2008), Finite element approximations of the Ericksen–Leslie model for nematic liquid crystal flow, *SIAM J. Numer. Anal.* **46**, 1704–1731.

A. N. Beris and B. J. Edwards (1994), *Thermodynamics of Flowing Systems: With Internal Microstructure*, Oxford Engineering Science Series, The Clarendon Press, Oxford University Press.

K. Bisht, Y. Wang, V. Banerjee and A. Majumdar (2020), Tailored morphologies in two-dimensional ferronematic wells, *Phys. Rev. E* **101**, 022706.

J. P. Borthagaray, R. H. Nochetto and S. W. Walker (2020), A structure-preserving FEM for the uniaxially constrained Q-tensor model of nematic liquid crystals, *Numer. Math.* **145**, 837–881.

Z. Brada, S. Kralj, M. Svetec and S. Zumer (2003), Annihilation of nematic point defects: Postcollision scenarios, *Phys. Rev. E* **67**, 050702.

H. Brezis, J.-M. Coron and E. H. Lieb (1986), Harmonic maps with defects, *Commun. Math. Phys.* **107**, 649–705.

Y. Cai and W. Wang (2020), Global well-posedness for the three dimensional simplified inertial Ericksen–Leslie systems near equilibrium, *J. Funct. Anal.* **279**, 108521.

Y. Cai, J. Shen and X. Xu (2017*a*), A stable scheme and its convergence analysis for a 2D dynamic Q-tensor model of nematic liquid crystals, *Math. Models Methods Appl. Sci.* **27**, 1459–1488.

Y. Cai, P. Zhang and A.-C. Shi (2017*b*), Liquid crystalline bilayers self-assembled from rod–coil diblock copolymers, *Soft Matter* **13**, 4607–4615.

G. Canevari (2015), Biaxiality in the asymptotic analysis of a 2D Landau–de Gennes model for liquid crystals, *ESAIM Control Optim. Calc. Var.* **21**, 101–137.

G. Canevari (2017), Line defects in the small elastic constant limit of a three-dimensional Landau–de Gennes model, *Arch. Ration. Mech. Anal.* **223**, 591–676.

G. Canevari, J. Harris, A. Majumdar and Y. W. Wang (2020), The well order reconstruction solution for three-dimensional wells, in the Landau–de Gennes theory, *Int. J. Nonlinear Mech.* **119**, 103342.

G. Canevari, A. Majumdar and A. Spicer (2017), Order reconstruction for nematics on squares and hexagons: A Landau–de Gennes study, *SIAM J. Appl. Math.* **77**, 267–293.

C. J. Cerjan and W. H. Miller (1981), On finding transition states, *J. Chem. Phys.* **75**, 2800–2806.

C. V. Chaubal and L. G. Leal (1998), A closure approximation for liquid-crystalline polymer models based on parametric density estimation, *J. Rheology* **42**, 177–201.

J. Chen, P. Zhang and Z. Zhang (2018), Local minimizer and De Giorgi's type conjecture for the isotropic–nematic interface problem, *Calc. Var. Partial Differential Equations* **57**, 1–19.

R. Chen, W. Bao and H. Zhang (2016), The kinematic effects of the defects in liquid crystal dynamics, *Commun. Comput. Phys.* **20**, 234–249.

R. Chen, X. Yang and H. Zhang (2017), Second order, linear, and unconditionally energy stable schemes for a hydrodynamic model of smectic-A liquid crystals, *SIAM J. Sci. Comput.* **39**, A2808–A2833.

W. Chen, C. Li and G. Wang (2010), On the stationary solutions of the 2D Doi–Onsager model, *Nonlinear Anal.* **73**, 2410–2425.

X. Chen, E. Korblova, D. Dong, X. Wei, R. Shao, L. Radzihovsky, M. A. Glaser, J. E. Maclennan, D. Bedrov, D. M. Walba and N. A. Clark (2020), First-principles experimental demonstration of ferroelectricity in a thermotropic nematic liquid crystal: Polar domains and striking electro-optics, *Proc. Nat. Acad. Sci.* **117**, 14021–14031.

R. Cohen and M. Taylor (1990), Weak stability of the map $x/|x|$ for liquid crystal functionals, *Commun. Partial Differential Equations* **15**, 675–692.

R. Cohen, R. Hardt, D. Kinderlehrer, S.-Y. Lin and M. Luskin (1987), Minimum energy configurations for liquid crystals: Computational results, in *Theory and Applications of Liquid Crystals*, Vol. 5 of The IMA Volumes in Mathematics and Its Applications, Springer, pp. 99–121.

G. M. Crippen and H. A. Scheraga (1971), Minimization of polypeptide energy XI: The method of gentlest ascent, *Arch. Biochem. Biophys.* **144**, 462–466.

A. Darmon, M. Benzaquen, S. Čopar, O. Dauchot and T. Lopez-Leon (2016), Topological defects in cholesteric liquid crystal shells, *Soft Matter* **12**, 9280–9288.

T. A. Davis and E. C. Gartland Jr (1998), Finite element analysis of the Landau–de Gennes minimization problem for liquid crystals, *SIAM J. Numer. Anal.* **35**, 336–362.

P. G. de Gennes and J. Prost (1993), *The Physics of Liquid Crystals*, Vol. 83 of International Series of Monographs on Physics, Oxford University Press.

G. de Luca and A. D. Rey (2007), Point and ring defects in nematics under capillary confinement, *J. Chem. Phys.* **127**, 104902.

C. Denniston, E. Orlandini and J. M. Yeomans (2001), Lattice Boltzmann simulations of liquid crystal hydrodynamics, *Phys. Rev. E* **63**, 056702.

M. Doi (1981), Molecular dynamics and rheological properties of concentrated solutions of rodlike polymers in isotropic and liquid crystalline phases, *J. Polymer Sci. Polymer Phys. Edn* **19**, 229–243.

M. Doi and S. F. Edwards (1988), *The Theory of Polymer Dynamics*, Vol. 73 of International Series of Monographs on Physics, Oxford University Press, Oxford.

M. Doi, J. Zhou, Y. Di and X. Xu (2019), Application of the Onsager–Machlup integral in solving dynamic equations in nonequilibrium systems, *Phys. Rev. E* **99**, 063303.

J. P. K. Doye and D. J. Wales (2002), Saddle points and dynamics of Lennard-Jones clusters, solids, and supercooled liquids, *J. Chem. Phys.* **116**, 3777–3788.

Q. Du and X. Feng (2020), The phase field method for geometric moving interfaces and their numerical approximations, in *Geometric Partial Differential Equations, Part I*, Vol. 21 of Handbook of Numerical Analysis, Elsevier, pp. 425–508.

Q. Du and L. Zhang (2009), A constrained string method and its numerical analysis, *Commun. Math. Sci.* **7**, 1039–1051.

Q. Du, B. Guo and J. Shen (2001), Fourier spectral approximation to a dissipative system modeling the flow of liquid crystals, *SIAM J. Numer. Anal.* **39**, 735–762.

W. E (1997), Nonlinear continuum theory of smectic-A liquid crystals, *Arch. Ration. Mech. Anal.* **137**, 159–175.

W. E and P. Zhang (2006), A molecular kinetic theory of inhomogeneous liquid crystal flow and the small Deborah number limit, *Methods Appl. Anal.* **13**, 181–198.

W. E and X. Zhou (2011), The gentlest ascent dynamics, *Nonlinearity* **24**, 1831.

W. E, W. Ren and E. Vanden-Eijnden (2002), String method for the study of rare events, *Phys. Rev. B* **66**, 052301.

W. E, W. Ren and E. Vanden-Eijnden (2007), Simplified and improved string method for computing the minimum energy paths in barrier-crossing events, *J. Chem. Phys.* **126**, 164103.

C. M. Elliott and A. M. Stuart (1993), The global dynamics of discrete semilinear parabolic equations, *SIAM J. Numer. Anal.* **30**, 1622–1663.

J. L. Ericksen (1961), Conservation laws for liquid crystals, *Trans. Soc. Rheology* **5**, 23–34.

J. L. Ericksen (1990), Liquid crystals with variable degree of orientation, *Arch. Ration. Mech. Anal.* **113**, 97–120.

D. J. Eyre (1998), Unconditionally gradient stable time marching the Cahn–Hilliard equation, in *Symposia BB: Computational & Mathematical Models of Microstructural Evolution*, Vol. 529 of Materials Research Society Symposium Proceedings, Materials Research Society, pp. 39–46.

P. E. Farrell, Á. Birkisson and S. W. Funke (2015), Deflation techniques for finding distinct solutions of nonlinear partial differential equations, *SIAM J. Sci. Statist. Comput.* **37**, A2026–A2045.

I. Fatkullin and V. Slastikov (2005), Critical points of the Onsager functional on a sphere, *Nonlinearity* **18**, 2565.

J. Feng, C. Chaubal and L. G. Leal (1998), Closure approximations for the Doi theory: Which to use in simulating complex flows of liquid-crystalline polymers?, *J. Rheology* **42**, 1095–1119.

J. J. Feng, G. Sgalari and L. G. Leal (2000), A theory for flowing nematic polymers with orientational distortion, *J. Rheology* **44**, 1085–1101.

X. Feng and A. Prohl (2004), Analysis of a fully discrete finite element method for the phase field model and approximation of its sharp interface limits, *Math. Comp.* **73**, 541–567.

G. Foffano, J. S. Lintuvuori, A. Tiribocchi and D. Marenduzzo (2014), The dynamics of colloidal intrusions in liquid crystals: A simulation perspective, *Liquid Cryst. Rev.* **2**, 1–27.

F. C. Frank (1958), I. Liquid crystals. On the theory of liquid crystals, *Discussions Faraday Soc.* **25**, 19–28.

G. Friedel (1922), Les états mésomorphes de la matière, *Ann. de Physique* **18**, 273.

J.-i. Fukuda, H. Stark, M. Yoneya and H. Yokoyama (2004), Interaction between two spherical particles in a nematic liquid crystal, *Phys. Rev. E* **69**, 041706.

J.-i. Fukuda, S. Žumer *et al.* (2010), Novel defect structures in a strongly confined liquid-crystalline blue phase, *Phys. Rev. Lett.* **104**, 017801.

E. C. Gartland Jr and S. Mkaddem (1999), Instability of radial hedgehog configurations in nematic liquid crystals under Landau–de Gennes free-energy models, *Phys. Rev. E* **59**, 563.

E. C. Gartland Jr, P. Palffy-Muhoray and R. S. Varga (1991), Numerical minimization of the Landau–de Gennes free energy: Defects in cylindrical capillaries, *Molecular Cryst. Liquid Cryst.* **199**, 429–452.

W. M. Gelbart and A. Ben-Shaul (1982), Molecular theory of curvature elasticity in nematic liquids, *J. Chem. Phys.* **77**, 916–933.

V. Girault and F. Guillén-González (2011), Mixed formulation, approximation and decoupling algorithm for a penalized nematic liquid crystals model, *Math. Comp.* **80**, 781–819.

D. Golovaty and J. A. Montero (2014), On minimizers of a Landau–de Gennes energy functional on planar domains, *Arch. Ration. Mech. Anal.* **213**, 447–490.

G. Gottarelli, M. Hibert, B. Samori, G. Solladie, G. P. Spada and R. Zimmermann (1983), Induction of the cholesteric mesophase in nematic liquid crystals: Mechanism and application to the determination of bridged biaryl configurations, *J. Amer. Chem. Soc.* **105**, 7318–7321.

F. Guillén-González and J. Koko (2015), A splitting in time scheme and augmented Lagrangian method for a nematic liquid crystal problem, *J. Sci. Comput.* **65**, 1129–1144.

F. M. Guillén-González and J. V. Gutiérrez-Santacreu (2013), A linear mixed finite element scheme for a nematic Ericksen–Leslie liquid crystal model, *ESAIM Math. Model. Numer. Anal.* **47**, 1433–1464.

Y. Guo, S. Afghah, J. Xiang, O. D. Lavrentovich, R. L. Selinger and Q.-H. Wei (2016), Cholesteric liquid crystals in rectangular microchannels: Skyrmions and stripes, *Soft Matter* **12**, 6312–6320.

J. K. Gupta, S. Sivakumar, F. Caruso and N. L. Abbott (2009), Size-dependent ordering of liquid crystals observed in polymeric capsules with micrometer and smaller diameters, *Angewandte Chemie International Edition* **48**, 1652–1655.

J. Han, Y. Luo, W. Wang, P. Zhang and Z. Zhang (2015), From microscopic theory to macroscopic theory: A systematic study on modeling for liquid crystals, *Arch. Ration. Mech. Anal.* **215**, 741–809.

Y. Han, Y. Hu, P. Zhang and L. Zhang (2019), Transition pathways between defect patterns in confined nematic liquid crystals, *J. Comput. Phys.* **396**, 1–11.

Y. Han, A. Majumdar and L. Zhang (2020*a*), A reduced study for nematic equilibria on two-dimensional polygons, *SIAM J. Appl. Math.* **80**, 1678–1703.

Y. Han, J. Yin, P. Zhang, A. Majumdar and L. Zhang (2020*b*), Solution landscape of a reduced Landau–de Gennes model on a hexagon. Available at arXiv:2003.07643.

P. Hänggi, P. Talkner and M. Borkovec (1990), Reaction-rate theory: Fifty years after Kramers, *Rev. Modern Phys.* **62**, 251.

W. R. Hao, J. D. Hauenstein, B. Hu and A. J. Sommese (2014), A bootstrapping approach for computing multiple solutions of differential equations, *J. Comput. Appl. Math.* **258**, 181–190.

R. Hardt, D. Kinderlehrer and F. Lin (1986), Existence and partial regularity of static liquid crystal configurations, *Commun. Math. Phys.* **105**, 547–570.

F. Hélein (1987), Minima de la fonctionnelle energie libre des cristaux liquides, *CR Acad. Sci. Paris* **305**, 565–568.

G. Henkelman and H. Jónsson (1999), A dimer method for finding saddle points on high dimensional potential surfaces using only first derivatives, *J. Chem. Phys.* **111**, 7010–7022.

S. Hess (1976), Fokker–Planck-equation approach to flow alignment in liquid crystals, *Z. Naturforschung A* **31**, 1034–1037.

M. Hieber and J. Prüss (2016), Modeling and analysis of the Ericksen–Leslie equations for nematic liquid crystal flows, in *Handbook of Mathematical Analysis in Mechanics of Viscous Fluids* (Y. Giga and A. Novotný, eds), Springer, pp. 1075–1134.

M. Hieber, M. Nesensohn, J. Prüss and K. Schade (2016), Dynamics of nematic liquid crystal flows: The quasilinear approach, *Ann. Inst. H. Poincaré Anal. Non Linéaire* **33**, 397–408.

E. J. Hinch and L. G. Leal (1976), Constitutive equations in suspension mechanics, part 2: Approximate forms for a suspension of rigid particles affected by Brownian rotations, *J. Fluid Mech.* **76**, 187–208.

M.-C. Hong (2011), Global existence of solutions of the simplified Ericksen–Leslie system in dimension two, *Calc. Var. Partial Differential Equations* **40**, 15–36.

M.-C. Hong and Z. Xin (2012), Global existence of solutions of the liquid crystal flow for the Oseen–Frank model in $\mathbb{R}^2$, *Adv. Math.* **231**, 1364–1400.

Y. Hu, Y. Qu and P. Zhang (2016), On the disclination lines of nematic liquid crystals, *Commun. Comput. Phys.* **19**, 354–379.

J. Huang and S. Ding (2015), Global well-posedness for the dynamical Q-tensor model of liquid crystals, *Sci. China Math.* **58**, 1349–1366.

J. Huang, F. Lin and C. Wang (2014), Regularity and existence of global solutions to the Ericksen–Leslie system in $\mathbb{R}^2$, *Commun. Math. Phys.* **331**, 805–850.

T. Huang, F. Lin, C. Liu and C. Wang (2016), Finite time singularity of the nematic liquid crystal flow in dimension three, *Arch. Ration. Mech. Anal.* **221**, 1223–1254.

R. Ignat, L. Nguyen, V. Slastikov and A. Zarnescu (2015), Stability of the melting hedgehog in the Landau–de Gennes theory of nematic liquid crystals, *Arch. Ration. Mech. Anal.* **215**, 633–673.

G. Ji, H. Yu and P. Zhang (2008), A kinetic-hydrodynamic simulation of liquid crystalline polymers under plane shear flow: 1 + 2 dimensional case, *Commun. Comput. Phys.* **4**, 1194–1215.

N. Jiang and Y.-L. Luo (2019), On well-posedness of Ericksen–Leslie's hyperbolic incompressible liquid crystal model, *SIAM J. Math. Anal.* **51**, 403–434.

H. Jónsson, G. Mills and K. W. Jacobsen (1998), Nudged elastic band method for finding minimum energy paths of transitions, in *Classical and Quantum Dynamics in Condensed Phase Simulations* (B. J. Berne, G. Ciccotti and D. F. Coker, eds), World Scientific, pp. 385–404.

F. C. Keber, E. Loiseau, T. Sanchez, S. J. DeCamp, L. Giomi, M. J. Bowick, M. C. Marchetti, Z. Dogic and A. R. Bausch (2014), Topology and dynamics of active nematic vesicles, *Science* **345**, 1135–1139.

D. Kinderlehrer, N. Walkington and B. Ou (1993), The elementary defects of the Oseen–Frank energy for a liquid crystal. Research report no. 93-NA-002, Carnegie Mellon University.

M. Kléman (1989), Defects in liquid crystals, *Rep. Progr. Phys.* **52**, 555.

A. V. Knyazev (2001), Toward the optimal preconditioned eigensolver: Locally optimal block preconditioned conjugate gradient method, *SIAM J. Sci. Comput.* **23**, 517–541.

S. Kralj and A. Majumdar (2014), Order reconstruction patterns in nematic liquid crystal wells, *Proc. Roy. Soc. A* **470**, 20140276.

S. Kralj, E. G. Virga and S. Žumer (1999), Biaxial torus around nematic point defects, *Phys. Rev. E* **60**, 1858.

H. Kusumaatmaja and A. Majumdar (2015), Free energy pathways of a multistable liquid crystal device, *Soft Matter* **11**, 4809–4817.

N. Kuzuu and M. Doi (1983), Constitutive equation for nematic liquid crystals under weak velocity gradient derived from a molecular kinetic equation, *J. Phys. Soc. Japan* **52**, 3486–3494.

C.-C. Lai, F. Lin, C. Wang, J. Wei and Y. Zhou (2019), Finite time blow-up for the nematic liquid crystal flow in dimension two. Available at arXiv:1908.10955.

X. Lamy (2013), Some properties of the nematic radial hedgehog in the Landau–de Gennes theory, *J. Math. Anal. Appl.* **397**, 586–594.

X. Lamy (2015), Uniaxial symmetry in nematic liquid crystals, *Ann. Inst. H. Poincaré Anal. Non Linéaire* **32**, 1125–1144.

F. M. Leslie (1968), Some constitutive equations for liquid crystals, *Arch. Ration. Mech. Anal.* **28**, 265–283.

F. M. Leslie (1979), Theory of flow phenomena in liquid crystals, *Adv. Liquid Cryst.* **4**, 1–81.

S. Li, W. Wang and P. Zhang (2015), Local well-posedness and small Deborah limit of a molecule-based Q-tensor system, *Discrete Contin. Dyn. Syst. Ser. B* **20**, 2611–2655.

T. Li, P. Zhang, X. Zhou *et al.* (2004), Analysis of 1 + 1 dimensional stochastic models of liquid crystal polymer flows, *Commun. Math. Sci.* **2**, 295–316.

Y. X. Li and J. X. Zhou (2001), A minimax method for finding multiple critical points and its applications to semilinear PDEs, *SIAM J. Sci. Statist. Comput.* **23**, 840–865.

F. Lin (1989), Nonlinear theory of defects in nematic liquid crystals: Phase transition and flow phenomena, *Commun. Pure Appl. Math.* **42**, 789–814.

F. Lin (1991), On nematic liquid crystals with variable degree of orientation, *Comm. Pure Appl. Math.* **44**, 453–468.

F. Lin and C. Liu (1995), Nonparabolic dissipative systems modeling the flow of liquid crystals, *Commun. Pure Appl. Math.* **48**, 501–537.

F. Lin and C. Liu (1996), Partial regularity of the dynamic system modeling the flow of liquid crystals, *Discrete Contin. Dyn. Syst. A* **2**, 1–22.

F. Lin and C. Liu (2001), Static and dynamic theories of liquid crystals, *J. Partial Differ. Equ.* **14**, 289–330.

F. Lin and C. C. Poon (1996), On nematic liquid crystal droplets, in *Elliptic and Parabolic Methods in Geometry (Minneapolis, MN, 1994)*, AK Peters, pp. 91–121.

F. Lin and C. Wang (2014), Recent developments of analysis for hydrodynamic flow of nematic liquid crystals, *Philos. Trans. Roy. Soc. London A* **372** (2029), 20130361.

F. Lin and C. Wang (2016), Global existence of weak solutions of the nematic liquid crystal flow in dimension three, *Commun. Pure Appl. Math.* **69**, 1532–1571.

F. Lin, J. Lin and C. Wang (2010), Liquid crystal flows in two dimensions, *Arch. Ration. Mech. Anal.* **197**, 297–336.

F. Lin, X. B. Pan and C. Wang (2012), Phase transition for potentials of high-dimensional wells, *Commun. Pure Appl. Math.* **65**, 833–888.

P. Lin and C. Liu (2006), Simulations of singularity dynamics in liquid crystal flows: A C^0 finite element approach, *J. Comput. Phys.* **215**, 348–362.

P. Lin, C. Liu and H. Zhang (2007), An energy law preserving C^0 finite element scheme for simulating the kinematic effects in liquid crystal dynamics, *J. Comput. Phys.* **227**, 1411–1427.

C. Liu and N. J. Walkington (2000), Approximation of liquid crystal flows, *SIAM J. Numer. Anal.* **37**, 725–741.

C. Liu and N. J. Walkington (2002), Mixed methods for the approximation of liquid crystal flows, *ESAIM Math. Model. Numer. Anal.* **36**, 205–222.

C. Liu and Y. Wang (2020*a*), On Lagrangian schemes for porous medium type generalized diffusion equations: A discrete energetic variational approach, *J. Comput. Phys.* **417**, 109566.

C. Liu and Y. Wang (2020*b*), A variational Lagrangian scheme for a phase field model: A discrete energetic variational approach. Available at arXiv:2003.10413.

C. Liu, J. Shen and X. Yang (2007), Dynamics of defect motion in nematic liquid crystal flow: Modeling and numerical simulation, *Commun. Comput. Phys* **2**, 1184–1198.

H. Liu, H. Zhang and P. Zhang (2005), Axial symmetry and classification of stationary solutions of Doi–Onsager equation on the sphere with Maier–Saupe potential, *Commun. Math. Sci.* **3**, 201–218.

Y. Liu and W. Wang (2018*a*), On the initial boundary value problem of a Navier–Stokes/Q-tensor model for liquid crystals, *Discrete Contin. Dyn. Syst. B* **23**, 3879.

Y. Liu and W. Wang (2018*b*), The Oseen–Frank limit of Onsager's molecular theory for liquid crystals, *Arch. Ration. Mech. Anal.* **227**, 1061–1090.

Y. Liu and W. Wang (2018*c*), The small Deborah number limit of the Doi–Onsager equation without hydrodynamics, *J. Funct. Anal.* **275**, 2740–2793.

L. Longa, D. Monselesan and H.-R. Trebin (1987), An extension of the Landau–Ginzburg–de Gennes theory for liquid crystals, *Liquid Cryst.* **2**, 769–796.

T. C. Lubensky, D. Pettey, N. Currier and H. Stark (1998), Topological defects and interactions in nematic emulsions, *Phys. Rev. E* **57**, 610.

C. S. MacDonald, J. A. Mackenzie and A. Ramage (2020), A moving mesh method for modelling defects in nematic liquid crystals, *J. Comput. Phys. X* **8**, 100065.

V. N. Mahajan and G. M. Dai (2007), Orthonormal polynomials in wavefront analysis: Analytical solution, *J. Optical Soc. Amer. A* **24**, 2994–3016.

W. Maier and A. Saupe (1958), Eine einfache molekulare Theorie des nematischen kristallinflüssigen Zustandes, *Z. Naturforschung A* **13**, 564–566.

A. Majumdar (2012), The radial-hedgehog solution in Landau–de Gennes' theory for nematic liquid crystals, *Europ. J. Appl. Math.* **23**, 61–97.

A. Majumdar and Y. Wang (2018), Remarks on uniaxial solutions in the Landau–de Gennes theory, *J. Math. Anal. Appl.* **464**, 328–353.

A. Majumdar and A. Zarnescu (2010), Landau–de Gennes theory of nematic liquid crystals: The Oseen–Frank limit and beyond, *Arch. Ration. Mech. Anal.* **196**, 227–280.

A. Majumdar, P. A. Milewski and A. Spicer (2016), Front propagation at the nematic–isotropic transition temperature, *SIAM J. Appl. Math.* **76**, 1296–1320.

A. Majumdar, C. J. P. Newton, J. M. Robbins and M. Zyskin (2007), Topology and bistability in liquid crystal devices, *Phys. Rev. E* **75**, 051703.

M. C. Marchetti, J.-F. Joanny, S. Ramaswamy, T. B. Liverpool, J. Prost, M. Rao and R. A. Simha (2013), Hydrodynamics of soft active matter, *Rev. Modern Phys.* **85**, 1143.

G. Marrucci and F. Greco (1991), The elastic constants of Maier–Saupe rodlike molecule nematics, *Molecular Cryst. Liquid Cryst.* **206**, 17–30.

D. Mehta (2011), Finding all the stationary points of a potential-energy landscape via numerical polynomial-homotopy-continuation method, *Phys. Rev. E* **84**, 025702.

A. Mertelj and D. Lisjak (2017), Ferromagnetic nematic liquid crystals, *Liquid Cryst. Rev.* **5**, 1–33.

A. Mertelj, D. Lisjak, M. Drofenik and M. Čopič (2013), Ferromagnetism in suspensions of magnetic platelets in liquid crystal, *Nature* **504**, 237–241.

J. W. Milnor, M. Spivak and R. Wells (1969), *Morse Theory*, Vol. 1, Princeton University Press.

R. A. Miron and K. A. Fichthorn (2001), The step and slide method for finding saddle points on multidimensional potential surfaces, *J. Chem. Phys.* **115**, 8742–8747.

S. Mkaddem and E. C. Gartland Jr (2000), Fine structure of defects in radial nematic droplets, *Phys. Rev. E* **62**, 6694.

N. J. Mottram and S. J. Hogan (1997), Disclination core structure and induced phase change in nematic liquid crystals, *Philos. Trans. Roy. Soc. London A* **355**, 2045–2064.

N. J. Mottram and T. J. Sluckin (2000), Defect-induced melting in nematic liquid crystals, *Liquid Cryst.* **27**, 1301–1304.

N. Mousseau and G. T. Barkema (1998), Traveling through potential energy landscapes of disordered materials: The activation–relaxation technique, *Phys. Rev. E* **57**, 2419.

M. Muller, Y. G. Smirnova, G. Marelli, M. Fuhrmans and A.-C. Shi (2012), Transition path from two apposed membranes to a stalk obtained by a combination of particle simulations and string method, *Phys. Rev. Lett.* **108**, 228103.

I. Muševič, M. Škarabot, U. Tkalec, M. Ravnik and S. Žumer (2006), Two-dimensional nematic colloidal crystals self-assembled by topological defects, *Science* **313** (5789), 954–958.

M. Nestler, I. Nitschke, S. Praetorius and A. Voigt (2018), Orientational order on surfaces: The coupling of topology, geometry, and dynamics, *J. Nonlinear Sci.* **28**, 147–191.

L. Nguyen and A. Zarnescu (2013), Refined approximation for minimizers of a Landau–de Gennes energy functional, *Calc. Var. Partial Differential Equations* **47**, 383–432.

I. Nitschke, M. Nestler, S. Praetorius, H. Löwen and A. Voigt (2018), Nematic liquid crystals on curved surfaces: A thin film limit, *Proc. Roy. Soc. A* **474**, 20170686.

R. H. Nochetto, S. W. Walker and W. Zhang (2017), A finite element method for nematic liquid crystals with variable degree of orientation, *SIAM J. Numer. Anal.* **55**, 1357–1386.

J. Noh, Y. Wang, H.-L. Liang, V. Subba, R. Jampani, A. Majumdar and J. P. F. Lagerwall (2020), Dynamic tuning of the director field in liquid crystal shells using block copolymers, *Phys. Rev. E* **2**, 033160.

M. Oh-e and K. Kondo (1995), Electro-optical characteristics and switching behavior of the in-plane switching mode, *Appl. Phys. Lett.* **67**, 3895–3897.

L. Onsager (1949), The effects of shape on the interaction of colloidal particles, *Ann. New York Acad. Sci.* **51**, 627–659.

C. W. Oseen (1933), The theory of liquid crystals, *Trans. Faraday Soc.* **29**, 883–899.

M. Paicu and A. Zarnescu (2012), Energy dissipation and regularity for a coupled Navier–Stokes and Q-tensor system, *Arch. Ration. Mech. Anal.* **203**, 45–67.

J. Park, W. Wang, P. Zhang and Z. Zhang (2017), On minimizers for the isotropic–nematic interface problem, *Calc. Var. Partial Differential Equations* **56**, 41.

O. Parodi (1970), Stress tensor for a nematic liquid crystal, *J. de Physique* **31**, 581–584.

J. Prost, F. Jülicher and J.-F. Joanny (2015), Active gel physics, *Nature Phys.* **11**, 111–117.

T. Qian and P. Sheng (1998), Generalized hydrodynamic equations for nematic liquid crystals, *Phys. Rev. E* **58**, 7475.

Y. Qu, Y. Wei and P. Zhang (2017), Transition of defect patterns from 2D to 3D in liquid crystals, *Commun. Comput. Phys.* **21**, 890–904.

A. Ramage and A. M. Sonnet (2016), Computational fluid dynamics for nematic liquid crystals, *BIT Numer. Math.* **56**, 573–586.

M. Ravnik and S. Žumer (2009), Landau–de Gennes modelling of nematic liquid crystal colloids, *Liquid Cryst.* **36**, 1201–1214.

W. Ren and E. Vanden-Eijnden (2013), A climbing string method for saddle point search, *J. Chem. Phys.* **138**, 134105.

A. D. Rey and T. Tsuji (1998), Recent advances in theoretical liquid crystal rheology, *Macromolecular Theory Simul.* **7**, 623–639.

M. Robinson, C. Luo, P. E. Farrell, R. Erban and A. Majumdar (2017), From molecular to continuum modelling of bistable liquid crystal devices, *Liquid Cryst.* **44**, 2267–2284.

A. Samanta and W. E (2013), Optimization-based string method for finding minimum energy path, *Commun. Comput. Phys.* **14**, 265–275.

J. Shen and X. Yang (2010), Numerical approximations of Allen–Cahn and Cahn–Hilliard equations, *Discrete Contin. Dyn. Syst. A* **28**, 1669.

J. Shen, J. Xu and J. Yang (2018), The scalar auxiliary variable (SAV) approach for gradient flows, *J. Comput. Phys.* **353**, 407–416.

J. Shen, J. Xu and J. Yang (2019), A new class of efficient and robust energy stable schemes for gradient flows, *SIAM Rev.* **61**, 474–506.

Q. Shen, C. Liu and M. C. Calderer (2002), Axisymmetric configurations of bipolar liquid crystal droplets, *Contin. Mech. Thermodyn.* **14**, 363–375.

M. Siavashpouri, C. H. Wachauf, M. J. Zakhary, F. Praetorius, H. Dietz and Z. Dogic (2017), Molecular engineering of chiral colloidal liquid crystals using DNA origami, *Nature Materials* **16**, 849–856.

A. Sonnet, A. Kilian and S. Hess (1995), Alignment tensor versus director: Description of defects in nematic liquid crystals, *Phys. Rev. E* **52**, 718.

K. Stephen and G. Adrian (2002), Controllable alignment of nematic liquid crystals around microscopic posts: Stabilization of multiple states, *Appl. Phys. Lett.* **80**, 3635–3637.

I. W. Stewart (2004), *The Static and Dynamic Continuum Theory of Liquid Crystals: A Mathematical Introduction*, Taylor & Francis.

T. Takashi and N. Yasumasa (2010), Morphological characterization of the diblock copolymer problem with topological computation, *Japan. J. Indust. Appl. Math.* **27**, 175–190.

J. M. Taylor (2018), Oseen–Frank-type theories of ordered media as the Γ-limit of a non-local mean-field free energy, *Math. Models Methods Appl. Sci.* **28**, 615–657.

Y. Tong, Y. Wang and P. Zhang (2017), Defects around a spherical particle in cholesteric liquid crystals, *Numer. Math. Theory Methods Appl.* **10**, 205–221.

E. Vanden-Eijnden *et al.* (2010), Transition-path theory and path-finding algorithms for the study of rare events, *Ann. Rev. Phys. Chem.* **61**, 391–420.

T. L. Vincent, B. S. Goh and K. L. Teo (1992), Trajectory-following algorithms for min-max optimization problems, *J. Optim. Theory Appl.* **75**, 501–519.

M. A. C. Vollmer (2017), Critical points and bifurcations of the three-dimensional Onsager model for liquid crystals, *Arch. Ration. Mech. Anal.* **226**, 851–922.

J. Vukadinovic (2009), Inertial manifolds for a Smoluchowski equation on the unit sphere, *Commun. Math. Phys.* **285**, 975–990.

S. W. Walker (2020), A finite element method for the generalized Ericksen model of nematic liquid crystals, *ESAIM Math. Model. Numer. Anal.* **54**, 1181–1220.

N. J. Walkington (2011), Numerical approximation of nematic liquid crystal flows governed by the Ericksen–Leslie equations, *ESAIM Math. Model. Numer. Anal.* **45**, 523–540.

M. Walters, Q. Wei and J. Z. Y. Chen (2019), Machine learning topological defects of confined liquid crystals in two dimensions, *Phys. Rev. E* **99**, 062701.

Q. Wang (2002), A hydrodynamic theory for solutions of nonhomogeneous nematic liquid crystalline polymers of different configurations, *J. Chem. Phys.* **116**, 9120–9136.

Q. Wang, W. E, C. Liu and P. Zhang (2002), Kinetic theory for flows of nonhomogeneous rodlike liquid crystalline polymers with a nonlocal intermolecular potential, *Phys. Rev. E* **65**, 051504.

W. Wang, P. Zhang and Z. Zhang (2013), Well-posedness of the Ericksen–Leslie system, *Arch. Ration. Mech. Anal.* **210**, 837–855.

W. Wang, P. Zhang and Z. Zhang (2015*a*), Rigorous derivation from Landau–de Gennes theory to Ericksen–Leslie theory, *SIAM J. Math. Anal.* **47**, 127–158.

W. Wang, P. Zhang and Z. Zhang (2015*b*), The small Deborah number limit of the Doi–Onsager equation to the Ericksen–Leslie equation, *Commun. Pure Appl. Math.* **68**, 1326–1398.

Y. Wang, G. Canevari and A. Majumdar (2019), Order reconstruction for nematics on squares with isotropic inclusions: A Landau–de Gennes study, *SIAM J. Appl. Math.* **79**, 1314–1340.

Y. Wang, P. Zhang and J. Z. Y. Chen (2017), Topological defects in an unconfined nematic fluid induced by single and double spherical colloidal particles, *Phys. Rev. E* **96**, 042702.

Y. Wang, P. Zhang and J. Z. Y. Chen (2018), Formation of three-dimensional colloidal crystals in a nematic liquid crystal, *Soft Matter* **14**, 6756–6766.

M. Wilkinson (2015), Strictly physical global weak solutions of a Navier–Stokes Q-tensor system with singular potential, *Arch. Ration. Mech. Anal.* **218**, 487–526.

E. Willman, F. A. Fernández, R. James and S. E. Day (2008), Switching dynamics of a post-aligned bistable nematic liquid crystal device, *J. Display Technol.* **4**, 276–281.

J. Xu and P. Zhang (2014), From microscopic theory to macroscopic theory: Symmetries and order parameters of rigid molecules, *Sci. China Math.* **57**, 443–468.

J. Xu and P. Zhang (2018), Calculating elastic constants of bent-core molecules from Onsager-theory-based tensor model, *Liquid Cryst.* **45**, 22–31.

J. Xu, Y. Li, S. Wu and A. Bousquet (2019), On the stability and accuracy of partially and fully implicit schemes for phase field modeling, *Comput. Methods Appl. Mech. Engrg* **345**, 826–853.

J. Xu, F. Ye and P. Zhang (2018), A tensor model for nematic phases of bent-core molecules based on molecular theory, *Multiscale Model. Simul.* **16**, 1581–1602.

X. Yang (2016), Linear, first and second-order, unconditionally energy stable numerical schemes for the phase field model of homopolymer blends, *J. Comput. Phys.* **327**, 294–316.

J. Yin, Y. Wang, J. Z. Y. Chen, P. Zhang and L. Zhang (2020*a*), Construction of a pathway map on a complicated energy landscape, *Phys. Rev. Lett.* **124**, 090601.

J. Yin, B. Yu and L. Zhang (2020*b*), Searching the solution landscape by generalized high-index saddle dynamics, *Sci. China Math.* doi:10.1007/s11425-020-1737-1.

J. Yin, L. Zhang and P. Zhang (2019), High-index optimization-based shrinking dimer method for finding high-index saddle points, *SIAM J. Sci. Comput.* **41**, A3576–3595.

H. Yu and P. Zhang (2007), A kinetic–hydrodynamic simulation of microstructure of liquid crystal polymers in plane shear flow, *J. Non-Newtonian Fluid Mech.* **141**, 116–127.

H. Yu, G. Ji and P. Zhang (2010), A nonhomogeneous kinetic model of liquid crystal polymers and its thermodynamic closure approximation, *Commun. Comput. Phys.* **7**, 383–402.

Y. Yu (2020), Disclinations in limiting Landau–de Gennes theory, *Arch. Ration. Mech. Anal.* **237**, 147–200.

P. Yue, J. J. Feng, C. Liu and J. Shen (2004), A diffuse-interface method for simulating two-phase flows of complex fluids, *J. Fluid Mech.* **515**, 293.

F. Zernike (1934), Diffraction theory of the knife-edge test and its improved form, the phase-contrast method, *Month. Not. Roy. Astronom. Soc.* **94**, 377–384.

H. Zhang and P. Zhang (2007), Stable dynamic states at the nematic liquid crystals in weak shear flow, *Phys. D* **232**, 156–165.

H. Zhang and P. Zhang (2008), On the new multiscale rodlike model of polymeric fluids, *SIAM J. Math. Anal.* **40**, 1246–1271.

J. Zhang and Q. Du (2012), Shrinking dimer dynamics and its applications to saddle point search, *SIAM J. Numer. Anal.* **50**, 1899–1921.

L. Zhang, Q. Du and Z. Z. Zheng (2016*a*), Optimization-based shrinking dimer method for finding transition states, *SIAM J. Sci. Comput.* **38**, A528–A544.

L. Zhang, W. Q. Ren, A. Samanta and Q. Du (2016*b*), Recent developments in computational modelling of nucleation in phase transformations, *NPJ Comput. Materials* **2**, 16003.

J. Zhao and Q. Wang (2016), Semi-discrete energy-stable schemes for a tensor-based hydrodynamic model of nematic liquid crystal flows, *J. Sci. Comput.* **68**, 1241–1266.

J. Zhao, X. Yang, Y. Gong and Q. Wang (2017), A novel linear second order unconditionally energy stable scheme for a hydrodynamic Q-tensor model of liquid crystals, *Comput. Methods Appl. Mech. Engrg* **318**, 803–825.

J. Zhao, X. Yang, J. Li and Q. Wang (2016), Energy stable numerical schemes for a hydrodynamic model of nematic liquid crystals, *SIAM J. Sci. Comput.* **38**, A3264–A3290.

C. Zhou, P. Yue and J. J. Feng (2007), The rise of Newtonian drops in a nematic liquid crystal, *J. Fluid Mech.* **593**, 385–404.

H. Zhou, H. Wang, M. G. Forest and Q. Wang (2005), A new proof on axisymmetric equilibria of a three-dimensional Smoluchowski equation, *Nonlinearity* **18**, 2815–2825.

S. Zhou, A. Sokolov, O. D. Lavrentovich and I. S. Aranson (2014), Living liquid crystals, *Proc. Nat. Acad. Sci.* **111**, 1265–1270.

T. Zhu, J. Li, A. Samanta, H. G. Kim and S. Suresh (2007), Interfacial plasticity governs strain rate sensitivity and ductility in nanostructured metals, *Proc. Nat. Acad. Sci.* **104**, 3031–3036.